Search for a Singly Strange Hexaquark Using Polarization Data From CLAS12 at Jefferson Lab Virginia

Geraint Clash

Doctor of Philosophy

University of York
Physics, Engineering and Technology

September 2023

Abstract

Recently hadron spectroscopy has seen a lot of success. There has been a large number of baryon and meson resonances discovered over the last two decades. There have also been several tetra and pentaquark candidates with experimental evidence but not confirmed. The first serious candidate was the X(3872), a potential tetraquark, leading to this rise in success for exotic hadron physics. This has brought about improvements in Quantum Chromo Dynamics (QCD), our current best description of interactions between quarks and gluons. QCD predicts the existence of hexaquark states, and then the $d^*(2380)$ was discovered. This thesis explores the rest of the d^* $J^p = 3^+$ anti-decuplet by searching for experimental evidence of the d_s hexaquark. This is the first analysis of the $e'd \rightarrow e'K^+d_s^0 \rightarrow e'K^+\Lambda n$ channel using the $P_{y'}$ measurements of the Λ as a lens to perform this search. This observable was extracted from Λ electroproduction events off a liquid deuterium target. From this an upper limit of the Breit-Wigner peak strength was extracted. This was done with the use of the CLAS12 detector system housed at Thomas Jefferson Laboratory in Virginia, USA. These polarization measurements are the first to be made on this data, and this is the first time the d_s has been searched for in such a way.

Table of contents

Abstract **3**

Table of contents **5**

List of figures **9**

List of tables **11**

Dedication **13**

Acknowledgements **15**

Declaration **17**

1 Introduction **19**

1.1 Hadron Physics a Brief History 19

1.2 Hadron Physics an Overview 20

1.2.1 Fundamental Particles 21

1.2.2 Fundamental Forces 22

1.2.3 Strong Force and Hadrons 23

1.3 Hadron Spectroscopy 28

1.3.1 Electroproduction 28

1.3.2 Polarization 29

1.4 Exotic Hadron Spectroscopy 32

1.5 Hexaquarks 33

1.6 Summary 36

2 Experiment **37**

2.1 Jefferson Laboratory and CEBAF 38

2.2 CLAS12 Experiment Setup 39

2.2.1 Forward Tagger 40

2.2.2 Forward Detector 44

2.2.3 Central Detector . . . 50
2.2.4 Superconducting Magnets . . . 54
2.2.5 Data Acquisition . . . 55

3 Search for the Singly Strange Hexaquark **57**
3.1 Properties of the d_s . . . 57
3.2 Evidence for the $d^*(2380)$ . . . 62
3.3 Bump Hunt . . . 63
3.4 Polarization . . . 65
3.4.1 Asymmetry in the Λ Weak Decay . . . 65
3.4.2 Extraction of the Λ Polarisation . . . 66
3.5 Acceptance Corrections . . . 68
3.5.1 Simulations . . . 69
3.6 The Final Search Method . . . 69
3.6.1 Kinematic Based Sensitivity of Polarization . . . 70
3.7 Summary . . . 72

4 Data Handling and Reconstruction **73**
4.1 Run Groups . . . 73
4.2 Data Reconstruction . . . 75
4.2.1 Calibration and Cooking . . . 75
4.3 Event Selection . . . 75
4.3.1 Particle Identification . . . 76
4.4 Summary . . . 78

5 Data Analysis **79**
5.1 Missing and Invariant Mass . . . 79
5.2 Bump Hunt . . . 80
5.3 Channel Selection for Polarization Analysis . . . 80
5.3.1 Missing and Invariant Masses . . . 81
5.3.2 RGB Specific Variables . . . 85
5.4 Summary . . . 89

6 Results and Discussion **91**
6.1 The Components of Polarization with a Vanishing Response Function . . . 92
6.2 The Component of Polarization with a Non-vanishing Response Function . . . 95

7 Conclusion and Future Work **101**
7.1 Conclusion . . . 101
7.2 Future Work . . . 102

7.2.1 Other Experiments 102

List of figures

1.1 Summary of the standard model. 21
1.2 Basic structure of some of the known hadrons. 23
1.3 Increasing complexity of proton structure. 24
1.4 Summary of the standard model. 26
1.5 Feynman diagram conventions. 28
1.6 The kinematics of electroproduction. 29
1.7 $J^p = 3^+$ multiplet 33
1.8 Genuine hexaquark structure of the d_s^0. 34
1.9 Quark level structure of a molecular d_s^0. 35
1.10 $J^p = 3^+$ multiplet 35

2.1 CEBAF aerial photo 38
2.2 CEBAF diagram. 39
2.3 CLAS12 overview. 40
2.4 Diagram of the FT. 41
2.5 Cross section of the FT. 42
2.6 Illustration of micromega tracker operational principle. 43
2.7 FT-Hodo 2D tile arrangement. 44
2.8 DC schematic labelled. 45
2.9 DC wire layout diagram. 45
2.10 HTCC diagram cut to show PMTS and mirrors. 46
2.11 Single sector of the LTCC with the optics labelled. 47
2.12 Cherenkov radiation angle vs the particle momentum. 48
2.13 RICH schematic. 48
2.14 FTOF diagram. 49
2.15 Illustration of ECAL Layers. 50
2.16 SVT schematic. 51
2.17 BMT diagram. 51
2.18 CTOF scintillator bars 52
2.19 CND drawing 52

2.20 Magnetic field strength heat map. 54
2.21 Summary of the trigger system. 56

3.1 d^* anti-decuplet and Δ decuplet. 57
3.2 Total cross-section vs $\sqrt{s}$ for the $pn \to d\pi^0\pi^0$ reaction. 62
3.3 Feynman diagram of the $d_s \to \Delta^{++}\Sigma^{*-}$ channel. 63
3.4 Acceptance vs M($\Delta^{++}\Sigma^{*-}$). 64
3.5 Two common decay branches of d^* and the d_s. 65
3.6 Electroduction diagram with polarization axes defined. 66
3.7 Plot of the $\cos\theta^{\Lambda}_{p_{y'}}$. 68
3.8 Analysing power of neutron from d^* decay. 70
3.9 Plot of the P^1_3 associated Legendre polynomial 71
3.10 Definitions of $\theta^{d^*}_n$ and $\theta^{d_s}_{\Lambda}$. 71

4.1 CLAS12 trigger control. 74
4.2 β_{TOF} VS P with a $|\chi^2_{PID}|$ cut of < 5 from the RGA data. 77

5.1 Feynman diagram of the $ed \to e'K^+d^0_s \to e'K^+\Lambda n \to e'K^+p\pi^-n$ reaction. 80
5.2 RGA exclusive missing mass. 82
5.3 Missing neutron mass. 83
5.4 Invariant mass of the Λ for both RGA and RGB. 84
5.5 Invariant mass of the Λ for both RGA and RGB on the same plot. 84
5.6 Missing neutron momentum. 86
5.7 Missing neutron momentum. 87
5.8 $\theta^{d_s}_{\Lambda}$ result. 88
5.9 Associated Legendre polynomial secondary peak marked. 89

6.1 $P_{x'}$ vs MM(e'K^+) RGA and RGB side by side comparison. 93
6.2 $P_{z'}$ vs MM(e'K^+) RGA and RGB side by side comparison. 94
6.3 $P_{y'}$ vs MM(e'K^+) RGA and RGB side by side comparison. 95
6.4 $P_{y'}$ vs $MM(e'K^+)$ with the fit described by Equation 6.7. 97
6.5 $P_{y'}$ vs $MM(e'K^+)$ with the fit described by Equation 6.7. 98
6.6 $P_{y'}$ vs $MM(e'K^+)$ with the fit described by Equation 6.7. 99
6.7 Upper 100

List of tables

1.1 Summary of the fundamental forces. 23
1.2 Summary of the response functions for pseudoscalar electroproduction. 31

2.1 Summary of the major detector systems of CLAS12. 53

3.1 Partial widths and branching ratios for the decay channels of the d_s. 61

6.1 Summary of the fit results of P_y. 96

Dedication

I want to dedicate this thesis to my late Grandmother, Marcia Johns, and my late Grandfather, Vernon Clash. They both would have loved to see this for themselves as they were both incredibly supportive in the sections of my education they were able to be a part of.

Acknowledgements

There are many people I would like to thank for assistance on this thesis, but I cannot thank everyone, so I do apologise for any accidental omission. First, I would like to thank my supervisors, Dr Mikhail Bashkanov and Dr Nick Zachariou, for taking me on as a student in the first place, supporting me through this research with fantastic insight into problems, especially useful when I have been ever so slightly shambolic. Next has to be my honorary third supervisor, Dr. Stuart Fegan. In times of great worry, he kept me level-headed and on the road to the completion of this thesis. If it were not for him letting me know I was still on track after doubting myself, this thesis likely would not exist. Prof. Dan Watts must be mentioned for not only being a brilliant head of our little hadron group but also for correctly introducing me to academia with a very welcoming pub visit. There are other members of staff, but we are risking a record-breaking acknowledgements section. The final people I will thank by name are Dr. Matthew Nicol and Mihai Mocanu. They both started their PhDs at the same time as I did and have been not only fantastic colleagues to bounce ideas off but also two wonderful friends who supported me both inside and outside of the office.

On the subject of thanking those who helped outside of an academic scope, I would like to thank my beautiful girlfriend, Lori McGuigan. I met her during the PhD, and she has been emotional support from day one, lifting me out of ruts so I could continue. My parents must be thanked next as during the pandemic, I moved back in with them as my flat in York at the time was not suitable to work from. More than that, they have always advocated for me in the pursuit of this dream career path. Again, apologies that I can not mention everyone, but a big thank you to everyone who has listened to me both gush over and complain about my research.

Finally, a thank you to the Unversity of York and the STFC for funding me to pursue this degree, as I do not believe I would have been able to do it self-funded.

Declaration

I declare that this thesis is a presentation of original work, and I am the sole author. I am a co-author of a theoretical paper written where the results were used in this work. I am the author of the CERN ROOT macro used to build the TTree discussed in Chapter 4 and the ROOT macro used to analyse the TTree's, which is discussed in Chapter 5. I am the sole person to carry out the analysis which produced the plots and results shown and discussed in Chapter 5 and 6. This work has not previously been presented for an award at this, or any other, University. All sources are acknowledged as References.

Chapter 1

Introduction

This thesis presents work towards the first experimental evidence of a strange hexaquark, the d_s, a particle with quark content *uuudds* or *uuddds*. The research attempts to provide information used to answer the question of whether this particle and other $J^p = 3^+$ hexaquarks are genuine hexaquarks or a molecule of two baryons. The search is through the lens of polarization, and therefore this work also provides measurements of the Λ polarization ($P_{x'}$, $P_{y'}$ and $P_{z'}$) in the reaction $ed \to e'K^+X \to e'K^+\Lambda n$ where the Λ decays to $p\pi^-$.

This chapter will begin with a brief history of the development of hadron physics. Then the underlying theory needed to understand the research will also be presented here. Starting with an overview of hadron physics, then going deeper into the strong force. A summary of hadron physics is given, including some details on electroproduction and polarization. Finally, a brief history of exotic hadron spectroscopy is provided, along with the motivation for this hexaquark search.

1.1 Hadron Physics a Brief History

In the infancy of the parent field that would evolve to become hadron physics, the original model of the atom was borrowed from an ancient Greek picture of the world; this model stated the atom was the most fundamental building block of matter. Then, at the end of the 1800s, ideas evolved, and J.J. Thomson, after his discovery of the electron, surmised how they might fit into the structure of the atom [1]. This came to be known as the plum pudding model and splits the atom into a positively charged sphere with negatively charged electrons (the plums of the pudding) situated within it. Later came Rutherford, who performed the famous alpha scattering experiment with gold atoms, improving our picture of the atom by learning that the positive charge was at the centre of the atom. This came to be known as the nucleus and contained the majority of the mass of the atom [2]. Improving upon this again came Bohr [3], and the Bohr model is still valid for modern physics. The model breaks down the atom into a nucleus and electrons that orbit at specific energy levels, making the Bohr model integral to the birth of quantum mechanics. Later, the nucleus' composite nucleons (protons and neutrons)

were discovered first with the proton by Rutherford in 1919 [4], and then the neutron, having evidence for it found in 1932 by James Chadwick [5].
After this, hadron physics started to see a lot of success, starting with the discovery of the pions (predicted to be the particle responsible for nucleon-nucleon interactions [6]) and kaons with observations of cosmic rays [7]. Other baryons, like the Λ [8] and the Ω [9], were also discovered. From this came further complications of the picture with the discovery of the quarks that compose those baryons. The quarks were initially proposed by Murray Gell-Mann [10] and George Zweig [11] independently at the same time (although Gell-Mann coined the term quark and Zweig referred to them as aces). Both proposed three quarks: up, down and strange (u,d and s). Now we are aware of six quarks adding the charm [12] (the positive counterpart to the strange), bottom [13] and top [14] quarks. After a summary of the history of the field that this thesis makes a contribution to, it is appropriate to move on to physics, starting with particle physics to cover the interactions important for this research.

1.2 Hadron Physics an Overview

An overview of particle physics is required to understand hadron physics to the level needed to interpret successfully, the motivation behind this thesis, the methodology used, and the conclusions made by the work presented. It is appropriate to start with a summary of the standard model, as this is the current best theory for understanding how fundamental particles behave and interact throughout the universe.

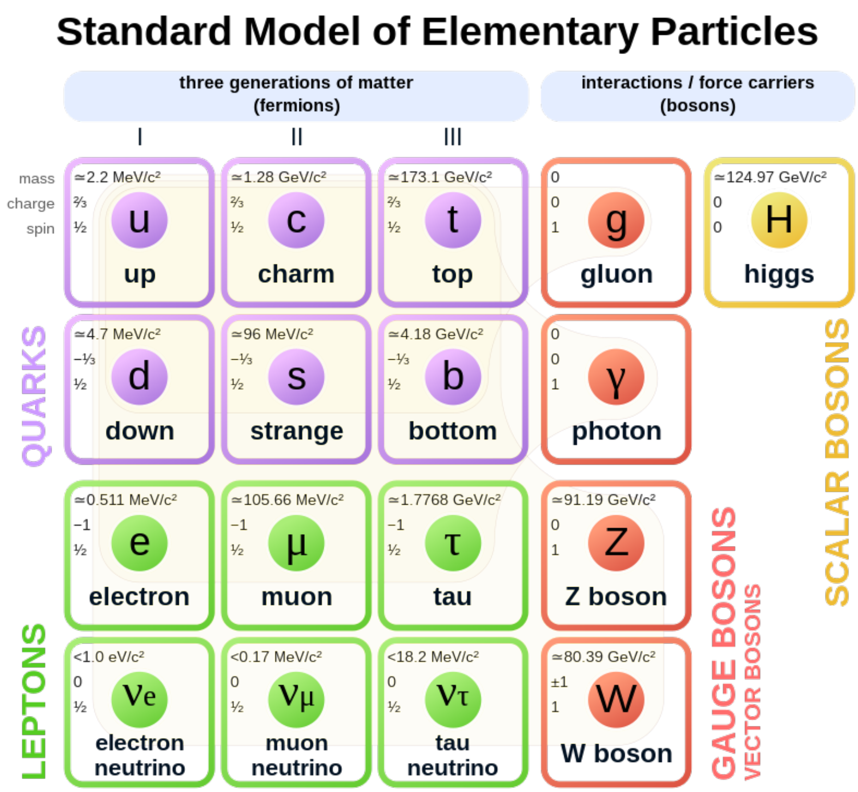

Fig. 1.1 Diagram of all the known fundamental particles of the standard model. Showing the mass, charge and spin of each particle and how they fit into various categories.

1.2.1 Fundamental Particles

All the particles of the standard model are outlined well in Figure 1.1, clearly showing the various categories they fit into. The first categories to be addressed are the broadest fermions and the bosons. These two groups are distinguished by their spin: fermions have half-integer spin, and bosons have integer spin. All matter consists of combinations and mixtures of these fundamental fermions, but this matter can have an integer spin as a whole and be a boson. This is important due to another difference between fermions and bosons, which is their ability to occupy the same quantum state, fermions can not, but bosons can.

Expanding the fermion category, there are two smaller groups, leptons and quarks, both of which are comprised of three generations and six particles. Focusing on the leptons first, there are the electron (e), muon (μ) and tauon (τ). Each of these has the charge of the electron, which is $e = -1.602 \times 10^{-19}$ C, and from here on, all electric charges will be referred to relative to this unit charge (the electron has a charge of -1). All of the charged leptons have a neutral corresponding neutrino, making up the six total leptons. With quarks, there are only quarks and no neutrino equivalent. Just like the leptons, the

generations are rising in mass. The quarks can be separated into the three generations, six flavours or the three positively charged $\left(+\frac{2}{3}\right)$ and the three negatively charged $\left(-\frac{1}{3}\right)$ ones.
Moving on to the bosons that also come in two categories the vector or gauge bosons and the scalar bosons. The only scalar boson is the Higgs boson, the particle complimentary to the Higgs field responsible for the rest mass of the leptons, the W and Z bosons and the resting undressed quark mass. More important to this work are the four gauge bosons, also known as force carriers.

1.2.2 Fundamental Forces

Strictly speaking, there are four fundamental forces in the universe gravity, the weak force, electromagnetism and the strong force. Gravity is separate from the others as, at the time of writing this thesis, it does not have a proper quantum description backed up by experimental evidence. There is a hypothesised mediating particle known as a graviton which, according to models, would have a spin of 2. It is known that gravity has an infinite range, and its influence radiates at the speed of light, meaning the graviton would be massless.
The weakest of the forces other than gravity is the weak nuclear force, mediated by the $W^{+/-}$ bosons and the Z^0 boson. This force is responsible for various nuclear decays and some decays of baryons and only interacts with quarks and leptons, and due to the W bosons having electromagnetic charge, they can couple to photons also. Weak interactions have to hold to most conservation laws like charge, energy, momentum, total angular momentum, lepton number and baryon number but can break parity conservation and quark flavour; this is unique to the weak interaction. The force is limited to short distances, specifically a range of about 10^{-18} m [15]. This can be explained by the large masses of these particles (greater than 80 GeV) and considering the Heisenberg uncertainty principle $\Delta E \Delta t \geq \frac{\hbar}{2}$. Where ΔE is uncertainty in energy, Δt is the uncertainty in time and $\hbar$ is the reduced Planks constant. To describe this, the large amount of energy needed for the W and Z bosons means they can only exist for a very short time.
The next force in order of increasing strength is electromagnetism. This is the force responsible for chemical bonds, various scattering reactions and shifts in electron energy levels; basically, it can interact with all charged particles. Mediated by the massless photon, which can travel freely, giving the electromagnetic force an infinite range [15].
The final and strongest force is the strong nuclear force. This is responsible for holding nuclei together and bonding the quarks in the individual nucleons. It is mediated by the gluon, which is a massless particle, but unlike the photon, it can self-interact, and that property keeps it to a limited range of $\sim 10^{-15}$ m [15].

Table 1.1 A summary of the four fundamental forces in the standard model. Showing the strength relative to the strong force, the gauge bosons responsible for the propagation of the force and the Range of the force in meters [15].

Force	**Relative Strength**	**Gauge Boson(s)**	**Range (m)**
Gravity	5×10^{-40}	Graviton (G)	∞
Weak	1.17×10^{-5}	W^+, W^- and Z^0 bosons	$\sim 10^{-18}$
Electromagnetism	$\frac{1}{137}$	Photon (γ)	∞
Strong	1	Gluon (g)	$\sim 10^{-15}$

1.2.3 Strong Force and Hadrons

As described above, the strong force only mediates interactions between quarks and gluons or gluon self-interactions. Particles consisting of quarks and/or gluons all come under the title of hadrons. There are different groups of hadrons separated mainly by their structure. Two well-known major categories of hadrons are the baryons (three valence quarks) and mesons (a quark and anti-quark pair).

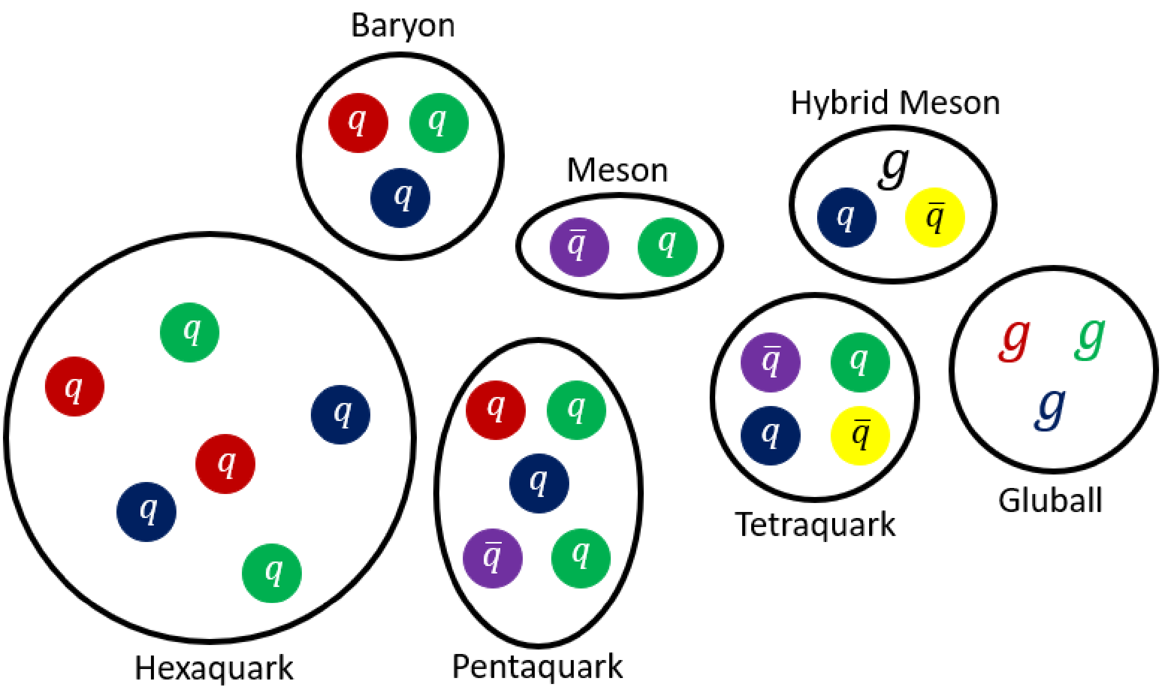

Fig. 1.2 Illustration of the single quark bag structures for a subset of the known hadrons. Quarks are coloured solid circles labelled q, anti-quarks are coloured dots labelled q, and gluons are the g's.

Figure 1.2 summarises a subset of the possible hadrons allowed to form according to our current understanding. In addition to the previously mentioned mesons and baryons, there are tetra, penta and hexaquarks. The tetraquark can be understood as a single particle containing two quark anti-quark pairs or a molecule of two mesons, and the pentaquark similarly can be understood as either a particle with four quarks and an antiquark or a molecule of a baryon and a meson. The hexaquark may be a single six-quark particle, a particle containing three quarks and three antiquarks, a molecule of two baryons or a baryon and anti-baryon molecule. What is meant by a particle versus a molecule essentially comes down to the size or width of the object and, therefore, the distance over which the forces are acting. As shown in Table 1.1, the strong force has a max range. When discussing quark-gluon interactions, this range is < 1 fm [16]; when this is exceeded, the mediating particle is a meson (typically a pion as it is the lightest meson), and this means that not all quarks are confined in a single particle state, and we describe it a molecule. The specifics of how this structure can be determined for a hexaquark will be discussed later.. The other two types are different; the hybrid mesons are similar to the regular mesons but with an additional gluon degree of freedom. The glueball is a truly unique hadron, consisting of only gluons (a minimum of two to make a colour-neutral object) and no valence quarks.

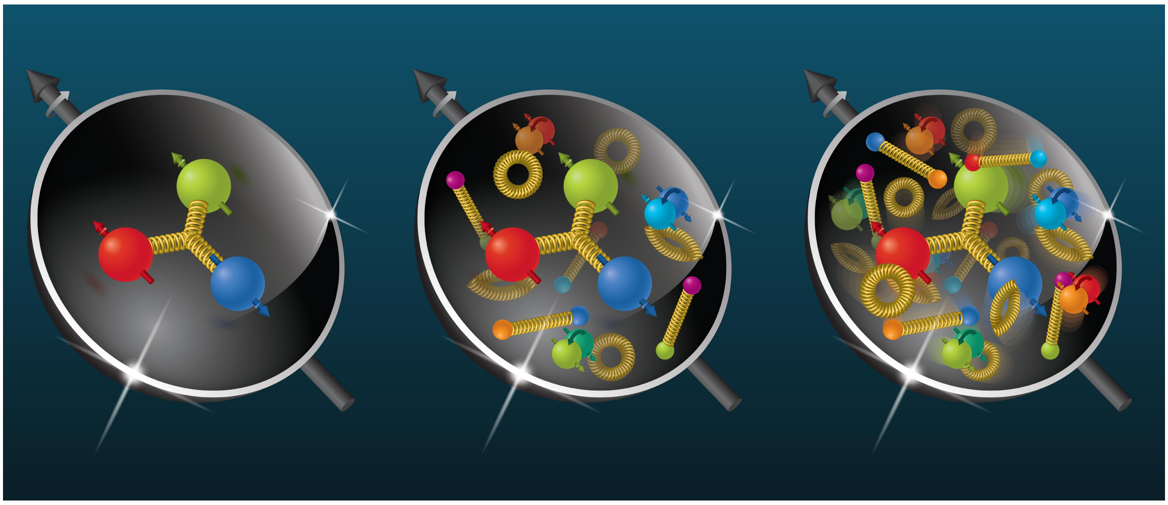

Fig. 1.3 A simplified depiction of the increasing complexity (from left to right) of the proton's structure as discussed below [17].

This is a surface-level picture of the structure of hadrons only concerning valence or constituent quarks. Looking more deeply into the internal structure of hadrons, it is known that there is a sea of quarks and anti-quarks amongst the valence quarks. To explain this, it is worth working backwards a bit and looking at how it is possible to discuss hadrons as a particle with no mention of the internal structure. This is sometimes done in nuclear physics, discussing areas of research such as exotic nuclei. Then there are the constituent quarks; looking at Figure 1.1, the mass of quarks can be seen, and one can see the combined masses of two up quarks, and one down quark (the valence quarks of the proton) is only about 1% of the mass of the proton. Part of this puzzle, known as Emergent Hadronic Mass (EHM), comes from the mass-energy equivalence with that energy coming from the quark-gluon interactions. Along with the mass of hadrons, with the same valence quarks, being different due to the total spin of the valence quarks and angular momentum between them. This effect is known as hyperfine splitting, and an example of this is the proton and the Δ^+ baryon. Both have uud valence quarks, but the proton has a mass of 938 MeV, and the Δ^+ has a mass of 1232 MeV; the difference is the proton is a $J^p = \frac{1}{2}^+$ particle, and the Δ^+ is a $J^p = \frac{3}{2}^+$ particle (explanation of J^p in the QCD subsection below). However, accounting for all these properties of the valence quarks does not equate to the measured mass of the proton or any hadron. There is hope that building a 3D picture of the full structure of hadrons like the proton, including the sea of quarks, will help fully understand the mystery of EHM. This progression in complexity of the structure of hadrons is illustrated in Figure 1.3. But for this research, it is appropriate to remain at the valence quark level of hadron structure.

QCD

The understanding of what hadrons can form comes from the theory underpinning how hadrons form and interact via the strong force, known as Quantum ChromoDynamics (QCD). QCD is our current best theoretical model of the strong interaction, and it indicates that the strong force mediates reactions between objects with a “colour” charge. This is a fundamental principle in hadron physics, and using this colour charge tells us what hadrons can be formed. A hadron must be neutral when it comes to colour charge, or another way to say this is that it must be "white" when the colour charges are combined, either three colours combine to make that (red, blue and green) or a colour and its anti-colour (green and anit-green respectively for example). These colour charges mean QCD follows colour SU(3) symmetry group rules, this comes from there being eight possible gluon configurations shown in Equation 1.1. With three colours and three anti-colours, one would imagine nine configurations, but the missing ninth is the colour singlet gluon, which does not exist [15]. If the colour-neutral gluon existed, we would have an unconfined gluon given the strong force and infinite range [18].

$$r\bar{b}, r\bar{g}, b\bar{r}, b\bar{g}, g\bar{r}, g\bar{b}, \frac{1}{\sqrt{2}}(r\bar{r} - b\bar{b}), \frac{1}{\sqrt{6}}(r\bar{r} + b\bar{b} - 2g\bar{g}) \tag{1.1}$$

Where r is red, b is blue, g green and $\bar{r}$, $\bar{b}$ and $\bar{g}$ are the corresponding anti-colours. Additional to this colour symmetry [15], there is an approximate flavour symmetry, again belonging to an SU(3) group, of the up, down and strange quarks (uds) and the corresponding anti-quarks ($\bar{u}\bar{d}\bar{s}$) and from this comes our ability to place hadrons into groups that have the same hadron type (meson, baryon, etc.), total angular momentum (J) and parity (P). The total angular momentum J of a hadron is the sum of the intrinsic spin of the valence quarks and the angular momentum L between them. The parity P is combined by multiplying all parties together. Quarks have an intrinsic parity of +1, and antiquarks have an intrinsic parity of -1, then there is the parity from the angular momentum between quarks $(-1)^L$, although this hides within it an extra complexity as once you go above a two quark system there are multiple Ls to consider.

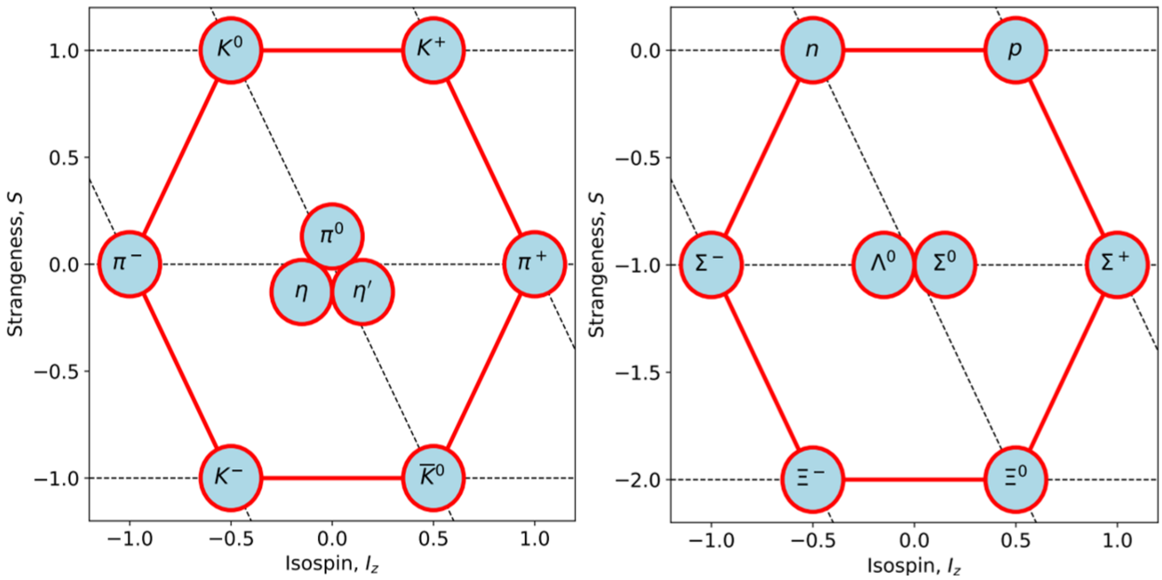

Fig. 1.4 The $J^P = 0^+$ nonet of mesons and $J^P = \frac{1}{2}^+$ octet of baryons. Both have strangeness as the y-axis and the third projection of isospin as the x-axis.

These groups of hadrons are known as multiplets. To understand them, an explanation of how they are constructed is needed [19]; therefore, one needs a description of Isospin and hypercharge. Isospin is a quantum number that is actually a vector, however, only the total isospin I and the third projection of isospin I_3 are considered here. I_3 is formally defined by Equation 1.2 a result of u and d quark symmetry, a subset of the aforementioned flavour symmetry. Total isospin I is related to the number of hadron states N with a particular J^p and hypercharge (members of the same row in the multiplet) in the following way $I = \frac{1}{2}(N-1)$. Then I_3 ranges from $-I$ to I, ascending by one each time as you go from left to right of the row.

$$I_3 = \frac{1}{2}(n_u - n_d) \tag{1.2}$$

Where n_u is the number of valence u quarks and n_d is for the number of d quarks.
Then, we have hypercharge, which is defined by Equation 1.3. It is simply the combination of all the hadron-specific quantum numbers.

$$Y = B + S + \frac{C - B' + T}{3} \tag{1.3}$$

Where Y is the hypercharge, B is the baryon number, S is the strangeness (strange quarks carry a strangeness of -1 and +1 is the strangeness of anti-strange quarks), C is the charm (charm quarks have +1 charm and anti-charm quarks have -1 charm), B' is beauty (bottom quarks have beauty of -1 and anti-bottom quarks have beauty of +1) and T is the topness (top quarks have topness of +1 and anti-top quarks have a topness of -1). For this research, the strangeness and baryon number are the most important. Therefore, a reduced version of hypercharge is used in this thesis:

$$Y = B + S \tag{1.4}$$

As stated by Equation 1.4 none of the particles analysed have non-zero charm, beauty or topness. In fact, a wider statement regarding hadron physics is that top quarks (and the corresponding anti-quarks) cannot form hadrons. This is due to the lifetime of the top quark being too short to form hadrons; it is measured to decay in 5×10^{-25} s [20], but as mentioned earlier, the range of the strong force is about 10^{-15} m. As the strong interaction is limited to acting over this distance at $c \approx 3 \times 10^{8}$ ms^{-1}, it can be calculated that the minimum time to form a strong bond between quarks is $\sim 10^{-23}$ s, two orders of magnitude larger than the predicted lifetime of the top quark. With the definitions of isospin and hypercharge, the multiplet can be fully understood. The y-axis is hypercharge (strangeness in the case of Figure 1.4) increasing, and the third isospin projection is along the x-axis. The electromagnetic charge is increasing along the diagonal between those two axes, which shows how I_3 and electromagnetic charge are related.

QCD is able to describe how colour-charged objects interact at very high energies accurately. However, it is very difficult to calculate how colour-charged objects interact at low energies. Unfortunately, it is in this low-energy regime that the vast majority of the interactions that directly influence the world around us occur. It is also these low-energy interactions that are responsible for the properties and behaviour of atomic nuclei. Connecting the observed behaviour of nuclei to the fundamental theory of QCD that underpins the interaction of their constituent parts is one of the major unresolved issues in modern physics. A major mission of modern hadron physics is trying to gain insight into the QCD many body problem through the lens of understanding the internal structure of hadrons. A pathway to this is exotic states including but not limited to tetra, penta and hexaquarks, the first two being difficult to separate from conventional background channels. The hexaquark search suffers less from this as from simple baryon number conservation; there is a limitation on possible interactions.

Feynman Diagrams

Richard Feynman introduced Feynman Diagrams in 1949 [21]. They were originally used to visually represent the various order corrections for the calculations of scattering cross-sections in particle physics. The simplicity of the diagrams streamlines such calculations as one can draw some diagrams of increasing complexity and can quickly estimate what order correction is needed. In a basic view, the more vertices (points where two fermions meet a force-propagating boson) a diagram has, the less that particular diagram contributes to the total cross-section [15]. This research has used it in this simplistic way, but in this thesis, Feynman diagrams have been used to represent hexaquark structure in more detail or to represent particle decay channels visually. The diagram conventions used in this thesis are summarized in Figure1.5.

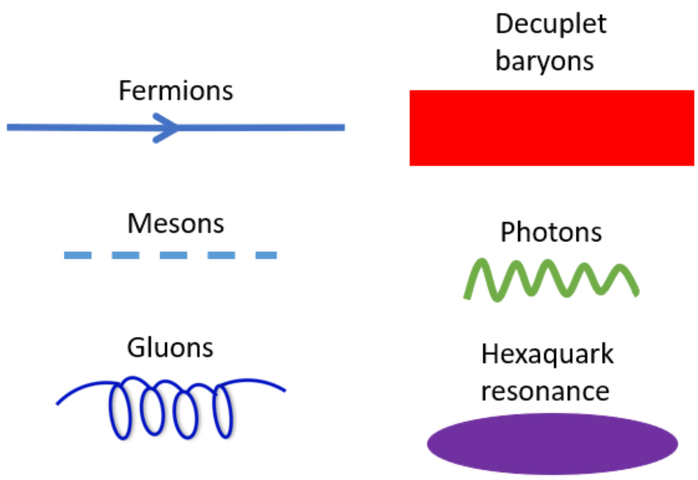

Fig. 1.5 Labelled summary of the Feynman diagram conventions used in this thesis. Solid blue lines and fermions such as electrons, quarks and $J^P = \frac{1}{2}^+$ octet baryons. Mesons are the dashed blue lines, and gluons are the curved lines that resemble a spring. The $J^P = \frac{3}{2}^+$ decuplet baryons are the red rectangles, green curved lines similar to sin waves are photons both real and virtual, and the purple ovals represent hexaquark resonances.

1.3 Hadron Spectroscopy

A large number of baryon and meson resonances have been discovered over the last two decades. There have also been several tetra and pentaquark candidates with experimental evidence but not confirmed. The first serious candidate was the X(3872), a potential tetraquark [22]. Although the goal of hadron spectroscopy is not to "stamp collect", the goal is aided by this. By measuring the masses, widths, cross-sections and other properties of these resonances, we can gather a much better understanding of QCD. The discovery and further analysis of these hadron resonances is done through various scattering experiments, both collider and fixed target (fixed target electron scattering is used in this research). From those scattering experiments, measurements can be made from a "bump hunt" style analysis (Section 3.3), but often more useful is the use of polarization observables. After this hadron physics overview, a more detailed look into the specific sub-field of hadron spectroscopy is appropriate at this point.

1.3.1 Electroproduction

As mentioned above, fixed target electron scattering experiments are used to gather the data used in this thesis. More precisely, the data is taken from meson electroproduction experiments. The kinematics of electroproduction are illustrated in Figure 1.6; it differs from photoproduction most fundamentally by the use of an electron beam that, after scattering, produces a virtual photon instead of a real one. The defining feature of a virtual particle is that its mass is different to the mass of the associated real version [15] and for the specific case of the virtual photon, this manifests in it having a mass at all, in stark comparison to its massless real counterpart [23].

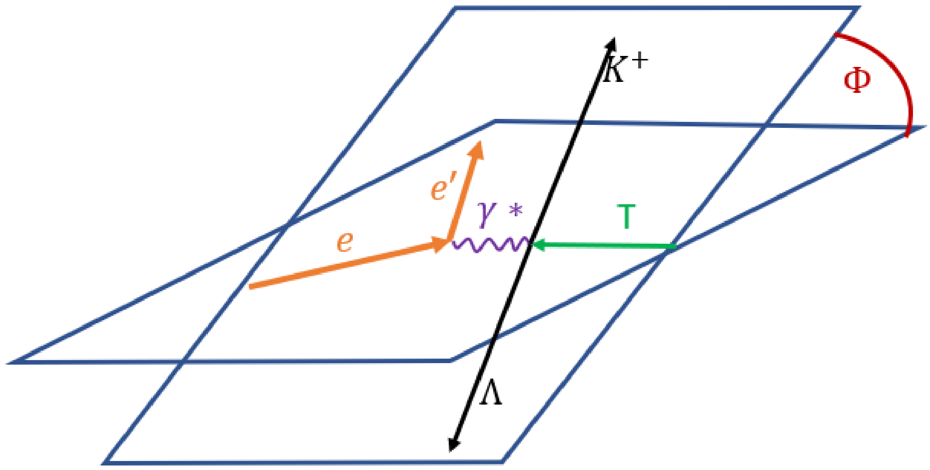

Fig. 1.6 The kinematics of electroproduction.

This virtual photon produced by the electron scattering impinges on the target (T) in the electron scattering plane. This will form some unknown (till further investigation) resonance, which later decays into a baryon and meson (Λ and K^+ chosen for Figure 1.6 as it is relevant to this thesis). The meson and baryon travel in the hadron production plane, which has a rotational offset from the electron scattering plane of angle ϕ. Electroproduction is different to photoproduction in the type and number of polarization observables that can be extracted. This comes from the fact that the virtual photon can exchange longitudinal polarization and, therefore, also produces observables from the interference of longitudinal and transverse polarization [23].

1.3.2 Polarization

When it comes to scattering experiments, the cross-section is the ideal measurement to make; seeing how it changes under different experimental conditions and pairing that with an accurate model can give great insight into the resonance being pursued. These models involve partial wave analysis [24, 25], and this can show how polarization is intrinsically linked to the angular momentum and spin of resonances. This link comes directly from the definition of the two major categories of polarization, transverse and longitudinal. The longitudinal polarization of a particle is essentially a statistical measure of how its spin aligns with its momentum vector [24]. Then transverse polarization is a degree of spin vector alignment but along two different vectors, one normal to the momentum vector within the hadron production plane and one normal to the hadron production plane itself [26]. Polarization is, therefore, folded into the differential cross-section for a reaction. To see precisely how one must look at Equation 1.5 to see the differential cross-section for ΛK^+ virtual photoabsorption (the electroproduction cross-section is then the product of this and the virtual photon flux) [27].

$$\begin{aligned}\frac{d^2\sigma_v}{d\Omega_K^{CM}} =& KS_\alpha S_\beta[R_T^{\beta\alpha} + \varepsilon R_L^{\beta\alpha} + \sqrt{\varepsilon(1+\varepsilon)} \times ({}^cR_{LT}^{\beta\alpha}\cos\phi + {}^s R_{LT}^{\beta\alpha}\sin\phi) \\ & + \varepsilon({}^cR_{TT}^{\beta\alpha}\cos 2\phi + {}^s R_{TT}^{\beta\alpha}\sin 2\phi) + h\sqrt{\varepsilon(1-\varepsilon)}({}^cR_{LT'}^{\beta\alpha}\cos\phi + {}^s R_{LT'}^{\beta\alpha}\sin\phi) \\ & + h\sqrt{1-\varepsilon^2}R_{TT'}^{\beta\alpha}]\end{aligned} \tag{1.5}$$

Where K is the ratio between kaon momentum and the virtual photon momentum both in the centre of mass (CM) reference frame, $S_{\alpha/\beta}$ are the spin projection operators, the sub and superscripts α and β are used to refer to the target and Λ polarization observables the summation over these observables is implied (see Table 1.2), $R_A^{\alpha\beta}$ where A can be T, L, LT, TT, LT' or TT' are the response functions summarised in Table 1.2, h is the helicity of the electron beam, ε is the polarization of the virtual photon given by Equation 1.8 and ϕ is the azimuthal angle between the hadron production plane and the electron scattering plane (these are defined in Figure 5.1).

$$\begin{aligned} S_\alpha &= (1, \mathbf{S}) \\ \mathbf{S} &= (S_x, S_y, S_z) \end{aligned} \tag{1.6}$$

$$\begin{aligned} S_\beta &= (1, \mathbf{S}) \\ \mathbf{S} &= (S_{x'}, S_{y'}, S_{z'}) \end{aligned} \tag{1.7}$$

Above are the definitions of the spin projection operators. For a full description of the x, y, z and x', y', z' axes, see Section 3.4.2.

$$\varepsilon = \left[1 + 2\left(1 + \frac{\nu^2}{Q^2}\right)\tan^2\frac{\theta_{e'}}{2}\right]^{-1} \tag{1.8}$$

Where ν is the virtual photons' energy given by the difference between electron beam or incident electron energy and the energy of the scattered electron ($E_{beam} - E_{e'}$), Q^2 is the four-momentum transfer defined by $Q^2 = -(\boldsymbol{e}_{beam} - \boldsymbol{e'})^2$, with $\boldsymbol{e}_{beam}$ being the four-vector of the electron beam and $\boldsymbol{e'}$ is the four-vector of the scattered electron, and $\theta_{e'}$is the polar angle of the scattered electron, relative to the beam direction.

Table 1.2 All of the response functions for pseudoscalar meson electroproduction. The rows are in the following order: the unpolarized functions in the first row, the next three are target polarization observables, the three after that are recoil observables, and the final rows are the combined target and recoil polarization observables. The columns show the recoil component axes and the target component axes (β and α respectively). Then the remaining columns are the transverse, longitudinal, longitudinal-transverse inference, transverse-transverse interference, and the last three columns need the electron to be polarized. The asterisks represent functions that are non-zero but are related to the other response functions [23].

β	α	T	L	${}^cLT$	${}^sLT$	${}^cTT$	${}^sTT$	${}^cLT'$	${}^sLT'$	TT'
		R_T^{00}	R_L^{00}	R_{LT}^{00}	0	R_{TT}^{00}	0	0	$R_{LT'}^{00}$	0
	x	0	0	0	R_{LT}^{0x}	0	R_{TT}^{0x}	$R_{LT'}^{0x}$	0	$R_{TT'}^{0x}$
	y	R_T^{0y}	R_L^{0y}	R_{LT}^{0y}	0	*	0	0	$R_{LT'}^{0y}$	0
	z	0	0	0	R_{LT}^{0z}	0	R_{TT}^{0z}	$R_{LT'}^{0z}$	0	$R_{TT'}^{0z}$
x'		0	0	0	$R_{LT}^{x'0}$	0	$R_{TT}^{x'0}$	$R_{LT'}^{x'0}$	0	$R_{TT'}^{x'0}$
y'		$R_T^{y'0}$	*	*	0	*	0	0	*	0
z'		0	0	0	$R_{LT}^{z'0}$	0	$R_{TT}^{z'0}$	$R_{LT'}^{z'0}$	0	$R_{TT'}^{z'0}$
x'	x	$R_T^{x'x}$	$R_L^{x'x}$	$R_{LT}^{x'x}$	0	*	0	0	$R_{LT'}^{x'x}$	0
x'	y	0	0	0	*	0	*	*	0	*
x'	z	$R_T^{x'z}$	$R_L^{x'z}$	*	0	*	0	0	*	0
y'	x	0	0	0	*	0	*	*	0	*
y'	y	*	*	*	0	*	0	0	*	0
y'	z	0	0	0	*	0	*	*	0	*
z'	x	$R_T^{z'x}$	*	$R_{LT}^{z'x}$	0	*	0	0	$R_{LT'}^{z'x}$	0
z'	y	0	0	0	*	0	*	*	0	*
z'	z	$R_T^{z'z}$	*	*	0	*	0	0	*	0

For the purposes of this research, due to the unpolarized target and the longitudinally polarized electron beam, the virtual photoabsorption differential cross-section from Equation 1.5 can be rewritten into the form seen in Equation 1.9.

$$\frac{d^2\sigma_v}{d\Omega_K^{CM}} = \sigma_0(1+\rho_{x'}^0 S_{x'} + \rho_{y'}^0 S_{y'} + \rho_{z'}^0 S_{z'}) \tag{1.9}$$

$$\sigma_0 = K[R_T^{00} + \varepsilon R_L^{00} + \sqrt{\varepsilon(1+\varepsilon)}R_{LT}^{00}\cos\phi + \varepsilon R_{TT}^{00}\cos 2\phi] \tag{1.10}$$

Where σ_0 is the unpolarized cross-section (defined in Equation 1.10) and ρ_i^0 (where i is x', y' or z') is the polarization component with respect to the axis chosen (explained in detail in Section 3.4). These polarization components can be represented in terms of their response functions seen in the equations below.

$$
\begin{aligned}
\rho_{x'}^{0} &= \frac{K}{\sigma_0}(\sqrt{\varepsilon(1+\varepsilon)}R_{LT}^{x'0}\sin\phi + \varepsilon R_{TT}^{x'0}\sin 2\phi) \\
\rho_{y'}^{0} &= \frac{K}{\sigma_0}(R_{T}^{y'0} + \varepsilon R_{L}^{y'0} + \sqrt{\varepsilon(1+\varepsilon)}R_{LT}^{y'0}\sin\phi + \varepsilon R_{TT}^{y'0}\sin 2\phi) \\
\rho_{z'}^{0} &= \frac{K}{\sigma_0}(\sqrt{\varepsilon(1+\varepsilon)}R_{LT}^{z'0}\sin\phi + \varepsilon R_{TT}^{z'0}\sin 2\phi)
\end{aligned}
\tag{1.11}
$$

For the purposes of this research, it is necessary to integrate Equation 1.9 with respect to ϕ over the range of 0 to 2π or 360°. This alters the polarization relations to be in the form shown below.

$$
\begin{aligned}
P_{x'}^{0} &= 0 \\
P_{y'}^{0} &= \frac{K}{\sigma_0}(R_{T}^{y'0} + \varepsilon R_{L}^{y'0}) \\
P_{z'}^{0} &= 0
\end{aligned}
\tag{1.12}
$$

With these new relations, along with the ϕ integrated σ_0 it is now possible to get this:

$$
\int_0^{2\pi} \frac{d^2\sigma_v}{d\Omega_K^{CM}} d\phi = 2\pi K(R_T^{00} + \varepsilon R_L^{00})(1 + P_{y'}^{0} S_{y'}) \tag{1.13}
$$

This makes it clear why $P_{y'}$ is the polarization component used for the search for experimental evidence for the singly strange hexaquark and why the other components are used for compare and contrast purposes. Getting more specific now with a look at exotic hadron physics.

1.4 Exotic Hadron Spectroscopy

As discussed in Section 1.3, lots of recent work has been done in the realm of exotic hadron spectroscopy, including various potential tetra and pentaquark candidates being measured [28]. This work technically started before the quark model of hadrons was developed with the $\Lambda(1405)$ first predicted in 1959 [29] and first measured in 1961 [30]. Then, the possibility of it being a pentaquark was proposed in this paper [31].

But even before the $\Lambda(1405)$ was proposed as a pentaquark, multiquark states including tetraquarks and pentaquarks were proposed as a possibility by Gell-Mann [10]; after that, tetraquark states were discussed in 1977 [32, 33] and following that, pentaquark states were proposed in 1987 [34, 35]. With that comes the studies for the singly strange pentaquark candidate the $\Lambda(1405)$ via the $\gamma n \to K^+K^-n$ reaction [36, 37]. Although this and other singly strange pentaquark searches were initially producing encouraging results from photoproduction and electroproduction off of proton and deuteron (neutron and proton) targets, along with neutrino bubble chamber experiments, K^+ neutron scattering, lepton-lepton scattering and proton-proton scattering [38]. Despite this, higher statistics experiments did not turn up any positive results for the pentaquark. A similar story can be told concerning the tetraquarks. For example, the aforementioned X(3872) which was first observed in 2003 [22]. That observation, along with later measurements [39], lead to the idea of this state being

a tetraquark. However, with its mass being so close to that of a D^0 and $\bar{D^0}*$, the idea of the X(3872) being a molecule of these two particles was proposed. After all of these studies, it is still an open question whether or not pentaquarks exist; the same can be said for the other multiquark states, the tetraquarks and hexaquarks.
When it comes to the multiquark states, one of the major issues related to the confirmation of the existence of tetraquarks and pentaquarks is the potential results being hidden by having low statistics amongst a large background. One of the advantages that the hexaquark search has over this one is the fact that due to baryon conservation, it cannot be formed off of a singular nucleon target; it is a baryon number two ($B = 2$) state and must come from a $B = 2$ state. Therefore, many conventional background channels are cut out from the search. With the major background covered it is a good place to talk about the main focus of this thesis and some motivation for it.

1.5 Hexaquarks

A hexaquark is any object with either six valence quarks or three quarks and three anti-quarks, and the first of such states to be discovered is, unsurprisingly, the deuteron [40]. There were then various theoretical works done to explore the possible existence of non-trivial hexaquarks [41]. The first of these to have experimental evidence for its existence is the $d^*(2380)$, this state consists of six "regular" quarks (uuuddd), as opposed to the state being made of three quarks and three antiquarks. The first signs of the $d^*(2380)$ came from the WASA-at-COSY collaboration in 2011 [42].

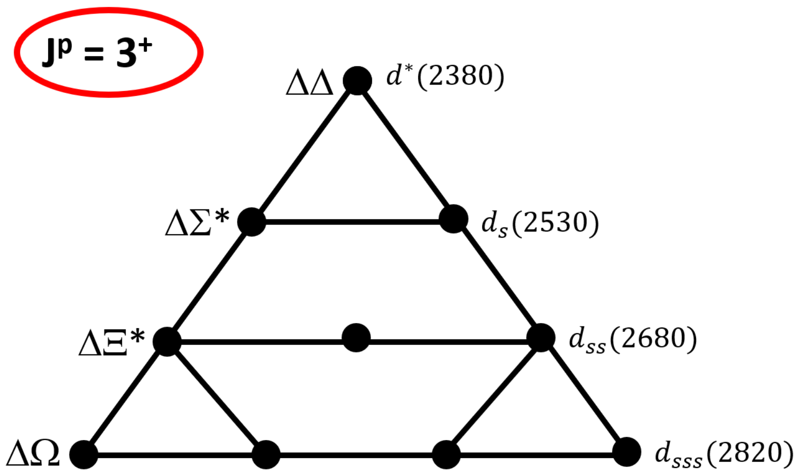

Fig. 1.7 The multiplet that the d^* and d_s^0 belong to, labelled with hexaquark name and mass on the right, and the most probable decuplet-decuplet baryon decay on the left.

Since then, all of the branching ratios for all decays have been measured through various nucleon-nucleon scattering experiments [43, 44, 45, 46, 47], almost assuring its existence. To further the understanding of the $d^*(2380)$, its electromagnetic properties have been measured with photoexcitation from deuteron targets [48, 49, 50]. This thesis outlines the search for another non-trivial hexaquark, more precisely, the first strange hexaquark. Known as the d_s as this particle in question belongs to the $J^P = 3^+$ multiplet seen in Figure 1.7 along with the $d^*(2380)$ [51]. A parallel research question to the one of whether or not these states exist is the question of what structure they have. There are two main models of the possible structure of these objects. There is the genuine hexaquark model, where all six quarks are in a single quark bag. Then there is the molecular model, where the two baryons form a molecule, keeping the two quark bags separate.

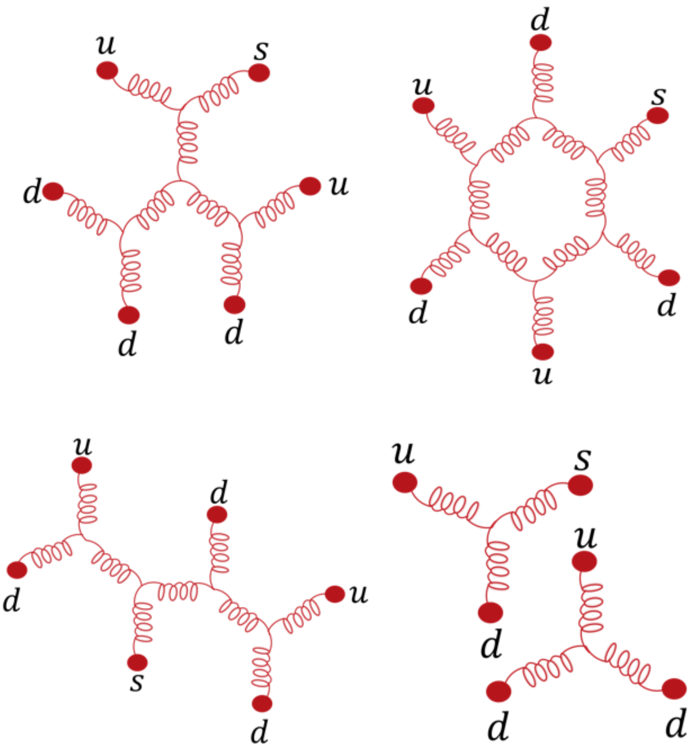

Fig. 1.8 The four configurations of the d_s^0 assuming a genuine hexaquark model. The solid dots here are the quarks connected by the gluons. The bottom right is the fully overlapped molecule configuration that the hexaquark is predicted to be in 20% of the time [52].

The models are not completely separated, as the genuine hexaquark model involves the particle being in a superposition of four possible quark-gluon interaction states, one of which is the molecule configuration, but the two baryons overlap fully.

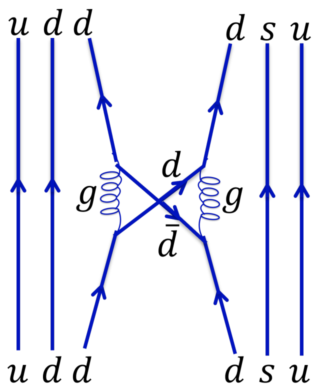

Fig. 1.9 The d_s^0 hexaquark structure on a quark level. The Δ^0 (udd) being bound to the Σ^{*0} (dsu) via the exchange of a π^0 ($d\bar{d}$).

Figure 1.8 shows all the genuine hexaquark structure possibilities for the d_s^0, these diagrams along with Figure 1.9, help to explain how measuring the Binding Energy (BE) can be used to assist in answering the question of structure. Due to the genuine hexaquark being bound by quark-gluon interactions, specifically the colour magnetic interaction, which is repulsive in this case and inversely proportional to the quark mass. Therefore, in the case of the genuine hexaquark, as strangeness increases, the particle becomes more tightly bound. Conversely, the molecule model has two baryons bound by pion exchange. As this is a strong interaction, it must conserve quark flavour, and therefore, strange quarks cannot exchange pions. This means the stranger the hexaquark, the weaker the binding energy.

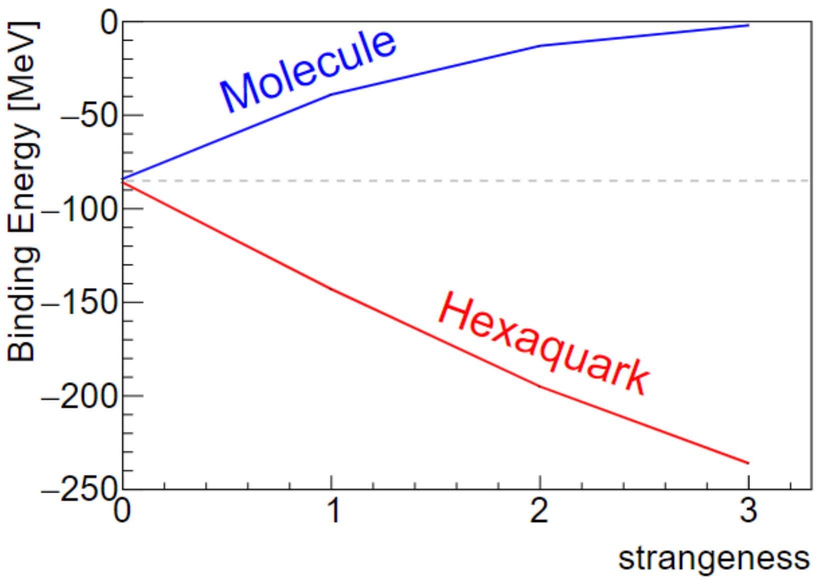

Fig. 1.10 Two plots indicating the trend of the BE of the hexaquarks as the number of strange quarks increases. The blue line is when considering a pure molecule structure, and the red line is when considering the structure to be a pure, genuine hexaquark.

This relation between BE and the strangeness of the hexaquarks for both structure models is summarised well by Figure 1.10; it also illustrates the importance of the efforts to find all members of the $J^p = 3^+$ multiplet. To measure the BE, one must measure the mass of the hexaquark because the BE is the difference between that mass and the mass of constituent baryons. More accurately, using Clebsch-Gordon coefficients to combine a specific ratio of the masses of particular $J^p = \frac{3}{2}^+$ decuplet baryons (a good reference on how to calculate this is [19]). Imperative to the search, then, is understanding the possible decay channels along with the theoretical mass and width of the d_s. This is covered in Section 3.1.

1.6 Summary

To conclude, the major motivation of this research is using the efforts to gather experimental evidence of this d_s singly strange hexaquark to explore many-body physics in QCD further. We can study this with greater ease than other pursuits in exotic hadron spectroscopy due to the requirement for a baryon number of two being a barrier to contamination by conventional background channels. In essence, measurements on the d_s would allow for a deeper understanding of the structure of all the $J^p = 3^+$ anti-decuplet hexaquarks, giving insight into hadron structure physics. With the understanding of why this research is being carried out it is appropriate to now discuss how it will be done.

Chapter 2

Experiment

This chapter will provide an overview of the Thomas Jefferson Laboratory, which is the experimental facility that houses the experiment known as CLAS12. This was the experiment which was used in the collection of the data necessary for this research. It will also give a detailed discussion of the experimental setup that allowed for this work to be carried out. Covering the various detector systems, with descriptions of the principles behind their operation, coverage of the systems, what they detect and the associated resolutions and/or efficiencies of the systems. Finishing this chapter will be a discussion of the data collection and trigger systems of CLAS12.

2.1 Jefferson Laboratory and CEBAF

Fig. 2.1 Aerial photo of CEBAF at JLab.

All of the experimental data analysed by the author was taken at the Thomas Jefferson Laboratory (JLab). JLab is a national accelerator facility run by the U.S. Department of Energy Office of Science. Situated on the JLab site is CEBAF, pictured in Figure 2.1, which is the Continuous Electron Beam Accelerator Facility, consisting of two anti-parallel linear accelerators (linacs) in a re-circulation setup currently capable of accelerating the electron beam to a maximum energy of 12 GeV.

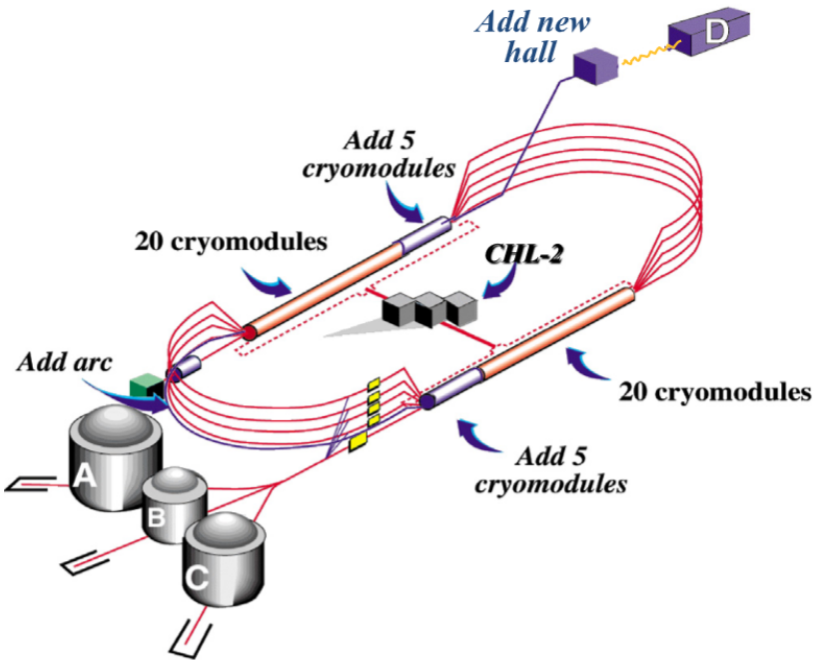

Fig. 2.2 Diagram of CEBAF with the experimental halls and some key components and major parts of the 12 GeV upgrade labelled [53].

Originally designed to deliver a 4 GeV electron beam, in 1984, construction began, and by the mid-90s, initial operation commenced. Very quickly came the upgrade to 6 GeV by the year 2000, and today, the facility runs at a maximum energy of 12 GeV. Summarised in Figure 2.2 are the major operational components with the requirements of the 6 to 12 GeV upgrade, which are now in effect.
An outline of the operation of CEBAF follows. A 2 W laser is directed onto a small piece of gallium-arsenide on the order of a few nm [54], ionizing the atoms and producing the electrons for the beam. The injector sends the electrons into the accelerator to start the first of 5 to 5.5 passes of the full 1.4 km circumference accelerator. On each half pass, the beam travels through 25 Radio Frequency (RF) cavities utilizing superconducting RF (SRF) technology to accelerate the beam in the linac. Once the beam has made it through the first linac, the magnets in the arcs seen in Figure 2.2 turn the beam 180° into the next linac. This process repeats to make a full pass. After a maximum of 5 of those full passes (dependent on experimental requirements), the beam is released into the 3 original experimental halls A, B and C. The newer hall D gets an extra half pass and, therefore, is the only hall capable of receiving the maximum energy of 12 GeV.

2.2 CLAS12 Experiment Setup

Housed within experimental Hall B is CLAS12, which stands for the CEBAF Large Acceptance Spectrometer, and the 12 represents the aforementioned maximum electron beam energy of 12 GeV, which, after being delivered by CEBAF, is fired incident upon a stationary target (liquid hydrogen and deuterium are relevant for this research). A surface-level breakdown of the detector is into three major regions, going in order of increasing polar angle first the Forward Tagger (FT) not shown in Figure 2.3 due to it being hidden by other components. Then, the Forward Detector (FD), which is the yellow component labelled HTCC and all parts forward (left) of that. Finally, there is the Central Detector (CD), which is comprised of the detector systems that are radially inward from the HTCC.

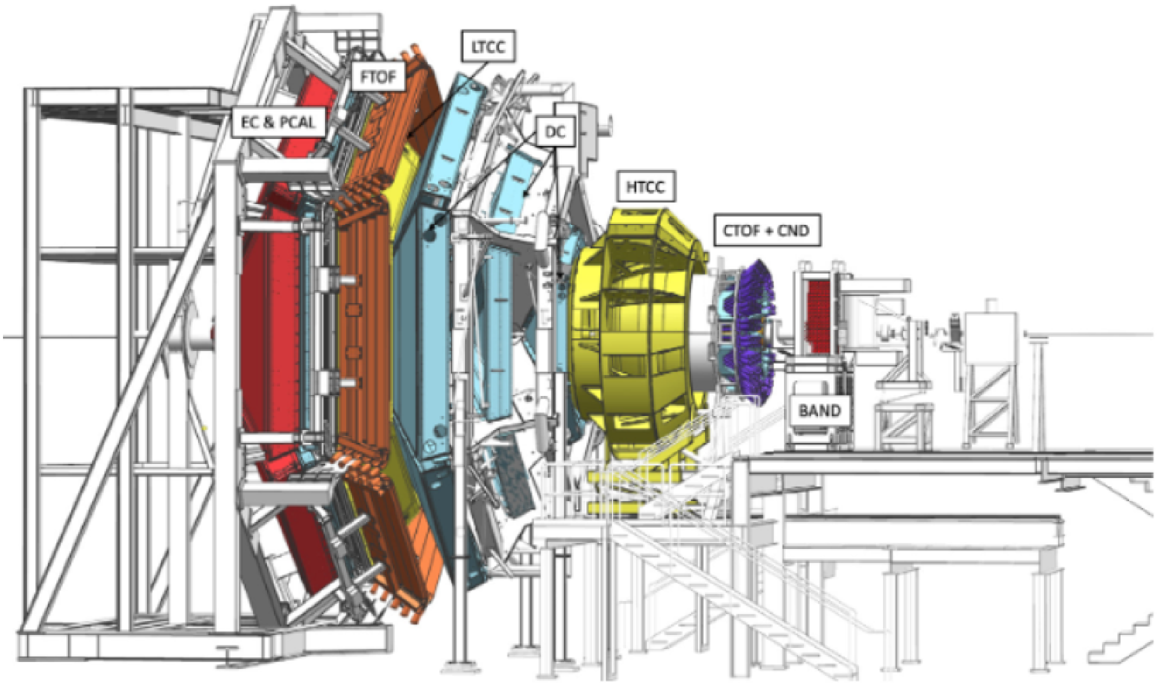

Fig. 2.3 CLAS12 with separate key components labeled [53].

2.2.1 Forward Tagger

The FT is for designed the detection of electrons or photons close to the beamline, with a polar angle (θ) range of 2.5° to 4.5°. With scattered beam electrons at this angular range, the Q^2 (four-momentum transfer) is small, and therefore, trigger electrons detected by the FT are responsible for initiating quasi-real photoproduction reactions.
To properly reconstruct the quasi-real photon, four variables are needed, the scattered electron energy ($E_{e'}$) in order to get the energy of the photon (E_γ) using Equation 2.1.

$$E_\gamma = \nu = E_{beam} - E_{e'} \tag{2.1}$$

Where ν is the energy of the photon, E_{beam} is the energy of the beam and $E_{e'}$ is the energy of the reconstructed electron. These measurables are then used in Equation 2.2 to extract an approximate value for the polarization of the photon.

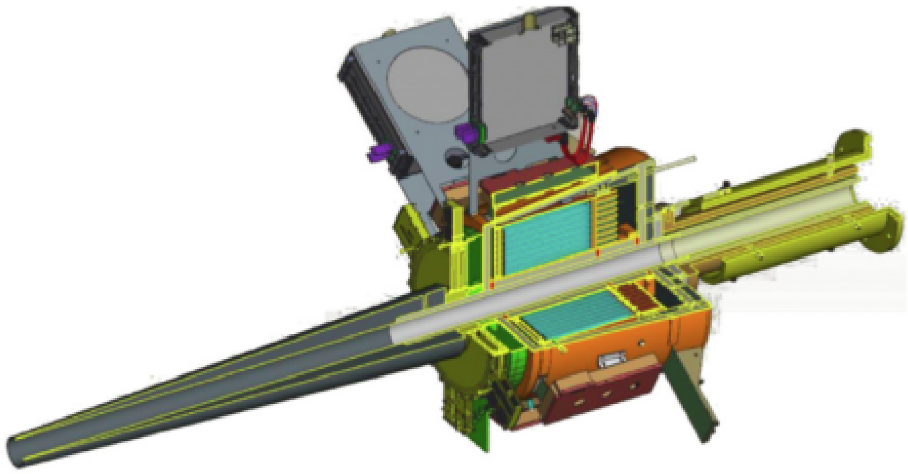

Fig. 2.4 CAD drawing of the FT, showing two of the main components, the calorimeter in cyan and the tracker is the green disk in front of the calorimeter [55].

$$P_\gamma = \varepsilon \sim \left(1 + \frac{\nu^2}{2E_{beam}E_{e'}}\right) \tag{2.2}$$

Where P_γ and ε are the polarization of the photon. The final two are angular measurements, the azimuthal angle $\phi_{e'}$ used to determine the polarization plane and the polar angle $\theta_{e'}$ to be used in Equation 2.3 to ascertain the Q^2.

$$Q^2 = 4E_{beam}E_{e'}\sin^2\left(\frac{\theta_{e'}}{2}\right) \tag{2.3}$$

These measurements come from the three main components of the FT, an electromagnetic calorimeter (FT-Cal) for the energy, a Micromegas tracker (FT-Track) for angular measurements and a hodoscope (FT-Hodo) for separation of electrons and photons [53, 56] some of which are seen in Figure 2.4.

FT-Cal

The FT-Cal measures the electromagnetic shower energy of the scattered beam electron in the range $0.5 \leq E_{e'} \leq 4.5$ GeV, making this measurement means using Equations 2.1 and 2.2 to determine E_γ and P_γ respectively. The FT-Cal also provides a fast trigger signal for quasi-real photoproduction reactions. To meet both of these requirements, scintillators are the chosen detector type, specifically lead tungstate ($PbWO_4$). In general, scintillators are detectors that produce a flash of light in response to a particle passing through it. Various interactions can be the source of this light, such as the photoelectric effect, Compton scattering, and particle anti-particle annihilation [57]. Then, in relation to this fast trigger signal, a fast recovery time is needed for the purpose of handling the high interaction rate, and the $PbWO_4$ crystals fulfil these timing requirements with a scintillation decay time of 6.5 ns. Another important requirement of the FT-Cal met by $PbWO_4$ is high shower containment to increase the accuracy of $E_{e'}$ measurements, and it accomplishes this by having a radiation length of 0.9 cm and Moliere radius of 2.1 cm. The FT-Cal is shown in Figure 2.5 it consists of an array of 332 $15 \times 15 \times 200 mm^3$ crystals in order to have full $\phi_{e'}$ coverage and $\theta_{e'}$ range 2° to 5°.

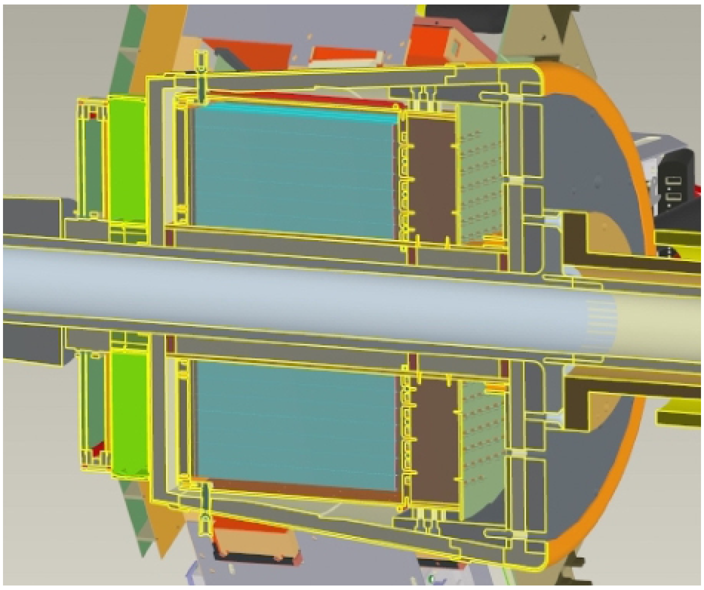

Fig. 2.5 CAD drawing of a cross-section of the FT-Cal with the $PbWO_4$ crystals in light blue. A full description of all components is in the reference [55].

FT-Track

The FT-Track is used to measure the two angles of the scattered electron $\phi_{e'}$ and $\theta_{e'}$, which are used the determine the remaining properties of the quasi-real photon, not determined by the FT-Cal. It makes these measurements through the use of micromegas trackers, which are detectors consisting of a cathode and anode separated by a region filled with a gas [55]. This gas gets ionized by a charged particle moving through it. The electrons drift towards the cathode, travelling through the '*amplification gap*', separated from the rest of the gas by the '*Micro-Mesh*'. As the electron gets close to the mesh, it experiences a large electric field ($\sim$ 100 kV/cm) and accelerates. This means it further ionizes the gas, creating more free electrons; they proceed to do the same, producing an avalanche effect. The charge is detected by readout strips separated by micrometres, giving positional resolution to the path of the initial incident electron; Figure 2.6 outlines this method.

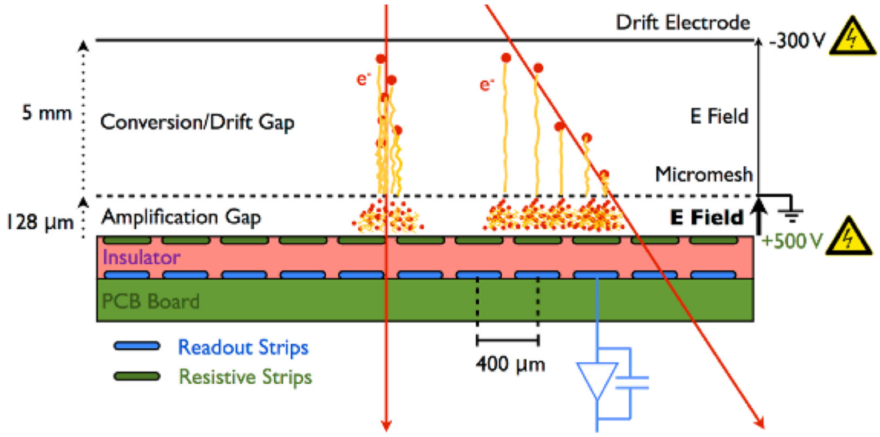

Fig. 2.6 Outline of the underlying operational principle of one of the six micromegas making up the FT-Track. The non-normal incident electron path (on the right) creates showers detected on different readouts at different times [56].

The specific arrangement of micromega detectors used for the FT-Track is two double-layer disks; the separate layers of one disk have readout strips oriented 90° to each other, giving an x and y position, pairing the coordinates provided by the readouts of each disk determines the angular measurements of $\phi_{e'}$ and $\theta_{e'}$. The design allows the FT-Track to have an excellent spatial resolution of $\sim 150\ \mu$m in both x and y.

FT-Hodo

With all four of the aforementioned variables needed to properly reconstruct the quasi-real photon directly measured or extracted through the use of the above two components, the FT-Hodo is used to separate signals coming from photons (γ) and electrons. It does this quite simply by assigning an electron as a signal in the FT-Hodo correlated in position and time with a hit in the FT-cal, whereas photons will be detected in the FT-Cal, but only a small fraction of them will be detected by the FT-Hodo, as the plastic scintillators used in the design are less responsive to photons due to the fundamental physical difference in how electrons and photons interact in matter. The electrons disturb electromagnetic fields as they move through the material on a continuous basis, whereas photons react with matter via a one-on-one basis. Figure 2.7 shows one of the two identical layers of scintillator tiles; each layer has 44 tiles with dimensions of $15 \times 15 \times 7$ mm^3 and 72 tiles with dimensions $30 \times 30 \times 15$ mm^3. The scintillator light is detected by Silicon Photo-Multipliers (SiPMs) [55].

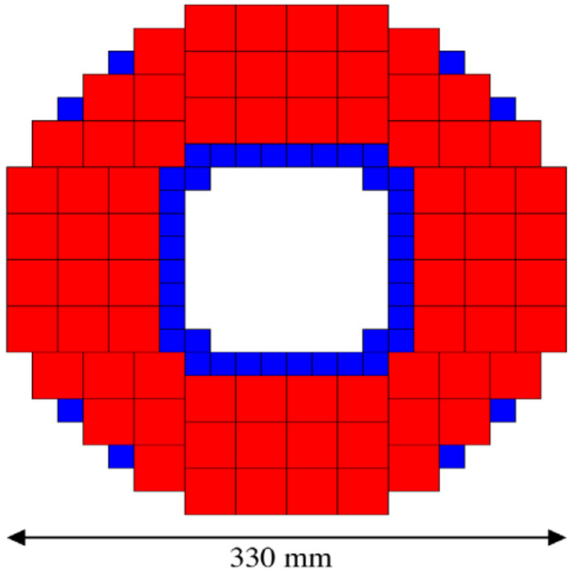

Fig. 2.7 2D picture of the configuration of the scintillator tiles of the FT-Hodo. The blue squares are the 15×15 mm^2 tiles and the red squares are the 30×30 mm^2 [55].

2.2.2 Forward Detector

The Forward Detector consists of Drift Chambers (DC) for trajectory and, therefore, momentum reconstruction of charged particles, Cherenkov detectors to separate electrons and pions, scintillators for measurement of the time of flight and calorimeters to detect electrons and high-energy neutrals. Not all of the detectors mentioned cover the same angular range. The Forward Time Of Flight (FTOF) system has the largest coverage of $5^\circ \leq \theta \leq 45^\circ$ [53, 58, 59].

DC

The DC is used to measure the momentum of charged particles in the polar angle range of $5^\circ \leq \theta \leq 40^\circ$. It consists of three regions, each of which is broken down into six sectors shown in Figure 2.8. This separate sector configuration makes for gaps in the ϕ acceptance giving 50% of 360° at $\theta = 5^\circ$ and 90% of 360° at $\theta = 40^\circ$ [53].

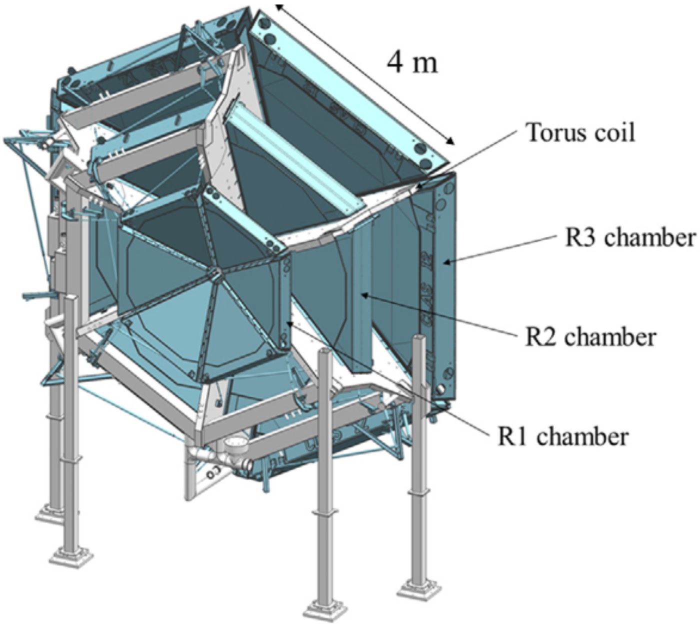

Fig. 2.8 Schematic of the CLAS12 DC. Clearly labelled are the three regions (R1, R2 and R3) and the position of one of the six torus coils [58].

In general terms, a DC works not unlike the micromegas described in Section 2.2.1, but instead of the gas-filled detector being sandwiched between an anode and cathode, the gas-filled (90:10 mix of argon and CO_2) region has several positively charged wires running through it. When a charged particle travels through this gas and ionizes it, the free electrons drift towards the wires, and an avalanche of electrons hits it. The charge is recorded along with a time to get several position measurements, and therefore, the path of the charged particle through the DC is inferred. The path is curved due to the magnetic fields, so this path can be used to reconstruct the momentum of the particle. The CLAS12 DC is set up in such a way that each sector contains two super layers, which consist of six layers of wires seen in Figure 2.9. These super layers are orientated $\pm 6°$ relative to the centre length of the sector.

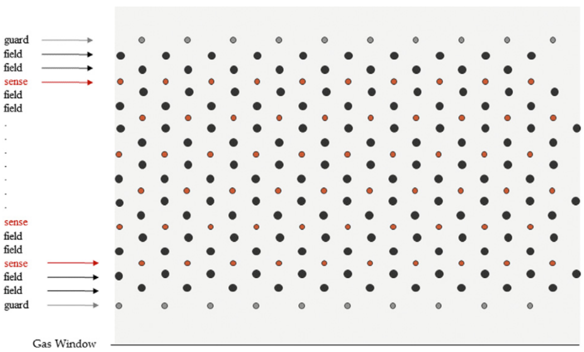

Fig. 2.9 Wire layout of a super layer, showing the hexagonal drift cells. The wires are arranged in such a way as to act like an infinite grid. [58].

This design allows the CLAS12 DC to meet the physics goals of having the excellent θ resolution of 1 mrad, ϕ resolution of 1 mrad$/\sin\theta$ and momentum resolution of $dp/p < 1\%$.

Cherenkov Counters

There are three different Cherenkov counters used in CLAS12. They are used for high-momentum particle species discrimination. They detect a phenomenon called Cherenkov radiation; this is where the charged particle is moving through a substance at a velocity $v > c/n$, where c is the speed of light and n is the material's refractive index. Moving at this velocity, faster than the speed of light in the substance, means the particle emits photons, known as Cherenkov radiation. First, there is the high threshold Cherenkov counter (HTCC); its purpose is to discriminate between electrons below 4.9 GeV and charged pions, kaons, and protons [53]. Achieving this through the use of CO_2 held at standard ambient temperature and pressure (SATP) 25°C and 1 atm. CO_2 in these conditions has an n such that charged pions produce Cherenkov radiation at momentum no lower than 4.9 GeV, so anything producing a signal with less momentum must be an electron with its lower mass but still travelling at the velocity required [60]. Figure 2.10 shows that the HTCC does not have blind spots with full 360°ϕ coverage, with 12 lots of 4 elliptical mirrors, giving the $5° - 35°\theta$ coverage. Each mirror matches up with a PMT used to amplify the light and produce a signal.

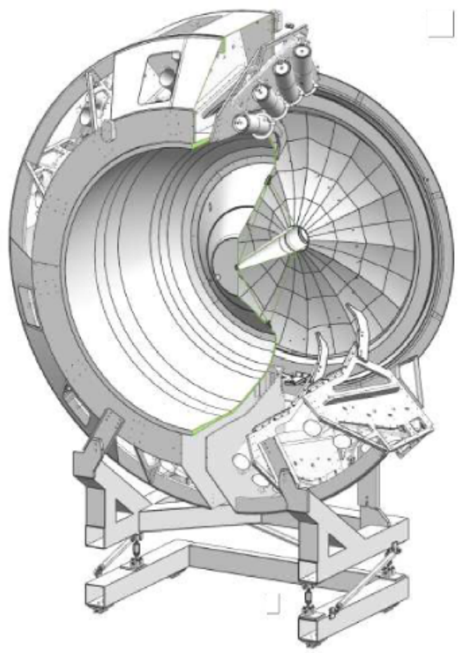

Fig. 2.10 Cut diagram of the HTCC. The elliptical mirrors can be seen in the back on the right. On the right at the top, four of the 48 PMTs can be seen [60].

Similar to the HTCC, there is the low threshold Cherenkov counter (LTCC) with the purpose of charged pion and kaon discrimination. The medium used in this case is C_4F_{10} which has a refractive index of $n = 1.00134$ and therefore charged pions can produce a signal at a minimum momentum of 3.7 GeV and charged kaons at 8.5 GeV [61]. Similar to the DC the LTCC is in sectors; however, as of writing this thesis, one of the six sectors is replaced by the ring imaging Cherenkov detector (RICH), which means there are gaps in the ϕ coverage, but there is a θ coverage of $5^\circ - 30^\circ$. In Figure 2.11, it can be seen how a single sector of the LTCC consists of 18 pairs of hyperbolic mirrors, elliptical mirrors, Winston light collecting cones and PMTs.

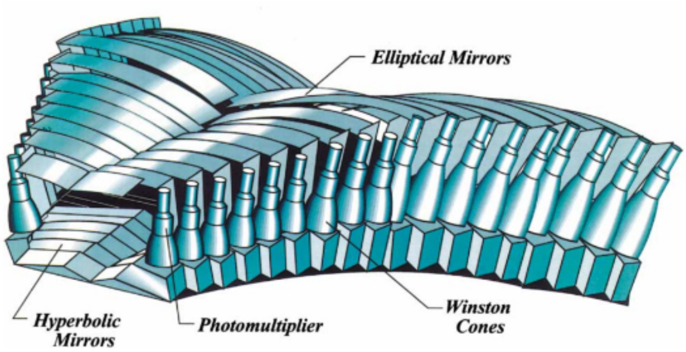

Fig. 2.11 A diagram of a single sector of the LTCC with the optics labelled [61].

Finally, we have the RICH used to separate charged pions from kaons in the momentum range 3 to 8 GeV [62]. Instead of there being a cut of momentum for pions and kaons on electrons and pions like the two Cherenkov counters described earlier, the RICH works by measuring the opening angle of the Cherenkov radiation emitted by the particle. The Cherenkov radiation opening angle can be used in conjunction with the momentum of the particle to determine the particle species shown in Figure 2.12. This is possible due to the aerogel being used as the medium in the RICH; it has a refractive index of $n = 1.05$ hence it having the lowest minimum momentum of all the detectors in this section. Figure 2.13 shows major parts of the RICH design; the 102 aerogel tiles, the spherical mirrors that reflect the Cherenkov radiation and the photon detector, which is small thanks to the mirrors reflecting the light to it no matter the point of origin. The RICH does have a particularly low angular acceptance, not only due to it being in just one of six possible sectors but in terms of the polar angle, compared to the polar coverage of the LTCC as it only covers a range of $5^\circ \leq \theta \leq 26^\circ$.

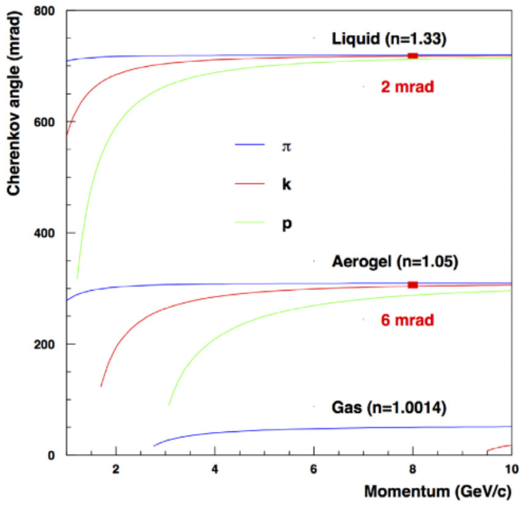

Fig. 2.12 Plot showing the relationship between the Cherenkov radiation opening angle and the momentum of the particle for three different substances: gas, water and then the aerogel used in the RICH. It can be seen how the aerogel provides the best separation between the three particles: pions (blue line), kaons (red line) and protons (green line) [62].

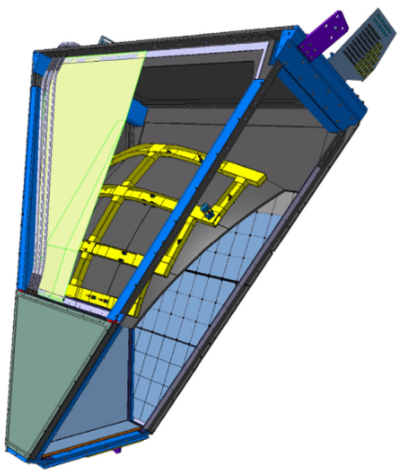

Fig. 2.13 Schematic of the RICH detector with various components highlighted. From left to right, on the top half are the exit panel, spherical mirror support and the mirrors. The grid on the right is the aerogel tiles, and on the bottom, the electronics panel can be seen. [62].

FTOF

The FTOF is used to measure the time of flight of charged particles in the polar angle region $5^\circ \leq \theta \leq 45^\circ$ and similar to the DC, the FTOF is made of six sectors and has similar ϕ coverage of 50% of 360° at $\theta = 5^\circ$ and 95% of 360° at $\theta = 45^\circ$ [59]. An overall look at the FTOF can be seen in Figure 2.14; for a more detailed picture, each sector of the FTOF consists of three panels; the first two in order of the downstream direction are panels 1b and 1a; these both cover the θ range of 5° to 35°.

The difference between panels 1b and 1a is; the number, size and makeup of the scintillator counters - used to measure the time a particle passed through the detector - panel 1b has 62 counters, all with a width and height of 6 cm and Lengths ranging from 17.3 cm to 407.9 cm. Panel 1a has 21 counters; these have a width of 15 cm, a height of 5 cm and lengths ranging from 32.3 cm to 376.1 cm. For the greater polar angular range of 35° to 45°, there is panel 2; it only has five counters, each with a width of 22 cm, a height of 5 cm and lengths ranging from 371.3 cm to 426.1 cm. The differences in each panel give them different timing resolutions, the average being 85 ps for 1b, 125 ps for 1a and 155 ps for 2. A combination of TOF and momentum is used for particle identification.

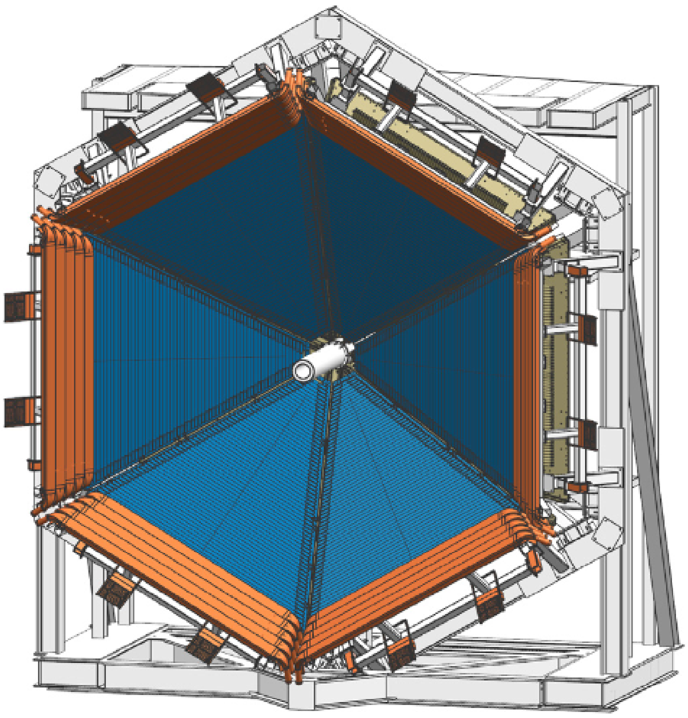

Fig. 2.14 Schematic of the FTOF, the blue triangular panels are the 1b panels, and behind them are the 1a panels not seen in this diagram. Then, the orange panels radially out from the 1b panels are the 2 panels [59].

Electromagnetic Calorimeters

There are two Electromagnetic calorimeters to make up the ECAL; there is the new pre-shower calorimeter (PCAL), and then just behind that is the old CLAS electromagnetic calorimeter (EC); the ECAL is used for the detection of electrons, photons and neutrons [53]. Both the PCAL and EC have six sectors each sector covers a polar angle range of $5^\circ \leq \theta \leq 35^\circ$ and together they cover an azimuthal angle ϕ of 50% of 360° at $\theta = 5^\circ$ and 85% of 360° at $\theta = 35^\circ$. Each of the sectors in both parts of the ECAL is constructed in a similar way; there are three alternating triangular scintillating layers, each with differently oriented scintillating strips on them. The three types of layers are U, where the strips are parallel to V's PMT readout side, W, where the strips are parallel to U's PMT readout side and W, where the strips are parallel to the top of the triangle. Every scintillation layer is separated by a lead layer which is illustrated in Figure 2.15. The specifics of the layering are different for the PCAL and EC; the PCAL has 15 scintillating layers, and the EC has 39.

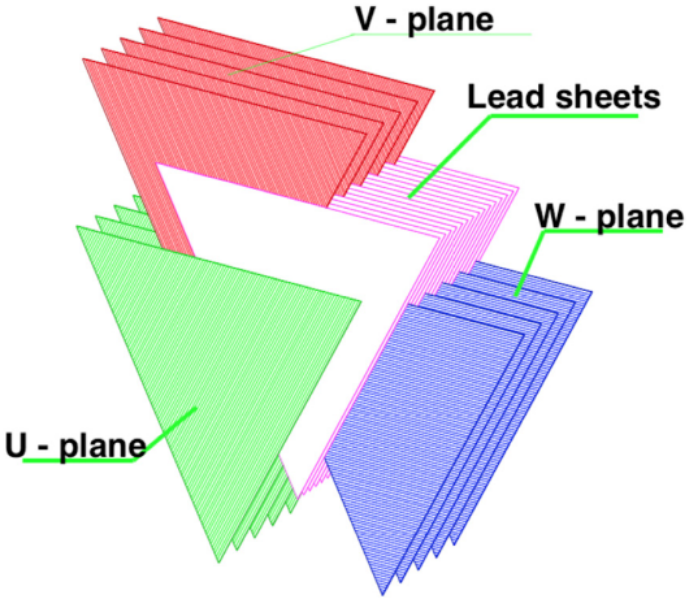

Fig. 2.15 Illustration of how the scintillating layers of the ECAL interleave between the lead sheets [53].

2.2.3 Central Detector

The Central Detector can detect particles at the largest polar angles, with a range of $35^\circ \leq \theta \leq 125^\circ$, as with the forward detector, there are different detectors working together for particle identification. The Central Vertex Tracker (CVT), made up of two micromegas and silicon microstrip sensors, is for momentum and vertex measurements of charged particles. The Central Time-of-Flight (CTOF) is a series of scintillator bars and finally, there is the Central Neutron Detector (CND), which is three layers of scintillator panels [53, 59].

CVT

The CVT consists of two detectors, the Silicon Vertex Tracker (SVT) and the Barrel Micromegas Tracker (BMT) [53]. The SVT covers a polar angle θ range of $35^\circ - 125^\circ$ and an azimuthal angle ϕ coverage of $\geq 90\%$ of 360°. The SVT is designed to measure the momentum of charged pions, kaons and baryons. As seen in Figure 2.16 is constructed of 3 regions, each with 10, 14 and 18 modules in order of radial distance from the beamline [63]. These modules have microstrip sensors mounted on each side; they get a position measurement, and similar to the DC, the inferred curved path of the particle through the layers due to the solenoid's magnetic field gives a momentum measurement.

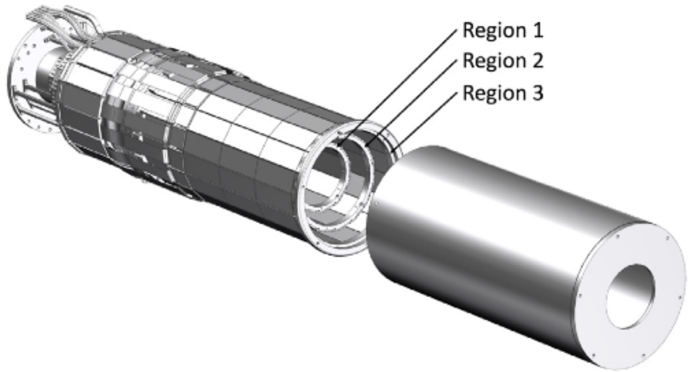

Fig. 2.16 Schematic of the SVT with the three radially layered regions labelled [63].

The BMT underlying detector operation is essentially the same as described in Section 2.2.1. However, the specific design is different here - seen in Figure 2.17 - the BMT is constructed of three regions covering about 120° of ϕ coverage [56]. It is located radially outwards from the SVT and improves the momentum resolution and tracking efficiency of the CVT.

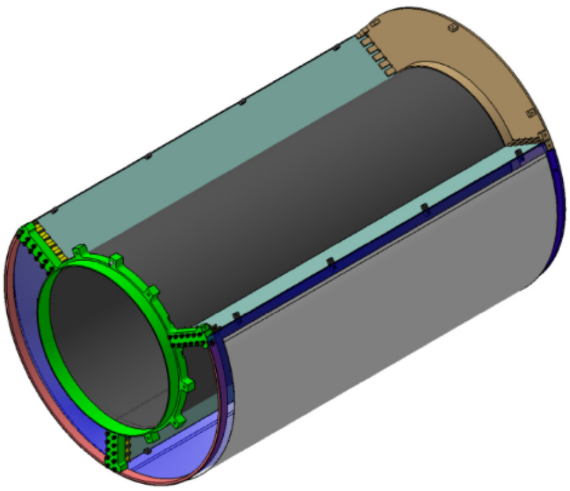

Fig. 2.17 Mechanical structure of the BMT with an open region [56].

CTOF

Serving the same role as the FTOF, the CTOF also utilises scintillators for the detection of charged particles, but it does have a very different design. There are 48 scintillator bars arranged into a cylinder; the design can be seen in Figure 2.18. This design gives the CTOF a full 360° of ϕ coverage, and it has polar coverage of $35^\circ \leq \theta \leq 125^\circ$ [59]. Each scintillator has a light guide on both ends, with a PMT on the end of them. This design achieves an average time resolution of 80 ps.

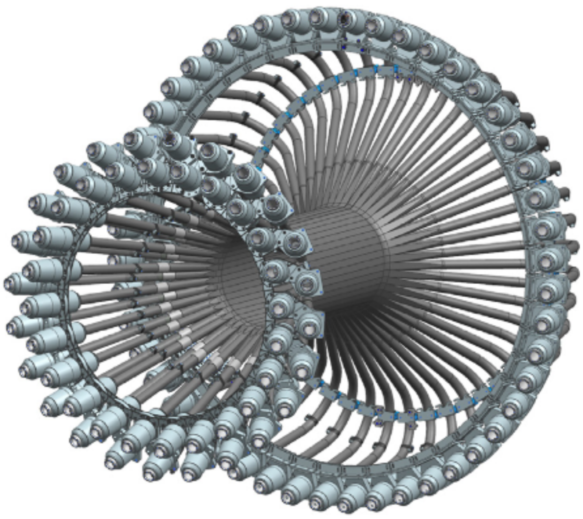

Fig. 2.18 Diagram of the 48 scintillator bars of the CTOF with the light guides and PMTs on each end. [59].

CND

The CND is also a barrel of scintillator bars but differs in design from the CTOF as it is required to detect neutrons. It has the full 360° of ϕ coverage, but it has lower θ coverage of $40^\circ \leq \theta \leq 120^\circ$. The CND has three layers of 48 scintillator bars. The layers give multiple position measurements and therefore, a path can be determined; using the path and time of flight, the CND can discern neutrons from photons. It is able to do this most effectively with neutrons that have momentum between 0.2 and 1.2 GeV and achieves a momentum resolution of $\frac{\sigma_p}{p}$ within 10%.

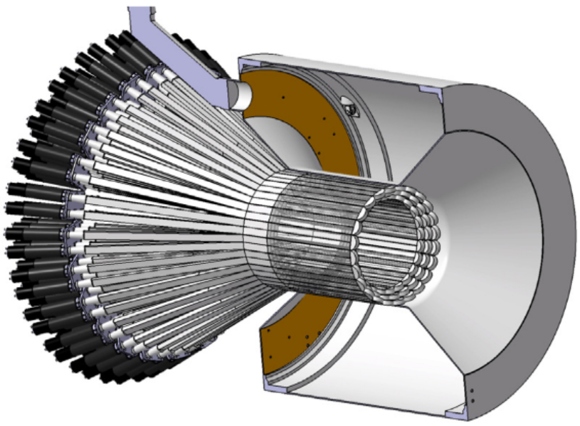

Fig. 2.19 Diagram of the CND with the three layers of 48 scintillator bars on display. Radially outward from the scintillator bars is the solenoid magnet [64].

Table 2.1 Summary of the angular ranges covered by all of the major detector systems, along with what they are used to determine and the resolution of the measurables or the threshold for particle discrimination.

Detector Region	**Detector System**	**Polar Range**	**Azimuthal Range**	**Measurable**	**Resolution**
CD	FT-Cal	$2^\circ < \theta < 5^\circ$	$0^\circ < \phi < 360^\circ$	$E_{e'}$ [GeV]	$\frac{\sigma_E}{E} \leq 2\%$
	FT-Track	$2.5^\circ < \theta < 4.5^\circ$	$0^\circ < \phi < 360^\circ$	x [μm] y [μm] $\theta_{e'}$ $\phi_{e'}$	≤ 150 [μm] ≤ 150 [μm] $\frac{\sigma_\theta}{\theta} \leq 1.5\%$ $\sigma_\phi \leq 2^\circ$
	FT-Hodo	$2.5^\circ < \theta < 4.5^\circ$	$0^\circ < \phi < 360^\circ$	e/γ discrimination	–
FD	DC	$5^\circ \leq \theta \leq 40^\circ$	$50\% - 90\%$ of $0^\circ < \phi < 360^\circ$	p [GeV]	$\frac{dp}{p} < 1\%$
	HTCC	$5^\circ \leq \theta \leq 35^\circ$	$0^\circ < \phi < 360^\circ$	$e/\pi^{+/-}$ discrimination	e threshold: 15 [MeV] π threshold: 4.9 [GeV]
	LTCC	$5^\circ \leq \theta \leq 30^\circ$	–	$\pi^{+/-}/K^{+/-}$ discrimination	π threshold: 3.7 [GeV] K threshold: 8.5 [GeV]
	RICH	$5^\circ \leq \theta \leq 26^\circ$	–	$\pi^{+/-}/K^{+/-}$ discrimination	π threshold: 3 [GeV] K threshold: 8 [GeV]
	FTOF	1b: $5^\circ \leq \theta \leq 35^\circ$ 1a: $5^\circ \leq \theta \leq 35^\circ$ 2: $35^\circ \leq \theta \leq 45^\circ$	$50\% - 95\%$ of $0^\circ < \phi < 360^\circ$	TOF [ns]	1b: 60-110 [ps] 1a: 90-180 [ps] 2: 170-180 [ps]
	ECAL	$5^\circ \leq \theta \leq 35^\circ$	$50\% - 85\%$ of $0^\circ < \phi < 360^\circ$	E [GeV] Position [cm] Time [ns]	$\frac{10\%}{\sqrt{E}}$ 0.5 [cm] 500 [ps]
CD	CVT	$35^\circ \leq \theta \leq 125^\circ$	$\geq 90\%$ of $0^\circ < \phi < 360^\circ$	p [GeV] θ ϕ	$\frac{\delta p}{p} \leq 5\%$ $\delta\theta \leq$10-20 [mrad] $\delta\phi \leq 5$ [mrad]
	CTOF	$35^\circ \leq \theta \leq 125^\circ$	$0^\circ < \phi < 360^\circ$	TOF [ns]	80 [ps]
	CND	$40^\circ \leq \theta \leq 125^\circ$	$0^\circ < \phi < 360^\circ$	n_p [GeV]	$\frac{\sigma_p}{p} \leq 10\%$

2.2.4 Superconducting Magnets

CLAS12 has two types of magnetic fields: a toroidal field and a solenoidal one. The torus magnet coils are in a six-sector configuration situated between the six sectors of the DC. The field it generates covers the polar angle range of 0° to about 35°. The solenoid magnet covers a more comprehensive polar range of approximately 35° to 125° and is situated radially outward from the CND [53]. Figure 2.20 summarizes the coverage of the magnetic fields. The design uses these two magnetic fields for one main reason: the fields allow for the high-resolution momentum measurements of charged particles. Achieving this through the toroidal field bending what would be the straight path of a charged particle towards or away from the beam line depending on the charge of the particle and polarity of the field. If the field polarity is set up to be negative, then this is the "inbending" data, meaning the negative particles are bent towards the beamline, and the opposite configuration is known as "outbending" data. The solenoidal field causes clockwise or anticlockwise spiralling depending on the charge of the particle; these two forms of bending of the particles' path of travel give a lot of tracking information to reconstruct the momentum of the particle. A benefit of the solenoid field is that it provides shielding from the low-energy electrons formed by Moller scattering, which are guided into a shielding pipe[65].

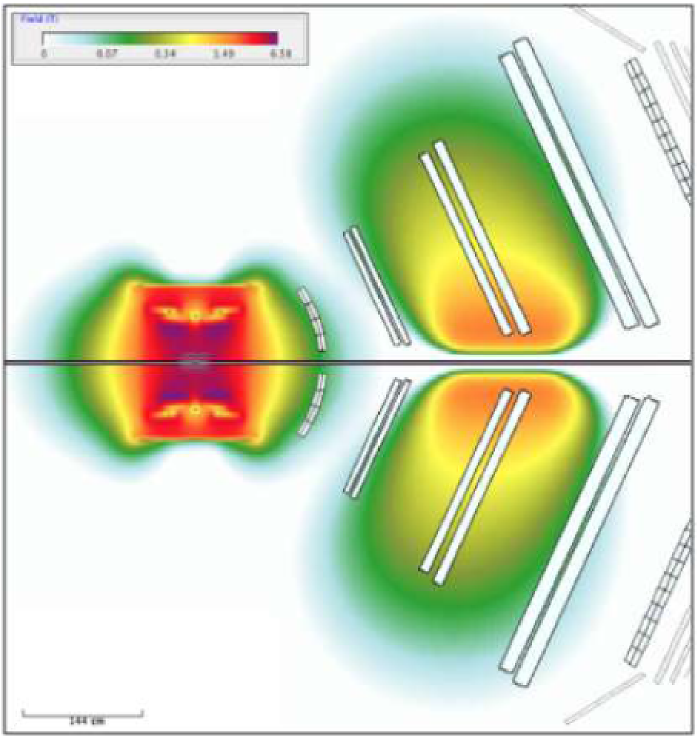

Fig. 2.20 Heat map of the field strength of the fields from both magnets in CLAS12. White boxes indicate detector components, and colour indicates field strength, purple being the peak field at 6.56 T [53, 65].

2.2.5 Data Acquisition

With an experiment like CLAS12, there is a large number of events produced, and at the planned luminosity of CLAS12 ($L = 10^{35}$ cm^{-2}s^{-1}), the hadron production rate is $\sim 5 \times 10^6$ every second, which would be too much to be recorded especially as a lot of this might be junk. In order to actually be recorded as an event, the event must set off various triggers. The generalised triggers are a combination of detecting the scattered electron in the FT or FD and then a positively charged track in the FD or CD [53]. The significant event reduction leads to a recorded event rate of $\sim 2 \times 10^4$ every second. This equates to a data production rate of 500 MB/s.

Triggers

The trigger system in CLAS12 works in three stages and has a total latency of 8 μs [66]. All trigger system information comes from two sources; if we are considering the PMT-based detectors, Flash Analog-to-Digital Converters (FADCs) are the information source and Drift Chamber Readout Boards (DCRBs) are the information source for the DCs, these are the pre-trigger boards. In the first stage, information comes from the pre-trigger boards and is passed on to the VXS Trigger Processor boards (VTPs). The FADCs are VXS format and work on a 250 MHz clock. The DCRBs are discriminator/TDC boards also of VXS format and operate on a 125 MHz. The detector systems used in the stage one trigger system are the FT-Cal, FT-Hodo, ECAL and the HTCC, these are mainly responsible for the electron trigger. Then, the FTOF, CTOF and CND are used for non-electron triggers like hadrons and photons, or muons in the case of the FTOF. In this first stage data banks are built with trigger decision detail.

The FTOF, CTOF, and CND systems also send information to the second stage of the trigger system every four nanoseconds; this second stage involves the calculation of timing and geometry coincidence between different subsets of the detectors in six groups; these groups correspond to the six sectors of the FD; the second stage of the trigger system also requires coincidence with information from the CD. In this second stage of the trigger, the data bank is built with sector-level and CD coincidence results.

Finally, the third stage collects all of the trigger bit streams into a single module. From this single module, the trigger bit streams can be combined in various ways to generate global trigger bits to read out the DAQ. Each global trigger bit contains two sector trigger bit conditions, which are both required to be true and one central trigger bit condition. In this third and final stage of the trigger builds the data bank that contains the trigger bit decisions for all final 32 trigger bit decisions.

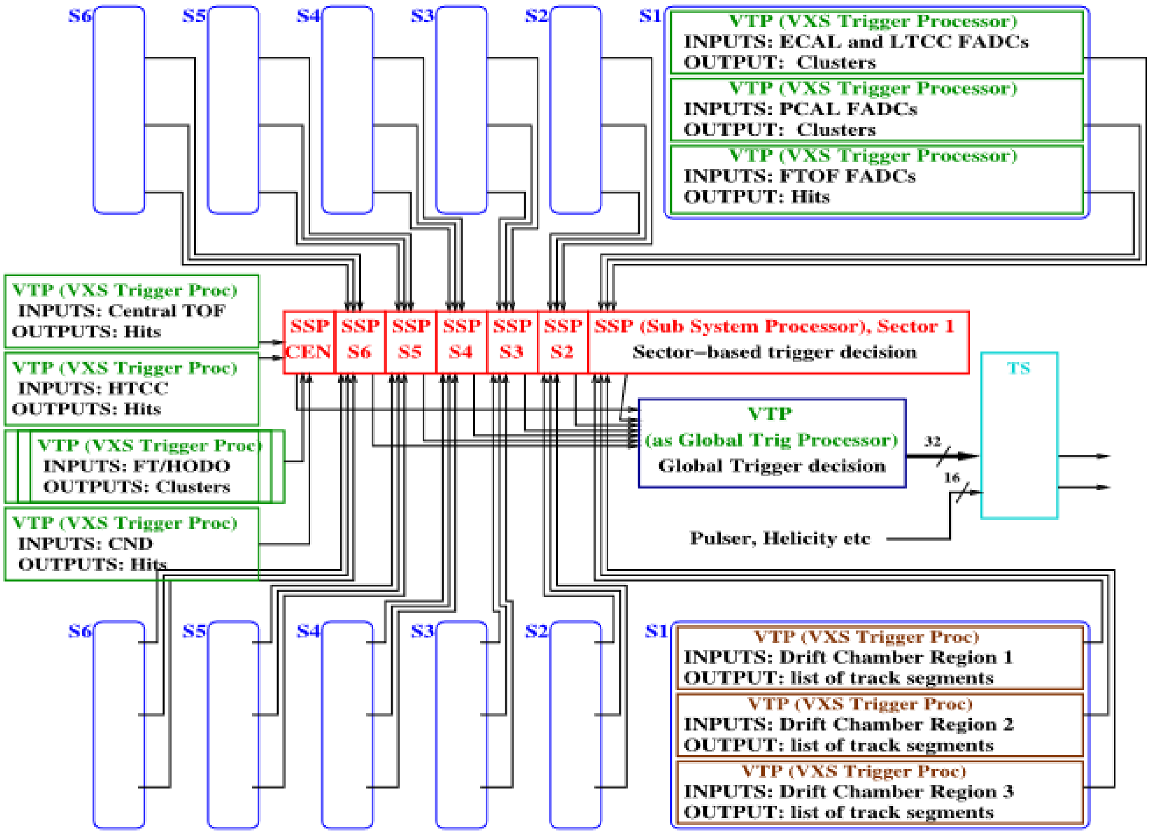

Fig. 2.21 The CLAS12 3 stage trigger system in diagram form [66].

Chapter 3

Search for the Singly Strange Hexaquark

This Chapter will describe the search for the singly strange hexaquark referred to as d_s. Looking at some approaches considered like the "bump hunt" and assessing why the search evolved into an analysis of polarization observables as well as putting all of this in the context of the previous work done in the efforts to find and study the $d^*(2380)$. This chapter will also provide a detailed discussion of polarization, how to extract it and how the Λ baryon is particularly useful in such a study with its self-analysing property. But before that, this chapter begins with a discussion of a theory study that the author aided in by carrying out simulations in order to determine an idea of what mass the d_s might have, and although that was not the larger goal of this paper (that was to study the properties of all hexaquarks) a study like this is the only serious way to start a search like the one presented in this thesis.

3.1 Properties of the d_s

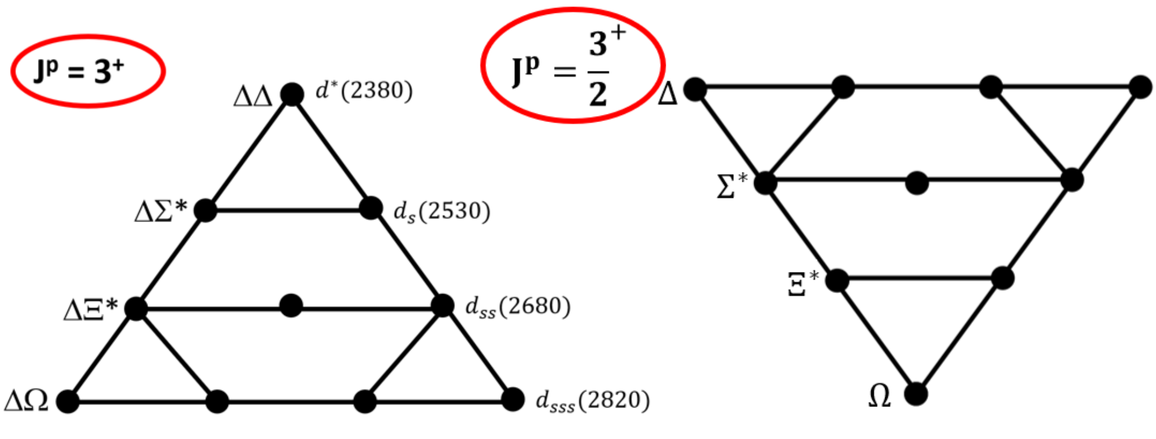

Fig. 3.1 On the left is the $J^p = 3^+$ anti-decuplet to which the hexaquarks of interest to this thesis belong. On the right is the decuplet of $J^p = \frac{3}{2}^+$ baryons, which holds the baryons that the hexaquarks on the left are resonances of.

As previously mentioned, two major structure models can describe the d_s hexaquark and other members of the $J^p = 3^+$ anti-decuplet. Either a molecule of two baryons that belong to the $J^p = \frac{3}{2}^+$ decuplet, both of these multiplets are shown in Figure 3.1. Or there is the genuine hexaquark model, where the particle has its six valence quarks in a single container. It is known that the structure model being considered affects the BE of the object and how this relates to both the mass of the constituent quarks and the mass of the hexaquark as a whole. The d_s (or any of the hexaquarks with the exception of the d^*) does not currently have a mass determined through experiment and therefore, to know what mass range to search in, one must be predicted. This was done through theory work that uses the following relations in this section to simulate the masses, widths and decay branches of all hexaquarks made of six "regular" quarks, this work is presented in this pre-published work [67] which is co-authored by the author. This predicted mass unsurprisingly relies on the chosen structure model. When it comes to the genuine hexaquark, an understanding of the concept of hyperfine splitting is needed and it can be summarised as the origin of the difference in mass between hadrons with the same valence quark content but different masses such as nucleons and Δ baryons. Those masses can be modelled with Equations 3.1 and 3.2.

$$M_N = 3M_q - \frac{K}{M_q^2} \tag{3.1}$$

$$M_\Delta = 3M_q + \frac{K}{M_q^2} \tag{3.2}$$

Where M_N is the mass of the nucleon, M_q is the mass of a dressed light quark (up or down) equal to 363 MeV, K is the parameter responsible for the hyperfine splitting, and M_Δ is the mass of the Δ. The hyperfine splitting component $\frac{K}{M_q^2}$ is equal to 50 MeV. As the source of this is essentially from quark-quark interactions, the six-quark environment of a hexaquark is more susceptible to its effect. Also, as the d_s has a strange valence quark, the dressed mass of it $M_s = 538$ MeV must be included to predict the mass of the d_s with Equation 3.3.

$$M_{d_s(Hex)} = 5M_q + M_s + \frac{10K}{M_q^2} + \frac{5K}{M_q M_s} - B_h \tag{3.3}$$

Where $M_{d_s(Hex)}$ is the predicted mass of the d_s when modelled as a genuine hexaquark, $\frac{5K}{M_q M_s}$ is a term added to account for the interaction between the light quarks and the strange quark and $B_h \sim 550$ MeV is a binding term to correct the predicted mass of the d^* to the value from experiment. This mass is calculated to be 2474 MeV. Now consider the molecular model of the hexaquarks. This model has no terms for hyperfine splitting and only considers the coupling between the two Δ baryons via pion exchange. This model predicts a mass for the d_s given by Equation 3.4.

$$M_{d_s(Mol)} = M_{red}(\Delta\Sigma^*)(3f \cdot 2f)^2 \tag{3.4}$$

Where $M_{d_s(Mol)}$ is the predicted mass of the d_s assuming a molecule structure, M_{red} is the reduced mass of the constituent Δ and Σ^* defined as $\frac{M_\Delta M_{\Sigma^*}}{M_\Delta + M_{\Sigma^*}}$ and f is an effective meson baryon coupling constant fixed to a value which reproduces the experimental mass of the d^*. The mass for the molecular picture is calculated to be 2578 MeV.

As well as a theoretical mass, a width is needed to search for the d_s. This gives a range to the masses calculated and therefore bounds the search for the d_s to lower and upper bounds. Calculating the width of a particle requires one to sum the partial widths, which are related to specific decay branches of the particle. A particle's total width is also related to the decay time via the relation seen in Equation 3.5, and the partial width can be calculated from that with Equation 3.6.

$$\Gamma = \frac{\hbar}{\tau} \tag{3.5}$$

$$\Gamma_{partial} = BR \times \Gamma \tag{3.6}$$

Where Γ is the total width of the particle, $\hbar$ is the reduced Planks constant, τ is the lifetime of the particle, $\Gamma_{partial}$ is the width specific to a particular decay channel, and BR is the branching ratio, the probability that the particle will decay via a specific decay branch. The partial width for all the possible decay branches for the d_s (as well as all the other "regular" quark hexaquarks) was calculated. This was done by simulating all of the decays of the hexaquarks, which calculates the width as a function of BE and using the above-described mass models, the partial widths can be extracted.

The general model for the width is different not only for the structure model assumed but also for the category of decay channel. Whether it is octet-octet decay (8$\oplus$8), where the d_s decays into two $J^p = \frac{1}{2}^+$ octet baryons, or decuplet-decuplet decay (10$\oplus$10), where it decays into two $J^p = \frac{3}{2}^+$ decuplet baryons. We start with the width calculation for the 8$\oplus$8 decays assuming a genuine hexaquark, given by Equation 3.7, as this is the simplest model.

$$\Gamma_{8_{hex}} = g_8^2 p^5 F_8(p) \tag{3.7}$$

Where g_8 is a coupling constant extracted from the measured partial width of the $d^* \to pn$ decay, which is measured to be 8 MeV [68], p is the momentum of one of the baryons in the hexaquark rest frame, and $F_8(p)$ is the form factor defined by Equation 3.8.

$$F_8(p) = \frac{R^4}{1 + R^4 p^4} \tag{3.8}$$

Where R is a constant equal to 6.3 GeV^{-1} [69].

We then continue with the 8$\oplus$8 decays but switching to the molecular hexaquark picture. In this case, the width is calculated by modifying Equation 3.7 by multiplying it by a factor to account for the overlap of the two baryon wavefunctions, giving the width in this case with Equation 3.9.

$$\Gamma_{8_{mol}} = \tilde{g}_8^2 p^5 F_8(p) P(B) \tag{3.9}$$

Where $\tilde{g}_8^2$ is the coupling constant modified so the calculation still returns 8 MeV for the d^* case, and $P(B)$ is the probability of wavefunction overlap as a function of BE. This is extracted from simulations under the assumption that the baryons are spherical with a distribution similar to the charge distribution of the proton: $\rho(r) = exp(-\alpha r)$, where α is 4.27 fm^{-1} and r is defined by Equation 3.10 and is the distance between the centres of these spherical distributions.

$$r = \frac{1}{\sqrt{2M_{red}|B|}} \tag{3.10}$$

Where symbols have their previous definitions.
Now, to describe the procedure for 10⊕10 decays starting with the assumed genuine hexaquark structure. This is more complex than its 8⊕8 counterpart as the decuplet baryons have a sizeable width themselves. The width for this case is calculated using Equation 3.11, which contains information concerning both baryons.

$$\Gamma_{10_{hex}} = \gamma_{10} \int dm_1^2 dm_2^2 F^2(q_{10}) |D_{D_1}(m_1^2) D_{D_2}(m_2^2)|^2 \tag{3.11}$$

Where γ_{10} is a normalisation factor used to reproduce the width at zero BE to be the sum of the widths of the two decuplet baryons, m_1 and m_2 are the masses of the baryons, $F^2(q_{10})$ is the form factor as a function of the momentum of one of the baryons in the hexaquark rest frame given by Eqaution 3.12 and $D_{D_{1/2}}(m_{1/2}^2)$ are propagators for the decuplet of baryons given by Equation 3.13.

$$F(q_{10}) = \frac{\Lambda^2}{\Lambda^2 + \frac{q_{10}^2}{4}} \tag{3.12}$$

$$D_{D_{1/2}} = \frac{\sqrt{\frac{m_{1/2}\Gamma_{1/2}(q_M)}{q_M}}}{M_{BM}^2 - m_{1/2}^2 + i m_{1/2} \Gamma_{1/2}^{tot}} \tag{3.13}$$

Where Λ the cut-off parameter is equal to 0.16 GeV from [69] and confirmed by the simulations, q_{10}^2 is the momentum of one of the decuplet baryons in the hexaquark rest frame, M_{BM} is the invariant mass of the octet baryon and octet meson that the decuplet baryon decayed into (see Section 5.1 for a definition of invariant mass), $\Gamma_{1/2}(q_M)$ is the energy dependant width of the baryon given by Equation 3.14, the energy dependence coming from the momentum of the meson from the decuplet baryon decay, i is the imaginary unit $\sqrt{-1}$ and $\Gamma_{1/2}^{tot}$ is the total width of the decuplet baryon.

$$\Gamma_{1/2} = \gamma q_M^3 \frac{R^2}{1 + R^2 q_M^2} \tag{3.14}$$

Where γ is 0.74 for Δ and 0.28 for the Σ^*, these were set to scale the function to the nominal partial widths.

Finally, we consider the width calculations for the 10$\oplus$10 for a molecular hexaquark. This actually follows the same procedure as the pure hexaquark counterpart, but due to the mass and, therefore, the BE being different, this leads to a different width calculation.

Table 3.1 Summary of all of the partial widths and branching ratios for the three generalised decay branches of the d_s. These values are seen for both main structure models.

	Genuine Hexaquark $d_s(2474)$		Molecule $d_s(2578)$	
Decay Branch	$\Gamma_{partial}$ [MeV]	BR [%]	$\Gamma_{partial}$ [MeV]	BR [%]
$\Delta\Sigma^*$	3.1	29	82.9	91
$N\Lambda$	3.9	37	4.2	5
$N\Sigma$	3.6	34	3.9	4
	Total Γ: 10.6		Total Γ: 91.0	

The widths, branching ratios and masses of the d_s are summarised in Table 3.1; it is split by the structure model, and then those are further broken down by the decay channel. When it comes to the molecular model, it is heavily favoured towards the $d_s \to \Delta\Sigma^*$ decay branch. But when considering a genuine hexaquark, the branching ratios are much closer to equal. However, the $d_s \to N\Lambda$ has the highest branching ratio, which is the first point in the reasons that this was the chosen decay branch to study. Further reasoning is given in the rest of this chapter. Before that, though, a summary of the evidence for the $d^*(2380)$ is provided to better contextualise the search for evidence of the d_s.

3.2 Evidence for the $d^*(2380)$

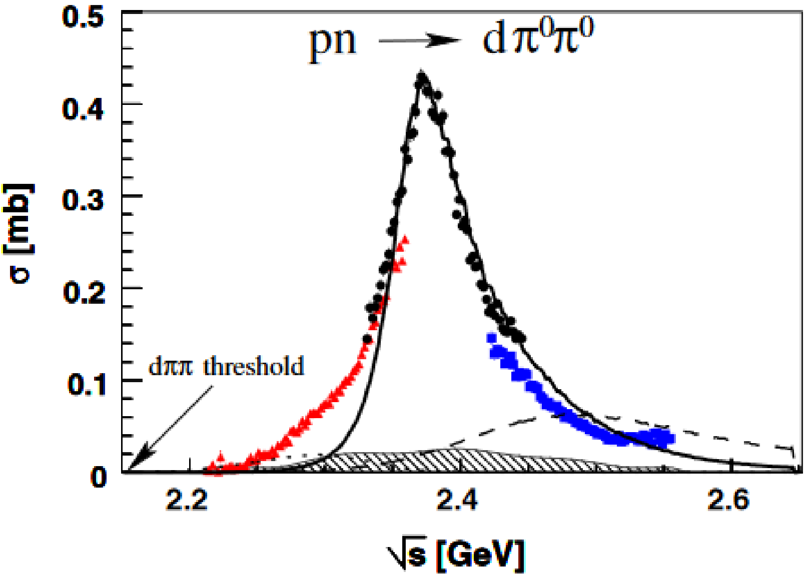

Fig. 3.2 Total cross-section vs $\sqrt{s}$ for the $pn \to d\pi^0\pi^0$ reaction. The red triangles are data from the 1.0 GeV beam, the black circles are data from the 1.2 GeV beam and the blue squares are the data from the 1.4 GeV beam.

The first experimental evidence for the $d^*(2380)$ comes from WASA-at-COSY collaboration in 2011 [42] through analysis of the first reaction of the three in Equation 3.15. This experiment had a proton beam of three different energies: 1.0 GeV, 1.2 GeV and 1.4 GeV, impinging on a deuteron target. Here, the main finding shown in Figure 3.2 was a peak in the cross-section at an approximate mass of 2.37 GeV and a width of about 70 MeV.

$$\begin{aligned} &pn \to d\pi^0\pi^0 \\ &pn \to d\pi^+\pi^- \\ &pn \to NN\pi\pi \end{aligned} \tag{3.15}$$

A similar peak in the cross-section is seen when the second reaction in Equation 3.15 is analysed [43]. Then, there are multiple studies of the reactions of the type described by the bottom reaction in Equation 3.15 [70, 44, 71]. All of these examples of measurements of the $d^*(2380)$ are essentially bump hunts due to the cross-section being proportional to the acceptance corrected yield, and the studies were searching for peaks in this at particular energies. Even though all these analyses show the $d^*(2380)$ clearly, other methods can and should be utilised when gathering evidence for a new hadron like this.

Other studies addressed this by looking for signs of the $d^*(2380)$ in polarization observables. Like the measurement of the analysing power of the neutron in the $d^* \to pn$ decay channel [45] made in an experiment involving a 2.27 GeV deuteron beam incident on a hydrogen (proton) target making a proton-neutron scattering reaction. The result, which is shown in Figure 3.8, is a narrow peak in the analysing power at the correct mass and with the width of the $d^*(2380)$. Measurements of this type allow for partial wave analysis, allowing for more substantial evidence and deeper analysis of the resonance. Now, a look at options to search for evidence of the d_s can be done.

3.3 Bump Hunt

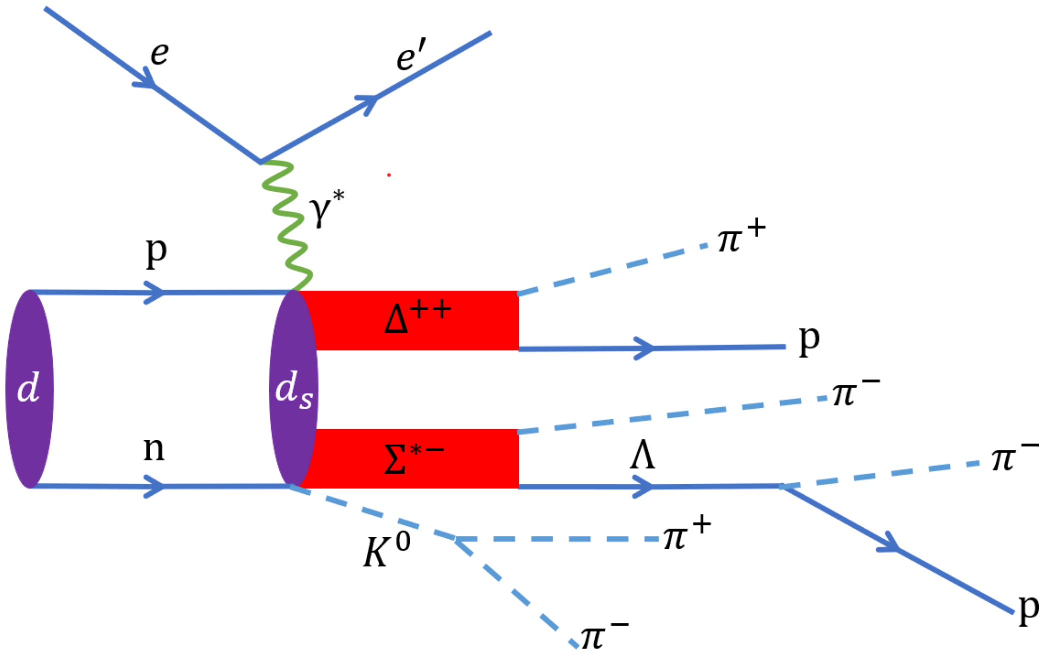

Fig. 3.3 Feynman diagram of the $d_s \to \Delta^{++}\Sigma^{*-}$ channel. This was the channel used in the bump hunt.

The beginning of the search for the d_s explored one of the $10 \oplus 10$ decay channels because of the very large branching ratio of this decay type (91%) when considering a molecular structure of the hexaquark. When producing the d_s at CLAS12 (electroproduction off a deuteron target), a kaon must be produced to conserve strangeness, specifically a K^+ or K^0. Due to the high amount of background channels originating from reactions with in-flight K^+ production, the focus was on K^0 channels. The one chosen was the one depicted in Figure 3.3; the choice of this one specifically is due to a few reasons. Along with the K^0 production, the requirement for two protons cuts out a large amount of background by itself. Finally, there is a large multiplicity of end-state particles, paired with the fact that there are several invariant and missing masses to check and cross-check, which makes for a very pure channel to analyse. The result of this "bump hunt" style of search in this particular case would be a peak above a smooth background seen in the invariant and or missing mass (see Section 5.1) of what would correspond to the d_s mass.

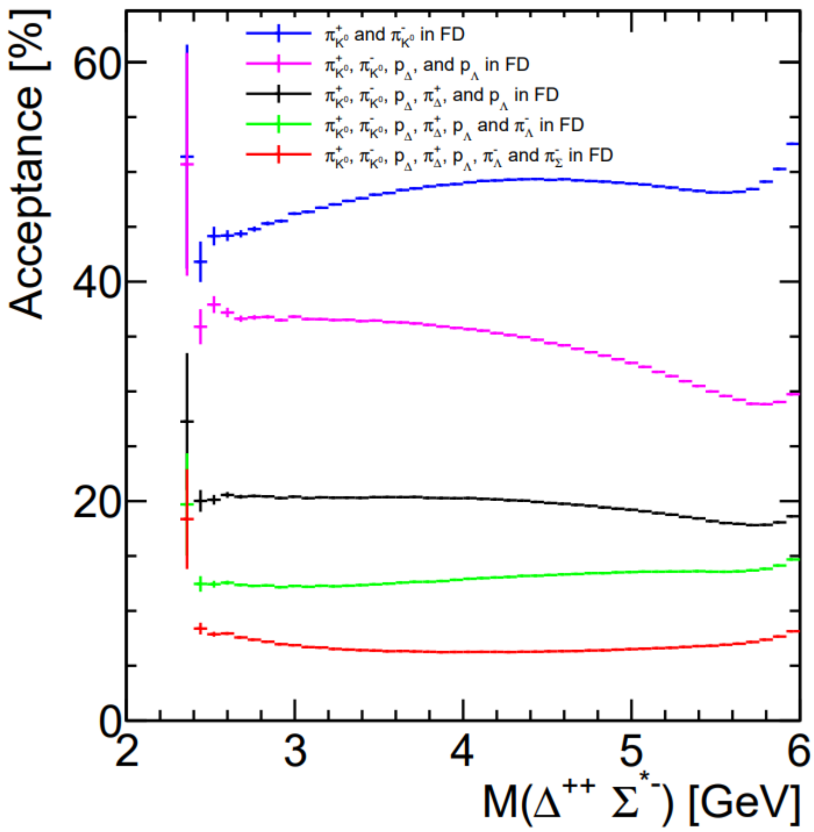

Fig. 3.4 Acceptance vs Invariant mass of the Δ^{++} and Σ^{*-} extracted from a phase-space based event generator that uses a $1/q^2$ weight. The different coloured points differ by having more of the final state particles with restrictions of θ that align with the θ range of the FD, specifically $5^\circ \leq \theta \leq 40^\circ$. The blue points are data where this cut is on the π^+ and π^- from the K^0 decay. The pink points add the two protons to the FD particles. The black points are where the decay products of the K^0 and Δ^{++}, along with the proton from the Λ decay, all pass through the FD. The green points are where the decay products of the K^0, Δ^{++} and Λ are detected in the FD. Finally, the red points have all the final state hadrons in the FD.

Although the high multiplicity of the channel described is good for purity, this leads to low acceptance (see Section 3.5). This is well illustrated in Figure 3.4, and the red points are the relevant ones as this bump hunt used events that required all the final state particles to be detected in the FD. However, this shows acceptance from a reasonably basic event generator (see Section 3.5), and the reality is likely a lower acceptance due to the physical gaps in the detector and possible issues in particle detection and reconstruction.

There was a thought of performing the same search on an 8⊕8 decay. To see why this cannot be done, one must look at the $\gamma d \to d^* \to pn$ channel [48]. It is known that the cross-section of this is on the order of one hundred times smaller than that of the photodisintegration ($\gamma d \to pn$) reaction, hence why polarization observables were used for the analysis of that channel. When considering the added cross-section reduction due to the production of a strange particle is clear why a bump hunt is not the correct analysis route.

3.4 Polarization

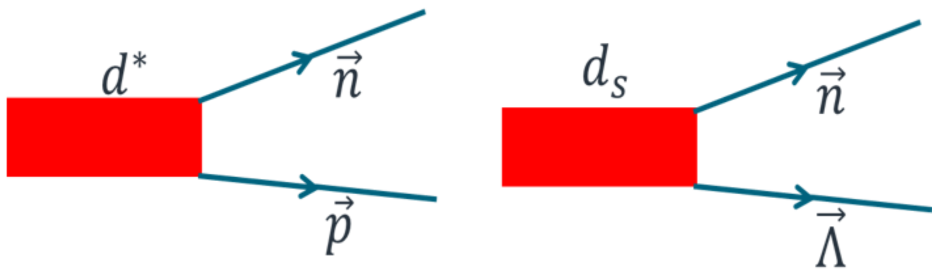

Fig. 3.5 Two simplified Feynman diagrams. On the left, the $d^* \to pn$ decay and on the right, the $d_s \to \Lambda n$, the similarities of the two channels can be seen.

Due to the extremely low cross-section for the production of the d_s, other measurables were needed to look for experimental evidence of the excited state. The chosen measurable is the polarization of the decay baryons from the $8 \oplus 8$ branches where the d_s decays into either the Σ or Λ along with a nucleon N, which are all members of the $J^p = \frac{1}{2}^+$ octet. This is the selected observable due to two main things. Firstly, from theory, it is known that as this is a strong interaction, everything must be conserved, including parity. The d_s has $J^p = 3^+$ and the daughter baryons have $J^p = \frac{1}{2}^+$. Therefore, the most optimal configuration for the conservation of angular momentum and parity is for the spins of the baryons to be aligned and the angular momentum between them to be even, the lowest being $L = 2$ aligned with the spin of the baryons from that one can ascertain that the baryons should be maximally polarised. Secondly, there is previous experimental data of the $d^* \to pn$ channel having the same sensitivity to polarization. In that case, the polarization had to be measured with the use of a polarimeter to measure the neutron polarization. The choice of this observable leads to the selection of the $d_s \to \Lambda n$ channel because, unlike with the neutron, the Λ is self-analysing.

3.4.1 Asymmetry in the Λ Weak Decay

The decay of the $\Lambda \to p\pi^-$ is governed by the weak interaction, and in this decay, there is interference between the parity-conserving and parity-violating partial waves. As Λ and the proton belong to the same $J^p = \frac{1}{2}^+$ octet of baryons and the π^- is a $J^p = 0^-$ meson, parity is violated when angular momentum between the two daughters L is zero which is the s partial wave. The suppressed $L = 1$ is a p partial wave decay branch and conserves parity. This mixing of amplitudes leads to an asymmetry that gives a preferred direction to decay particles relative to the direction of the spin of the Λ.

3.4.2 Extraction of the Λ Polarisation

This asymmetry leads to this self-analysing feature of the Λ, meaning the polarization of the Λ can be extracted directly by measuring the angular distribution of the decay products. To understand how this can extract polarization, one must first look at the kinematics of an electroproduction reaction. From that, one can define the axes used to measure the angular distributions.

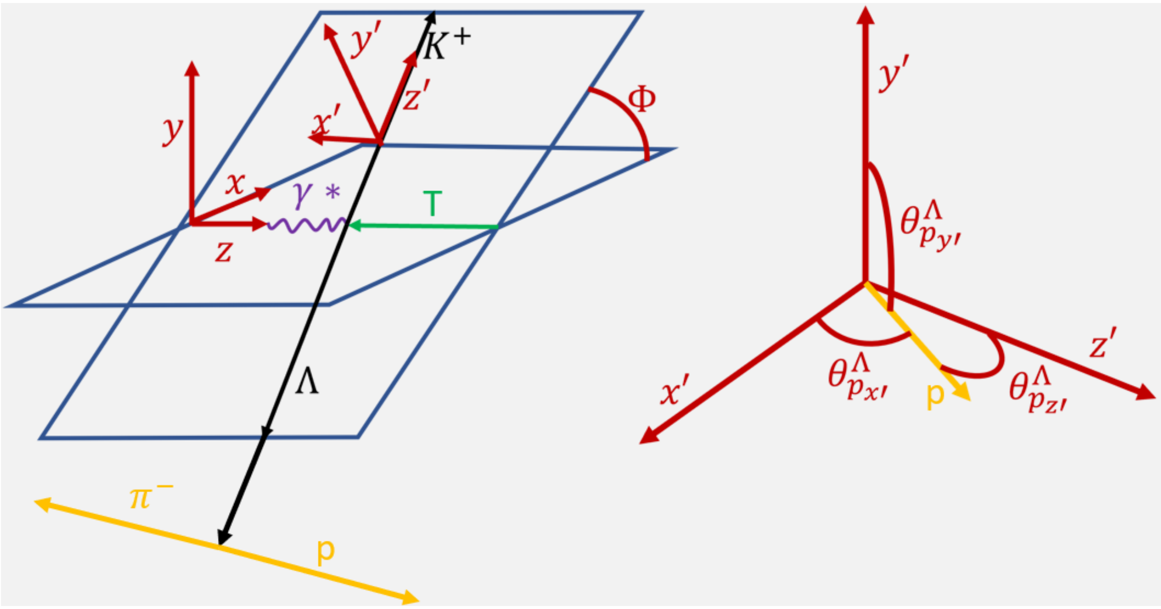

Fig. 3.6 On the left, the general electroproduction reaction is shown diagrammatically. The reaction is shown with the electron scattering plane, with the target (T) and the virtual photon (γ^*), and the hadron reaction plane with the Λ and K^+, angle ϕ is the rotational offset between these two planes (first introduced in Section 1.3). Also shown on the left are the decay products of the Λ boosted to its rest frame. On the Right are the three primed axes and the proton boosted to the Λ rest frame between these axes, giving an example of how the angles are measured.

With electroproduction, the electron scatters off the target, exchanging momentum with it via a virtual photon seen in the scattering plane. You then have a resonance formed that decays into a baryon and meson, as seen in the hadron reaction plane. It can be shown by Figure 5.1 how the axes used to measure the protons' angular distribution relate to the scattering plane and the hadron reaction plane. The axes are defined in the following way z' is the momentum of the K^+ in the Center of Mass (CM) frame. Then y' is the cross product of the virtual photon and the K^+ both in the CM frame. Finally, x' is defined like any set of Cartesian coordinates where $x' = y' \times z'$.

$$z' = P^{CM}_{K^+} \tag{3.16}$$

$$y' = P^{CM}_{\gamma^*} \times P^{CM}_{K^+} \tag{3.17}$$

$$x' = (P_{\gamma^*}^{CM} \times P_{K^+}^{CM}) \times P_{K^+}^{CM} \tag{3.18}$$

To understand how one extracts polarization from the various angles measured, an assessment of Equation 3.19 is needed.

$$N(\cos\theta_{p_A}^{\Lambda}) = \frac{N_0}{2}(1 + P_A \alpha \cos\theta_{p_A}^{\Lambda}) \tag{3.19}$$

Where N is the acceptance corrected yield for a particular $\cos\theta_{p_A}^{\Lambda}$, where $\theta_{p_A}^{\Lambda}$ is the polar angle of the proton in the rest frame of the Λ with respect to the chosen axis $A = x', y'$ or z' (boosted to the Λ rest frame). N_0 is defined as the total acceptance corrected yield for the data set being analysed. α is the weak decay parameter equal to 0.748 ± 0.007 [72] and P_A is the polarization again relative to the chosen axis. Taking the above as a linear equation of form $y = mx + c$, the gradient is defined as the following.

$$m = \frac{N_0 P_A \alpha}{2} \tag{3.20}$$

This part of the procedure is illustrated well in Figure 3.7 where one of the $\cos\theta_{p_{y'}}^{\Lambda}$ distributions are plotted and fit with a first-order polynomial to extract m. Finally, rearranging to get the polarisation component gives the following.

$$P_A = \frac{2m}{N_0 \alpha} \tag{3.21}$$

To fully summarise, the method used to extract the polarisation of Λ when it decays to $p\pi^-$ is as follows. Take the proton from the Λ decay, boost it to the Λ rest frame, and measure the angle between this new proton vector and the axis of importance. Take the cosine of that angle and plot it in a histogram of a number of bins (chosen for this work was six bins). Finally, fit this histogram with a first-order polynomial and extract the gradient to be used in Equation 3.21 to calculate the corresponding polarisation component.

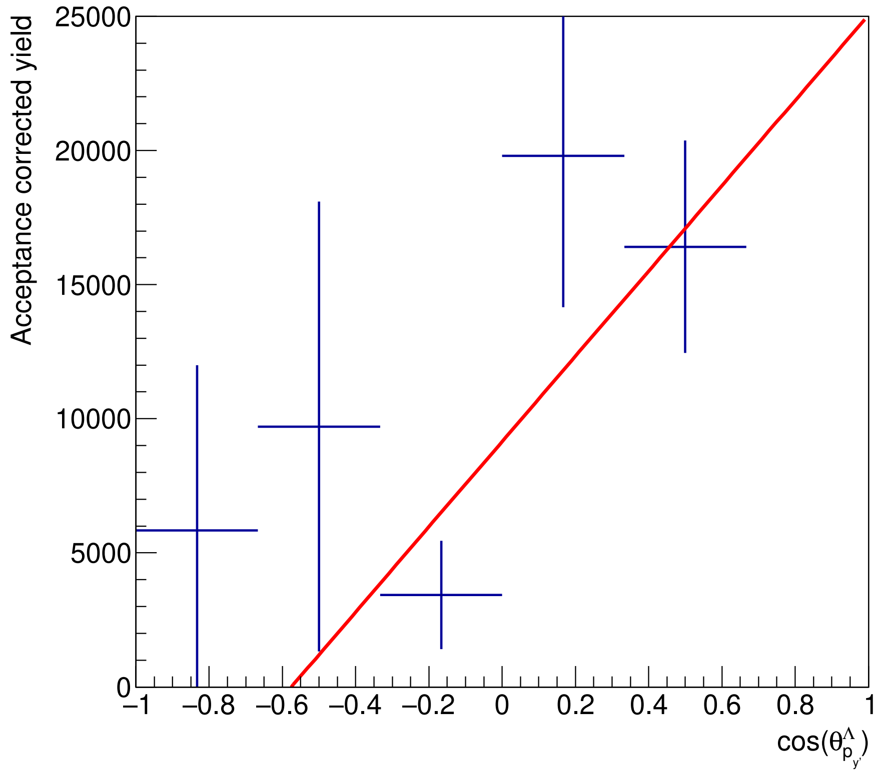

Fig. 3.7 Plot of six bins of $\cos\theta^{\Lambda}_{p_{y'}}$ for a particular missing mass bin. Used as an example of the gradient extracted to calculate the polarization.

3.5 Acceptance Corrections

Strictly speaking, what is described here are acceptance and efficiency corrections coupled together but will be referred to from here on out as acceptance corrections. Acceptance corrections are needed to account for the fact that not every event that actually occurred will be successfully detected and reconstructed. These events can be missed due to physical gaps in the detector, having particles undetected or failures in the reconstruction procedure, but unlike the philosophical tree falling in the empty forest, we can and must account for it. The way this is done is relatively simple, starting with the generation of a known number of events (n_{MC}); those events get passed through a virtual version of CLAS12, which is modelled using software that uses Geant4 to replicate the efficiency and acceptance of the real CLAS12 accurately. That data gets processed by the standard analysis macros used on the real data, giving a number of simulated reconstructed events (n_{sim}). The acceptance correction (A_{cor}) is a ratio of these two numbers, and finally, to get the acceptance corrected yield, the number of reconstructed events (n_{exp}) is divided by A_{cor}.

$$N = \frac{n_{exp}}{A_{cor}} = \frac{n_{exp} n_{MC}}{n_{sim}} \tag{3.22}$$

For N, this has to be done on a bin-by-bin basis because of the angular dependence of the acceptance of CLAS12. This was achieved by plotting the cosines of the angles in a histogram and dividing and multiplying the histograms together.

3.5.1 Simulations

The first step in producing the acceptance corrections is using a relatively simple event generator to produce the aforementioned generated events. It is a phase-space based event generator. This means it takes the available energy and momentum from the specifications of the target and beam given to it by the user and generates the intermediate and final state particles (also user-specified) with statistically distributed fractions of that total energy and momentum. It does handle secondary decays, for example, a $\Lambda \to p\pi^-$, but again, this deals out the previously calculated Λ momentum and energy to the daughter particles. Something this event generator cannot do is account for detached vertices. This is where an intermediate state particle survives long enough to move a not negligible distance from the initial interaction vertex. This is not detrimental to this work, as this detached vertices concept is not included in the data calibration used in this research (pass 1).
The next stage, past event generation, is processing these events through a virtual CLAS12. This is done using GEMC [73], the CLAS12 simulation software framework, written in C++, that utilises Geant4 to make this virtual CLAS12 environment. This second stage of the acceptance correction procedure is done using the Open Science Grid (OSG). It handles the complex computation of these generated events being processed by the virtual CLAS12.

3.6 The Final Search Method

It was mentioned in Section 3.4 how the $d_s \to \Lambda n$ is analogous to the $d^* \to pn$ channel; this is illustrated by Figure 3.5. It was also stated in that section that both channels are sensitive to polarization both from theory and the data presented in this reference [51]. The ideal scenario for the $P_{y'}$ result would be similar to the one shown in Figure 3.8. A plot of the y component of the analysing power of the neutron from the $d^*(2380)$ decay against the CM invariant mass, it peaks at the $d^*(2380)$ mass. The ideal result would be the $P_{y'}$ versus the missing mass of what should be the d_s, defined as $M^2_{d_s} = (P_e + P_d - P_{e'} - P_{K^+})^2$ (see Section 5.1 for a full description), with a peak in polarization indicating the mass of the d_s and the width of this peak would give insight into the hexaquarks width. A notable point concerning the data presented in Figure 3.8 is its constriction to a particular polar angle of the neutron in the CM or d^* rest frame relative to the unboosted d^* momentum (θ_n^{CM}) this angle is 83°.

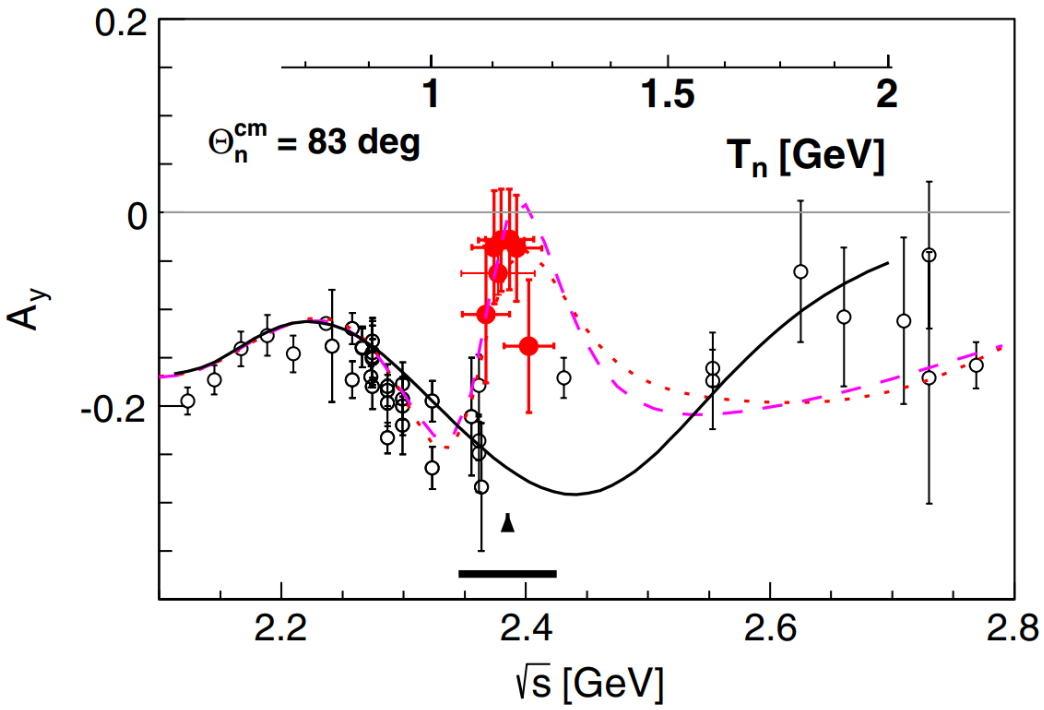

Fig. 3.8 Analysing power of a neutron from d^* decay plotted against the CM energy (at θ_n^{CM} which in this data is the same as the invariant mass of the d^*. The red solid points are data from the reference [51]. The hollow points are from previous works. The solid black line is the SAID SP07 phase shift prediction. The dashed pink line is the weighted SAID partial-wave solution, and the dotted red line is the unweighted counterpart.

3.6.1 Kinematic Based Sensitivity of Polarization

The reason for this angle cut can be explained with the aid of Figure 3.9. From theoretical work done [74] it is known that the sensitivity to polarization for these resonances is proportional to this associated Legendre polynomial P_j^1 where j is the angular momentum, which in the case of hexaquarks is 3 so the polynomial in question is P_3^1; it can be represented with Equation 3.23 and re-written with $x = \cos(\theta)$ to get Equation 3.24.

$$-\frac{3}{2}(5x^2-1)\sqrt{1-x^2} \tag{3.23}$$

$$-\frac{3}{2}(5\cos^2(\theta)-1)\sqrt{1-\cos^2(\theta)} \tag{3.24}$$

Then, from this and seeing that the large central peak in Figure 3.9 is at $x = 0$ and knowing $\cos(90°) = 0$, it is clear why the search for the d^* signal was performed with a cut on θ_n^{CM} at about 90°.

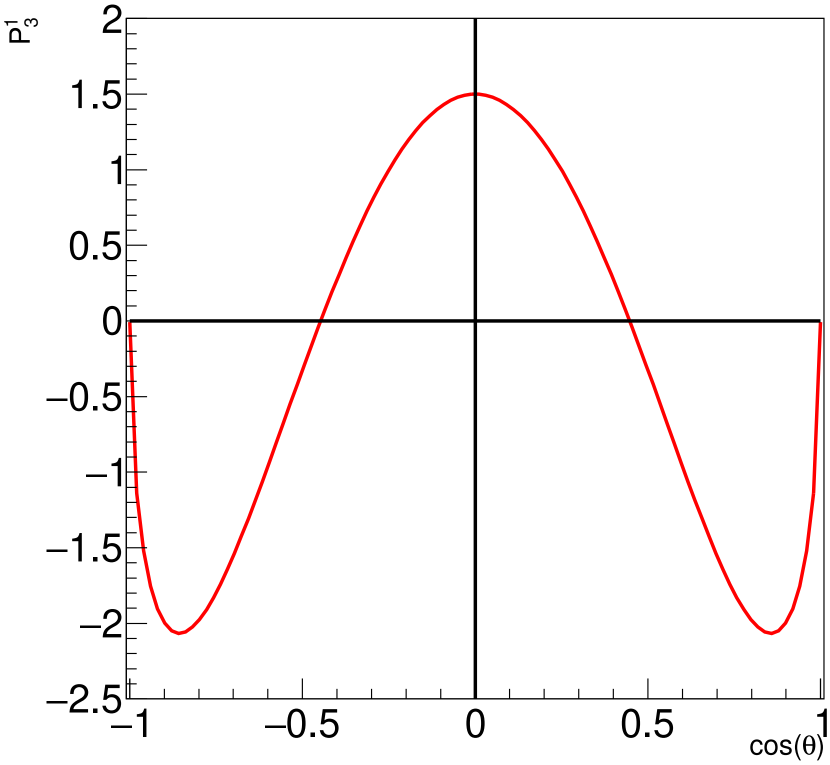

Fig. 3.9 Plot of the P_3^1 associated Legendre polynomial described by Equation 3.23.

The equivalent angle that the polarization observables extracted in this research are reliant on is $\theta_\Lambda^{d_s}$; this is the angle between the Λ in d_s rest frame and the unboosted d_s momentum. These angles are defined by the diagrams in Figure 3.10.

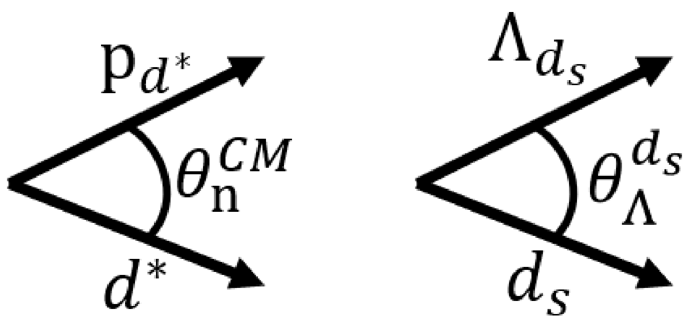

Fig. 3.10 Diagrammatic definitions of $\theta_n^{d^*}$ used for the analysis of the d^* and $\theta_\Lambda^{d_s}$ which will be used in the search for evidence of the d_s.

3.7 Summary

This chapter provided a layout of how to search for the d_s^0 both in terms of the theoretical prediction of masses and widths of the resonance and a full description of search methods. These search methods have also been given a prediction in efficacy predicted from theory and previous studies. It is now appropriate to discuss the data and how it was processed from a raw form to a usable format for analysis.

Chapter 4

Data Handling and Reconstruction

In this chapter, an overview of the run groups analysed in this thesis will be provided, along with a description of the differences between the run groups. This is followed by a summary of the path from raw data collected by CLAS12 and processed by the "cooking" process into data that can analysed. The author wrote the event selection code, and its main function is outlined in this chapter. This outline covers what software is used, the data storage file chosen, and requirements and cuts implemented for event selection.

4.1 Run Groups

Experiments in Hall B are assigned to a "Run Group", enabling physics measurements requiring similar experimental configurations (beam energy, target substance, beam and/or target polarization, etc.) to be grouped together into the same beam time. This work analyses data produced by two run groups. Run Group A (RGA) and Run Group B (RGB). Differentiating only by what target and what specific triggers are used. The CLAS12 trigger system is covered in Chapter 2, Section 2.2.5 but seen in Figure 4.1 is what is shown to a CLAS12 shift taker providing the relevant information for active triggers. This image also shows the list of the 32 trigger bits used in the CLAS12 trigger system. Although the beam energy is not the same in each run as intended, operational limitations of CEBAF prevented this.

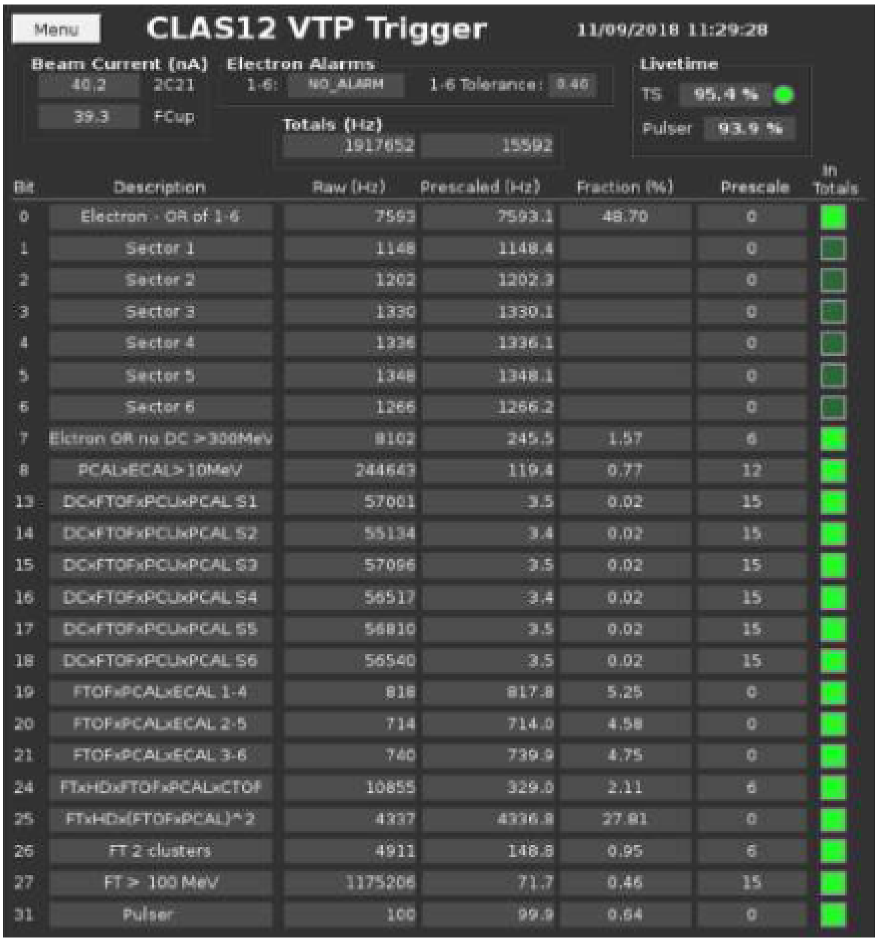

Fig. 4.1 CLAS12 trigger control seen by a CLAS12 shift taker for a specific experimental run.

RGA

The target for RGA is liquid hydrogen, contained in a cylindrical target cell that has an approximate 2.5 cm diameter and a length of 5 cm. This hydrogen target means RGA is for studying electron-proton scattering events and, in this thesis, is used for comparison to the RGB data. The electron beam energy for all RGA events that were analysed for this thesis was 10.6 GeV. The run periods used in this work are the outbending and inbending runs from the Fall of 2018 run period and the inbending runs from the Spring 2019 run period.

RGB

The target is almost identical for this run group, but instead of liquid hydrogen, it is liquid deuterium. Therefore RGB is used for the electron-deuteron scattering and, by extension, the search for the d_s hexaquark. This run group also differs from RGA by not having the FT triggers active. The beam energy ranges for the chosen RGB run periods from 10.2 to 10.6 GeV; the author queried the Run Condition DataBase (RCDB) [75] to ensure accurate beam energies were used for all analyses of both RGA and RGB. The run periods used are the inbending runs of Spring 2020, outbending and intending runs from Fall 2019, and the inbending runs of Spring 2019.

4.2 Data Reconstruction

The raw electronic signals output by the detector systems described in Chapter 2 cannot be used to select events. First, it must be translated into physical quantities like momentum, energy, charge, which can be used for identification of the particle species. This is achieved through a process known as "cooking". This cooking process involves taking the raw data and using collaboration and reconstruction algorithms, specific to each detector subsystem, to extract the physical quantities into another file format [76]. For example, signals from the wires in the drift chambers are matched to patterns corresponding to a particles' trajectory.
The raw data is stored in the Event Input-Output (EVIO) data format, a flexible data container that minimizes disk access [77]. This raw data is recorded on an event-by-event basis, with information like the detector system, including, to continue the example of drift chambers; region, layer and drift time signal shape. Events are defined by one of the various triggers mentioned in Section 2.2.5 being taken as its beginning.

4.2.1 Calibration and Cooking

The process of calibration is applied to every detector subsystem in CLAS12. How it is done is slightly different for each subsystem, but generally, a combination of simulated data and cosmic ray runs are used to build the Calibration Constant DataBase (CCDB). The CCDB is then accessed for every experimental run to calibrate the raw analogue signals the subsystems receive into the digitized raw data [76, 61].
The cooking process, as mentioned earlier, is the process applied to the digitized calibrated raw data to be in a "human-readable" form. Digitized signals are decoded by algorithms, converted into physical quantities such as momentum, and saved into HIgh Performance Output (HIPO) files. These HIPO files have labelled data banks that can easily be accessed on an event-by-event basis either through the terminal, a quick manual check, or by software for analysis.

4.3 Event Selection

The first step in the event selection process is to skim the cooked data from the JLab servers. This cooked data are in HIPO files [78]. This format is used for a few reasons [76], it has fast compression, allows access to data based on the content of the event and can be easily accessed by ROOT [79], the chosen analysis framework for this research. Specifically, the HIPO files are accessed using clas12root [80], a software package developed to access CLAS12 data using ROOT. It is a streamlined way of using user-written macros to access event and particle data, such as the momentum of a particle or the number of particles in an event. This information is pulled from the HIPO files and placed into a file format called a ROOT TTree, facilitated by a ROOT macro made by the author. This is for two main reasons: the files are smaller, and they can be kept locally and are therefore more easily worked on. The other reason is that the analysis software used is ROOT. The events that make it into the TTree are selected due to the requirement for those events to have particular particles (see Sections 4.3.1 and 5.3), and those particles have certain kinematic restrictions. Once saved in the TTrees locally, a ROOT macro is used to analyse them, and further cuts are applied to this smaller data sample for the purposes of removing the background and getting different information from different subsets of the data.

4.3.1 Particle Identification

The events that make it past the initial skim and into the TTree for further analysis have to pass a filter that checks for a minimum number of various particle species. This is the same for RGA and RGB despite the different reaction channels being studied. For both of these run groups, this analysis requires at least one of the following: electron, K^+, proton and π^-. With many particle species, the signals in any single detector can be hard to discriminate, but using multiple detectors in conjunction with one another can give enough information to determine particle ID, as described below.

Event Builder PID

The CLAS12 Event Builder Particle IDentification (PID) uses two main measurements beta (β), which is acquired from the particles TOF and defined in Equation 4.1 and momentum, which is determined from the curvature of the path of the particle from the magnetic fields. For forward particles, the DC acquires the momentum, and FTOF measures the TOF of charged particles. Then, for the charged particles with larger polar angles, there are the CVT and CTOF for the same measurements. Figure 4.2 illustrates how β_{TOF} and momentum measurements can be used in conjunction with the nominal β_{calc} versus momentum function from Equation 4.2 to ID particles.

$$\beta_{TOF} = \frac{L}{ct} = \frac{v}{c} \tag{4.1}$$

$$\beta_{calc} = \frac{P}{\sqrt{P^2 + m^2}} \tag{4.2}$$

Where t is the TOF, taken from either of the TOF systems and L is the path length; this can be measured by combining signals from the TOF systems and the DC or CVT and drawing a curved path from the separate hit points. c is the speed of light, P is the momentum used as a range for the nominal β_{calc} vs P functions and the P data comes from the DC or CVT. Finally, m is the nominal mass of the particle in question used in Equation 4.2 to form the β_{calc} vs P functions in Figure 4.2. Neutrals in the FD are detected in the ECAL and/or the FTOF and do not correspond to changed particle tracks. The CND and the CTOF are the equivalent particles for larger polar angle neutral particles. For further discrimination between particles, there are the Cherenkov counters. This helps in the assignment of m for giving the particle a particular PID.

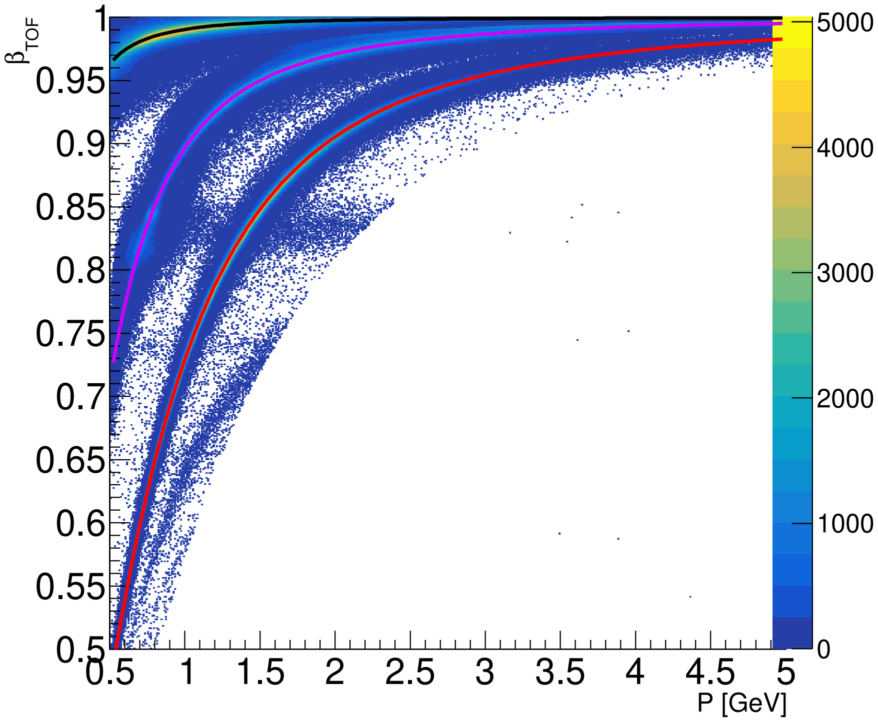

Fig. 4.2 A 2D histogram of β_{TOF} VS P with a χ^2_{PID} cut of < 5. There are three functions of β_{calc} vs P for three different particles. Black is for the π^-, pink is for the K^+ and the red line is the proton.

χ^2_{PID}

A particular particle track cannot be assigned the label of a specific species only when it perfectly matches the nominal β_{calc} VS P functions, as there is uncertainty in the measurements. The χ^2_{PID} is essentially a measure of how far data sits from the β_{calc} VS P function for the particle in question. A χ^2_{PID} of 0 is precisely of said function and every particle track is assigned a χ^2_{PID} where $|\chi^2_{PID}| \geq 0$. To select a particle with greater purity only tracks with $|\chi^2_{PID}| \leq a$ where a is some value, and this leads to a symmetric cut applied to either side of the nominal function so that any track that has been reconstructed with its β and momentum between the cut is labelled as the particle in question. The effects of the χ^2_{PID} can be seen in the plots in Figure 4.3. It is quite clear that as the maximum allowed χ^2_{PID} value decreases, the events surrounding the bands corresponding to the particles get cut out symmetrically around the band. For the purposes of this research, the original selection cut for data reaching the TTree stage was all hadrons to have a $|\chi^2_{PID}| \leq 5$; for the final analysis, this was reduced to 3.

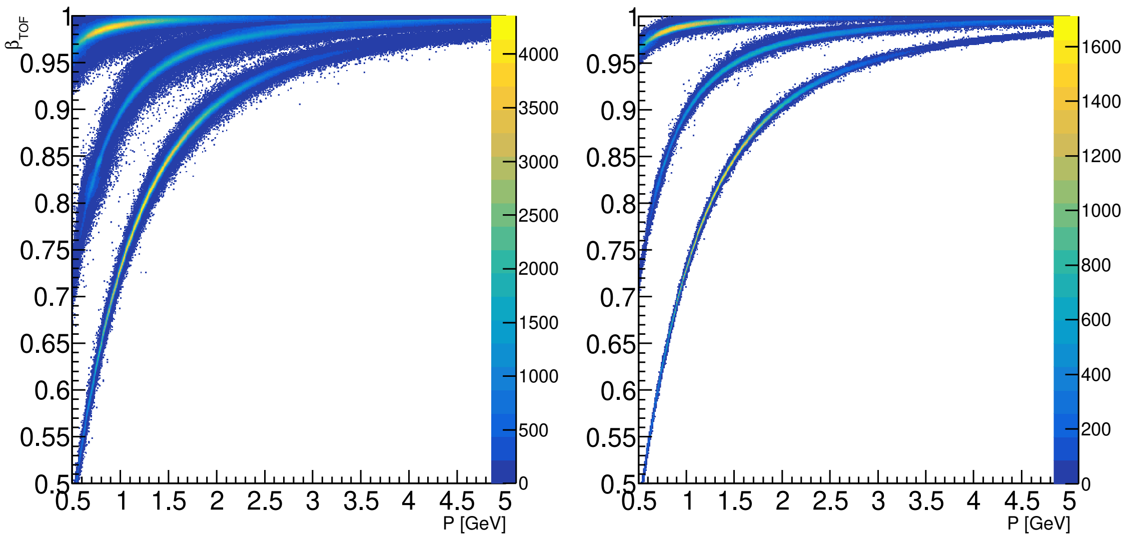

Fig. 4.3 Two 2D histograms of β_{TOF} VS P also from the RGA data. On the left is the data with a cut on the $|\chi^2_{PID}|$ of ≤ 3. On the right is the data with a cut on the $|\chi^2_{PID}|$ of ≤ 1.

Kinematic Restrictions

Another major cut on the data performed at the TTree stage is a kinematic one, where events are only further analysed if all the charged particles are reconstructed by the FD region of CLAS12. This cut is applied mainly due to the difficulties with accurately reconstructing the momentum of particles that land in the CD region of CLAS12. This issue will hopefully be resolved once the data has been processed by the pass 2 calibration (this is discussed further in Section7.1).

4.4 Summary

To go from the raw data on the CLAS12 computer farm to the data analysed by the author locally to produce the results seen in Chapters 5 and 6, the followingsteps are followed. The raw data is cooked and stored in the HIPO file format, this is then queried for the requirement outlined. The electron is needed in the FD selected through PID, and then there is a condition for the event to have at least one of the following hadrons: K^+, proton and π^-. The hadrons are selected with their PID values in combination with a $|\chi^2_{PID}|$ value ≤ 5. These hadrons are also required to fall on the FD and this data is stored in a ROOT TTree saved locally and analysed by ROOT.

Chapter 5

Data Analysis

This chapter will describe and explain how the data that has been skimmed by the ROOT Tree maker code described in the previous chapter will be analysed by ROOT macros designed by the author to, cut on specific aspects of the data in order to select particular channels. Starting with a summary of the tools used in event selection. Then, an explanation of why the bump hunt was an abandoned search method is given, followed by a description of the channel used in the final search along with the cuts applied to select that channel.

5.1 Missing and Invariant Mass

Given a generic channel described by Equation 5.1 we can select particles in the following ways depending on what we reconstruct.

$$eT \rightarrow e'AB \rightarrow e'ACD \tag{5.1}$$

Where e is the electron from the beam, T is the target, e' is the scattered electron, A and B are particles formed from the initial scattering event and C and D are daughter particles of B where it decays in the following way $B \rightarrow CD$.
When considering a particle that is not directly reconstructed by detector systems, one can use a concept known as missing mass to reconstruct the particle. In general, the missing mass of a particle is calculated through the conservation of the four momenta of a reaction. Taking A to be the particle not asked for from the event reconstruction, it can be reconstructed via Equation 5.2

$$M_A^2 = (P_e + P_T - P_{e'} - P_C - P_D)^2 \tag{5.2}$$

Where M_A is the mass of the missing particle A and P_X is the four-momentum of the particle subscripted, defined as $P = (p_x, p_y, p_z, M)$. Where $p_{x,y,z}$ are the Cartesian momentum components of the particle, and M is the mass of the particle.

The invariant mass is similar in concept but used instead to reconstruct a particle from the four momenta of its decay products illustrated by the invariant mass of particle B in Equation 5.3.

$$M_B^2 = (P_C + P_D)^2 \tag{5.3}$$

Where M_B is the invariant mass of particle B, and both P_C and P_D have the same meaning as in Equation 5.2. After selecting the reconstructed particles, the chosen channel can be separated from major background contributions using these in conjunction with each other.

5.2 Bump Hunt

As explained in Section 3.3, an integral requirement for the bump hunt search via the $\Delta\Sigma^*$ decuplet baryons was the reconstruction of the K^0. As it decays most commonly via the $K^0 \rightarrow \pi^+\pi^-$ channel, the $M_{K^0}^2 = (P_{\pi^+} + P_{\pi^-})^2$ invariant mass was plotted to see if it could be reconstructed. It could not, and therefore, this was pursued no longer. The issue of low acceptance was also mentioned, and it is illustrated in Figure 3.4; both the issues surrounding the reconstruction of K^0 and the acceptance-based issues may get fixed with the introduction of pass 2 data as this will allow the use of data from the CD allowing for roughly order of magnitude increase in statistics which with a final state of such high multiplicity is required.

5.3 Channel Selection for Polarization Analysis

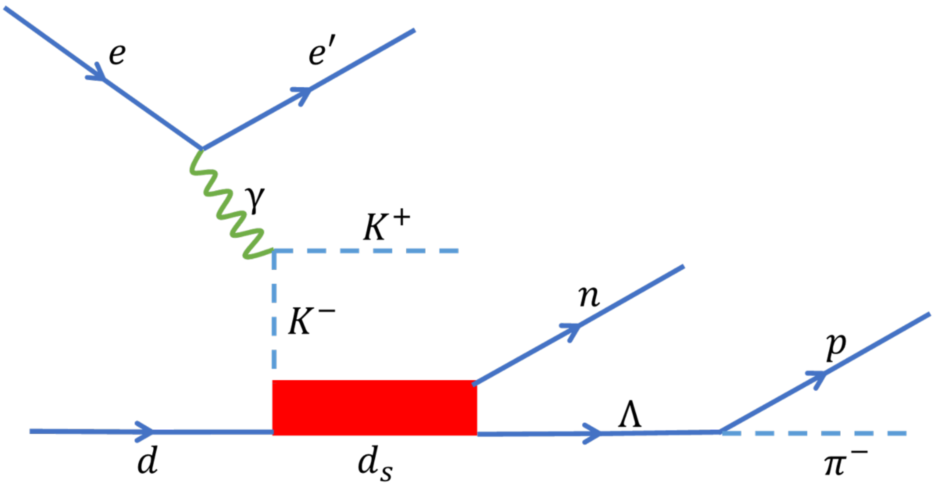

Fig. 5.1 The interaction seen Equation 5.4 as a Feynman diagram. The d_s^0 is formed by the interaction between the deuteron and the virtual negative counterpart to the reconstructed K^+, produced in flight. It then decays into the neutron and the Λ, which itself decays via the proton π^- decay branch.

Due to the formation of the d_s^0 having such a high sensitivity to polarization (as discussed in Section 3.4) and the easiest route to polarization extraction for this singly strange object being Λ production, the reaction channel chosen for the final d_s^0 search is the following:

$$ed \rightarrow e'K^+d_s^0 \rightarrow e'K^+\Lambda n \rightarrow e'K^+p\pi^-n \tag{5.4}$$

There is also the $d_s^+ \rightarrow \Lambda p$ channel, but this requires a K^0 to conserve strangeness, and as discussed in Section 3.3, the K^0 invariant mass could not be successfully reconstructed. The method of how this channel is separated from the full data set will be outlined. Although the detection of neutral particles is possible with CLAS12, it is always a challenge and has low acceptance. Therefore, only charged particles were reconstructed using the event builder PID for this research.
For a thorough investigation of the Λ polarization from the d_s^0 decay, it is appropriate to compare it with the same data with kinematic restrictions so it is likely that no d_s^0 formed. This is the same final state as the reaction in Eqaution 5.4, but the neutron here has a lower momentum than its counterpart from the d_s^0 decay and is considered a "spectator" (is not actively involved in the reaction) to the reaction; the precise value for the threshold momentum for this is given later in this section. Due to this subset of RGB data having this spectator neutron, it is analogous to the RGA data, specifically the reaction shown in Equation 5.5. These two data subsets should both be considered electroproduction of Λ off a proton target and, therefore, have the same behaviour in the three polarization components.

$$ep \rightarrow e'K^+\Lambda \rightarrow e'K^+p\pi^- \tag{5.5}$$

The plots being discussed in this section were used to illustrate two major things. Firstly, the purity of the channel selection and particles being selected, like the missing neutron for the RGB data. Secondly, to justify other cuts being made, such as the cut on the kinematics of the Λ.

5.3.1 Missing and Invariant Masses

To select the relevant RGA data after the initial skim, the exclusive missing mass is used, which is defined by Equation 5.6. This missing mass is plotted in Figure 5.2; it has a strong peak around 0 GeV^2 on top of a relatively smooth background. This is expected because if one compares Equations 5.5 and 5.6, it is clear that in the reaction of interest, there are no particles left to produce a missing mass in the desired reaction channel studied with the RGA data.

$$M_{Ex}^2 = (P_e + P_{p_T} - P_{e'} - P_{K^+} - P_p - P_{\pi^-})^2 \tag{5.6}$$

$$M_n^2 = (P_e + P_{d_T} - P_{e'} - P_{K^+} - P_p - P_{\pi^-})^2 \tag{5.7}$$

Where P_{p_T} and P_{d_T} are the four-vectors of the target proton and deuteron, respectively, M_{Ex} is the exclusive missing mass for the RGA data, and all the other variables have their meanings from Equation 5.2.

The other peak is seen at about 0.25 GeV^2; this is likely due to the presence of a kaon as the mass of the charged kaons is 0.494 GeV, and the K^0 mass is 0.498 GeV. The placement of the cut is chosen for the following reasons: it is symmetric, which works well for this quantity as it is directly around 0 GeV^2, and the value of 0.02 GeV^2 is chosen to cut out any pions that peak at about 0.02 GeV^2, while conserving statistics.

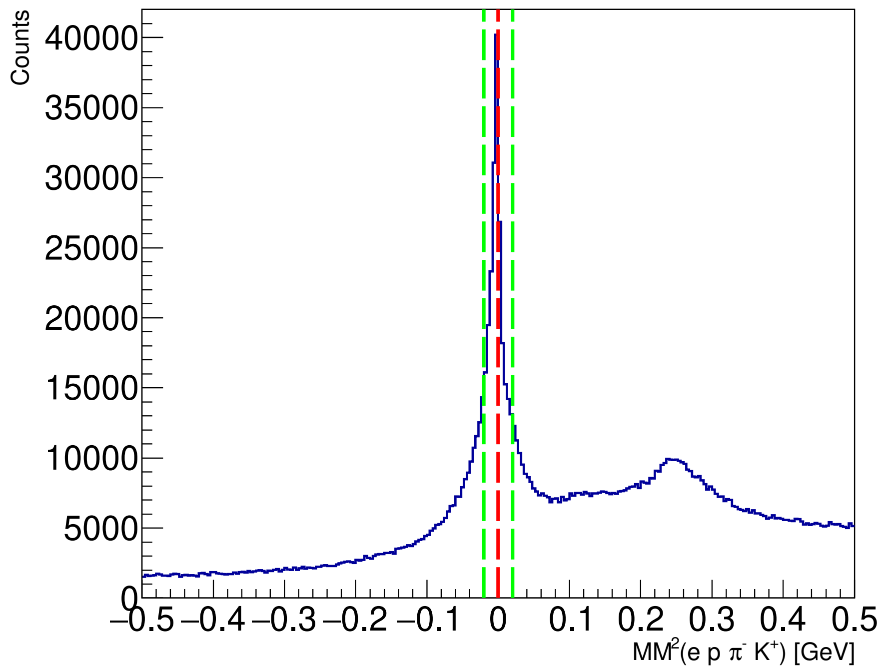

Fig. 5.2 1D histogram of the exclusive missing mass of the RGA data. The red dashed line is placed at 0 GeV, and the green dashed lines are placed where the missing mass cut limits are.

A similar quantity is used for the selection of the correct reaction in the RGB data. This is the missing mass of the neutron (both RGB subsets have a not directly reconstructed neutron in their reactions) defined by Equation 5.7 and plotted in Figure 5.3. In this plot, there is a smooth background that rises in counts along with the missing mass. The red dashed line in Figure 5.3 indicates the nominal neutron mass of 940 MeV [81], and there is a peak in this region. The shoulder at the missing mass of just over 1.2 GeV is likely due to a Δ baryon. The cut range choice was made by fitting the peak with a Gaussian function and placing the cuts at mean $\pm 2\sigma$ rounded to the nearest 10 MeV. Two standard deviations were chosen due to the presence of the aforementioned shoulder, as a three standard deviation cut would have included too many events from this shoulder, but if a one standard deviation cut were used, it would have been too strict and left out a lot of valid events.

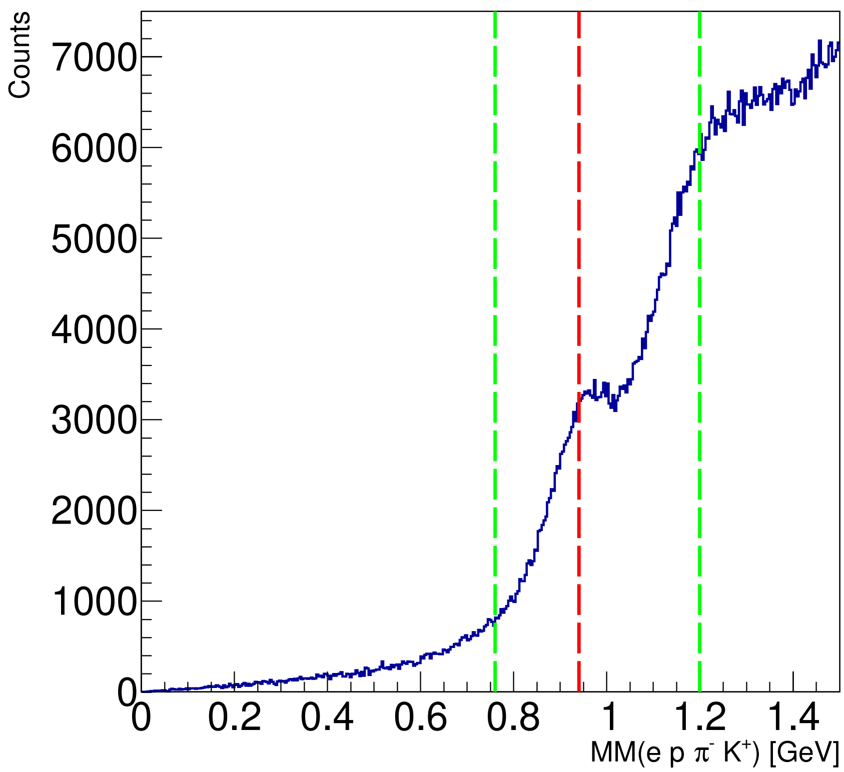

Fig. 5.3 1D histogram of the missing mass defined by Equation 5.7. The red dashed line is at 940 MeV, which is the neutron mass, and the green dashed lines are where the cuts on the data are placed.

After applying a cut on the missing neutron mass between 0.76 and 1.2 GeV, the invariant mass of the proton and π^- for the RGB data is produced, shown in Figure 5.4. The same plot for RGA is produced (also in Figure 5.4) after a symmetric cut around ± 0.02 GeV on the exclusive missing mass. The invariant mass is plotted in search of the Λ and defined as $M_\Lambda^2 = (P_p + P_{\pi^-})^2$ for both RGA and RGB.

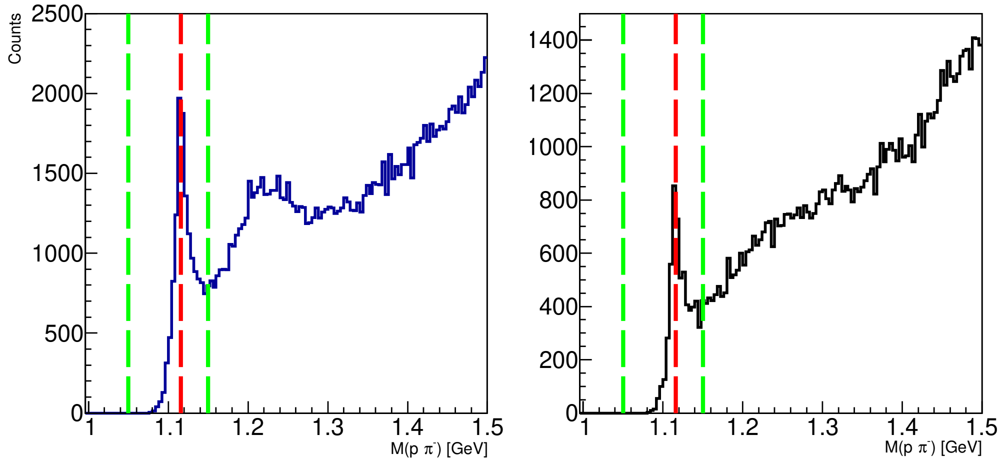

Fig. 5.4 Two 1D histograms of the invariant mass of the proton and π^-. On the left is data from RGB, and on the right, RGA data is shown. In both plots, the red dashed line is at the mass of the Λ 1116 MeV and the green dashed line show where the cuts on these data are placed.

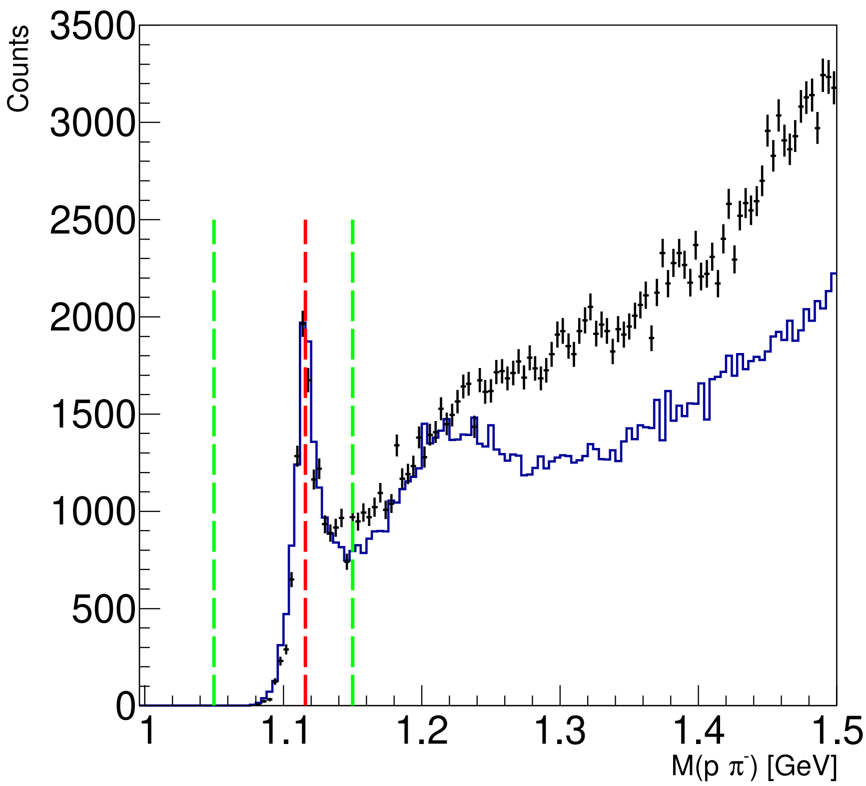

Fig. 5.5 Blue histogram is the RGB data, and the black histogram RGA data scaled so the Λ peaks match the same height. The dashed lines have the same meaning as in Figure 5.4.

As previously stated, all three data subsets are used to study ΛK^+ electroproduction, and the invariant mass of the proton and the π^- is plotted to see evidence of the Λ. The peak in the invariant mass indicating the decay of a Λ is seen directly on the nominal mass of the baryon for both data sets indicated by the red dashed line at 1116 MeV [72]. In Figure 5.5 the Λ peak from the RGA data is scaled to the Λ peak height of the RGB data to see the difference in shapes of the peak and background. From this plot, it is clear that the peaks are almost identical. The background of the RGA data rises with the invariant mass, and it does this faster than the RGB data. The RGB background also has a secondary peak at just above 1.2 GeV, likely a Δ baryon. This peak is absent in the RGA data due to the reasonably tight cut on the exclusive missing mass, meaning these events are less contaminated by the background. In comparison, the selection of the interaction defined in Equation 5.4 is not as clean as events with the Δ are included in the missing neutron mass cut. These events are likely from events where the "kaon" is a misidentified pion, and this would have to be the case for the Δ in the invariant mass due to the conservation of strangeness.

5.3.2 RGB Specific Variables

Once a cut on the invariant Λ mass of more than 1.05 GeV and less than 1.15 GeV for both RGA and RGB data is applied, there is an RGB-specific cut applied. This is to split the RGB data into two subsets. The first is used to compare and contrast with the RGA data, which is the subset with the spectator neutron. The other subset is the data used directly in the d_s search, which has a neutron that has enough momentum to be considered a participant in the reaction. The missing neutron momentum is plotted in Figure 5.6 to ascertain the best place to cut on this measurable. This is to separate the RGB data into two separate subsets: the data with the spectator neutron and the data with the participant neutron. The theoretical momentum distribution which essentially is the fermi momentum of the neutron, shows the momentum distribution of a spectator nucleon plotted in Figure 5.7 illustrates that the experimental peak structure is wider than predicted. This is likely due to the resolution of CLAS12 being too large to reproduce the theoretical curve accurately. The decision was made to place the spectator/participant neutron separation cut at 300 MeV due to the wider nature of the peak in the distribution.

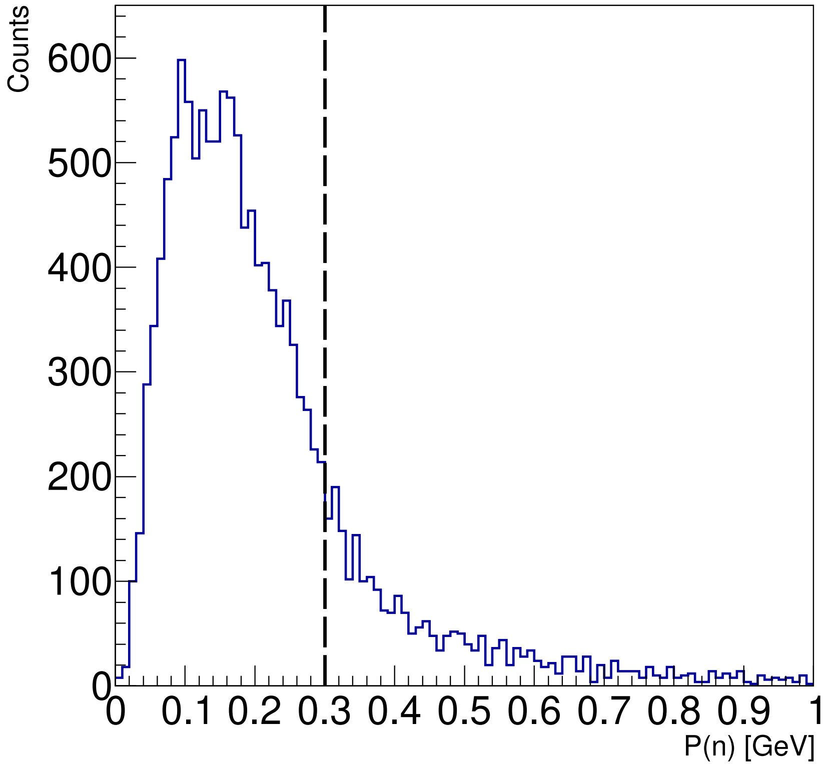

Fig. 5.6 Momentum of the missing neutron plotted in a 1D histogram. All data to the left of the black dashed line is considered the spectator neutron, and all data to the right of it is the participant neutron.

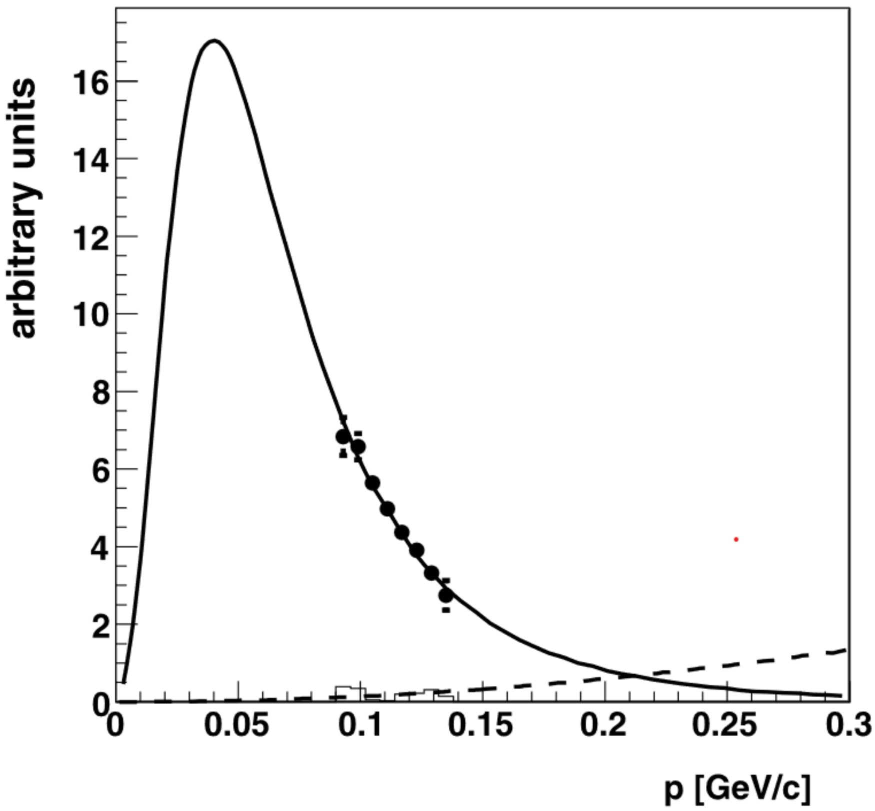

Fig. 5.7 The black curve is the momentum of a spectator nucleon [70], illustrating the similarity in the shape of this and the data in Figure 5.6.

The observable used to look for evidence for the d_s^0 is the polarization, specifically $P_{y'}$ (although $P_{x'}$ and $P_{z'}$ will also be shown), and as described in Section 3.6, this must be plotted against the missing mass defined by Equation 5.8 to perform the search.

$$M_X^2 = (P_e + P_{d_T} - P_{e'} - P_{K^+})^2 \tag{5.8}$$

Where M_X depends on the data subset being considered, in the case of the RGB data with the participant neutron, this should be the missing mass of the d_s. If, instead, the RGB data with the spectator neutron is being analysed, then the mass does not have a simple physical relation. Finally, with the RGA data, it is different again as, in this case, the target is a proton, and therefore, for the purposes of this calculation only, the missing mass is artificially shifted by using the target mass of the mass of a deuteron in order to compare the same missing mass range directly.

A final cut is applied only to the subset of the RGB data used to search for evidence for the d_s; this is the RGB data with the participant neutron. The cut is on the polar angle (θ) of the Λ after being boosted to the rest frame of the d_s with respect to the non-boosted d_s momentum vector ($\theta_{d_s}^{\Lambda}$). This is plotted in Figure 5.8 to decide where to cut on this measurable best.

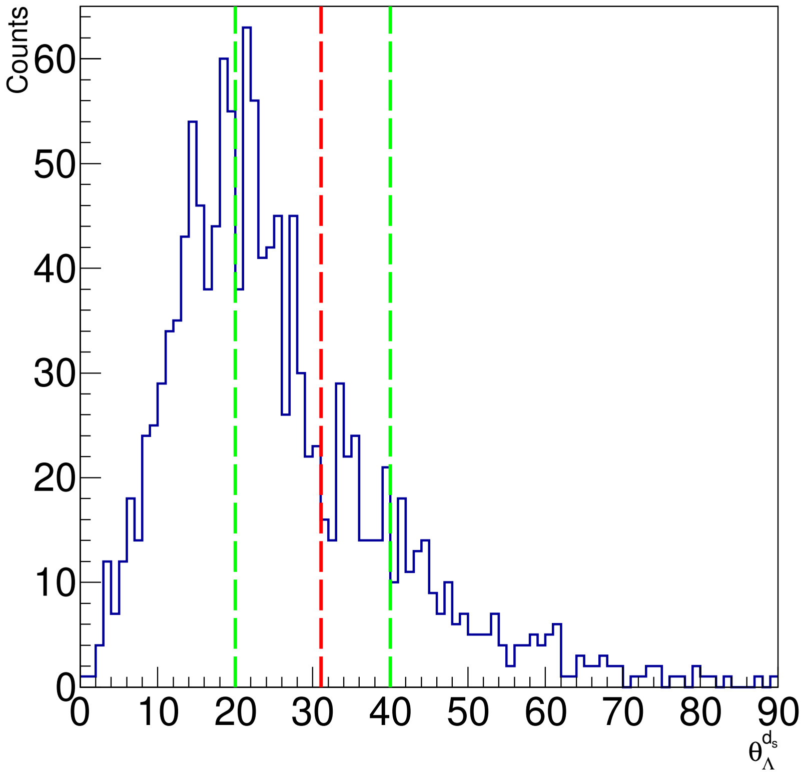

Fig. 5.8 The polar angle ($\theta_{\Lambda}^{d_s}$) of the Λ in the rest frame of the d_s with respect to the non-boosted d_s momentum vector. The red dashed line is the value of $\theta_{\Lambda}^{d_s}$ corresponding to the secondary peak in Figure 5.9. The green dashed lines indicate where the cuts were placed on the variable.

After the assessment, the cut is applied between 20° and 40° for two reasons. The peak can be seen just below about 15°, and the counts drop to near zero by about 70°, so the cut preserves statistics. The second reason is due to the secondary peak in the associated Legendre polynomial corresponding to $\cos 31.09°$ seen in Figure 5.9; the cut is nearly symmetric around the angle of interest (indicated by the green dashed line).

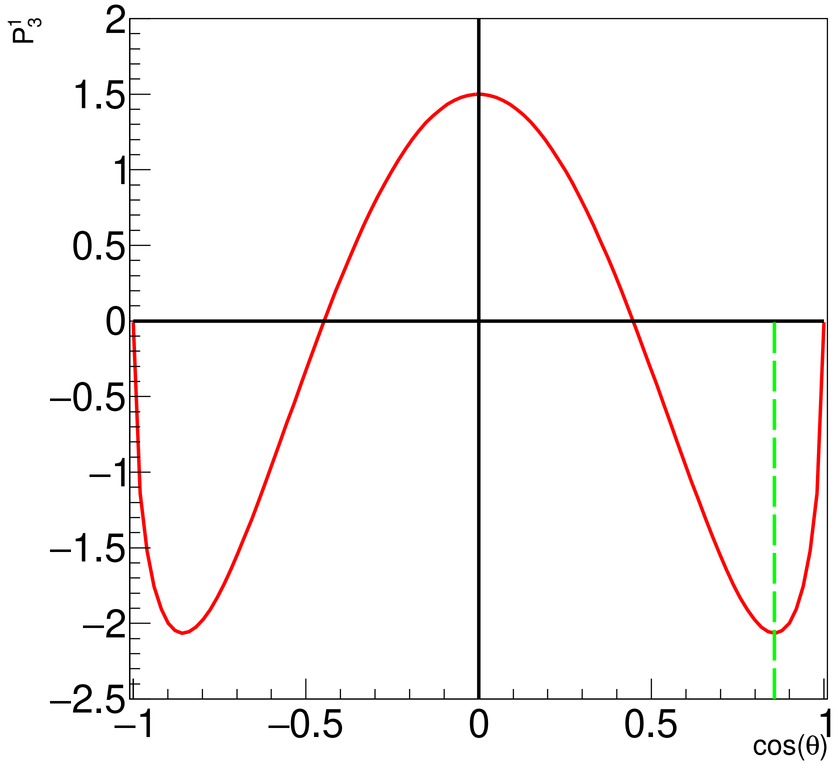

Fig. 5.9 Associated Legendre polynomial with the secondary peak corresponding to $\theta = 31.09°$ identified by the green dashed line.

5.4 Summary

The cuts applied to the different subsets were all described in this section. As well as the definition of the difference between the RGB data with the spectator neutron and the participant neutron. After applying said cuts and having as pure channels as this analysis will achieve, the next step is to plot the three components ($P_{x'}, P_{y'}$ and $P_{z'}$) of the polarization of the Λ for all three data subsets: RGA, RGB with the spectator neutron and RGB with the participant neutron (used in the direct d_s^0 search).

Chapter 6

Results and Discussion

In this chapter, all of the components of the Λ polarization are shown for all three data subsets: RGA, RGB with the spectator neutron and RGB with the participant neutron (used in the direct d_s^0 search). Every plot of polarization vs missing mass shown in Figures 6.1 to 6.3 shares the same recurring features. The vertical dashed lines from left to right: the black line is the Λn threshold, and the pink line is the $\Sigma^* n$ threshold; this is to catch potential interesting behaviour at these baryon resonance thresholds. Then to analyse the full range where evidence of the d_s^0 could possibly be seen outlined by the green dashed lines. The first green line is the mass of the d_s assuming a genuine hexaquark model ($M_{d_s(Hex)} = 2474$ MeV) minus the width calculated assuming genuine hexaquark ($\Gamma_{Hex} = 10.6$ MeV), placing the line at 2463.4 MeV and finally the second green line is the placed at 2669 MeV corresponding the mass ($M_{d_s(Mol)} = 2578$ MeV) plus the width ($\Gamma_{Mol} = 91$ MeV) of the d_s but this time considering the molecule model. The horizontal line is placed at $P_{x',y',z'} = 0$.
The data itself is represented as follows: blue square points are the RGA data, the red triangles are the RGB data with the spectator neutron, and the black circles are the RGB data with the participant neutron. Another feature in the polarization plots is the error bars on each point. The error in the missing mass is half the missing mass bin size, which is 100 MeV, so the error is ± 50 MeV. The error in the polarization component is calculated using a variation of Equation 6.1; this is the standard procedure to propagate the error of a variable that was extracted from other variables carrying their own errors.

$$\sigma_A = \sqrt{\left(\frac{\partial A}{\partial B}\right)^2 \sigma_B^2 + \left(\frac{\partial A}{\partial C}\right)^2 \sigma_C^2 + \ldots + \left(\frac{\partial A}{\partial Z}\right)^2 \sigma_Z^2} \tag{6.1}$$

Where $\sigma_{A(B,C,Z)}$ is the error in the sub-scripted variable and $\frac{\partial A}{\partial B(C,Z)}$ is the partial differential of, the equation that extracts the variable of interest (A), with respect to a variable in said equation. It is implied by Equation 6.1, but to make it clear, this sum of squares continues for all variables in the equation of interest. As a reminder, polarization in the case of this research is extracted with Equation 6.2.

$$P_A = \frac{2m}{N_0 \alpha} \tag{6.2}$$

Where P_A is $P_{x',y',z'}$, m is the gradient of the distribution of $\cos\theta$, N_0 is the acceptance corrected yield for a particular missing mass bin and α is the weak decay parameter (see Section 3.4.2 for the derivation of this equation and an in-depth explanation of the variables). With this knowledge, one can extract the partial differentials (Equations 6.3, 6.4 and 6.5) and, therefore, the error in the polarization component with Equation 6.6.

$$\frac{\partial P_A}{\partial m} = \frac{2}{N_0 \alpha} \tag{6.3}$$

$$\frac{\partial P_A}{\partial N_0} = -\frac{2m}{N_0^2 \alpha} \tag{6.4}$$

$$\frac{\partial P_A}{\partial N_0} = -\frac{2m}{N_0 \alpha^2} \tag{6.5}$$

$$\sigma_{P_A} = \sqrt{\left(\frac{4\sigma_m^2}{N_0^2\alpha^2}\right) + \left(\frac{4m^2\sigma_{N_0}^2}{N_0^4\alpha^2}\right) + \left(\frac{4m^2\sigma_\alpha^2}{N_0^2\alpha^4}\right)} \tag{6.6}$$

The final feature shared by all of the polarization plots is the missing mass range and the rolling binning used. The total range is 2 to 3.05 GeV, with two sets of ten missing mass bins, one set being positively shifted by 50 MeV relative to the first, which is ten 100 MeV wide bins ranging from 2 to 3 GeV. A rolling bin approach was used to get the most out of the poor statistics. It allowed for the ability to gain insight into the overall trend of the polarization components without using smaller bins that would require greater statistics. The errors in polarization described above do not account for this and this is more apparent in Section 6.2, where two more rolling bins are introduced. The bins overlap in the missing mass values they cover; therefore, the polarization errors should be combined. However, it can be argued that this extra accuracy to the errors is not necessary. Due to the fact that the goal of this thesis (which is fully explained in Section 6.2) is to acquire an upper limit to a Breit-Wigner peak describing the polarization and to ultimately prove accessibility to this channel for analysis upon improvements to the calibrations and, therefore, statistics once the data has gone through pass 2 which with it allowing the inclusion of data from the CD should allow for about an order of magnitude increase in statistics.

6.1 The Components of Polarization with a Vanishing Response Function

First, shown in Figure 6.1 is $P_{x'}$, from the theory presented in Section 1.3, we know the response function for this observable is zero in this data. The plot does not reflect that fact, which could be due to inaccurate acceptance corrections paired with low statistics. However, what is seen on the left of Figure 6.1 is good agreement between the RGA and the spectator neutron data from RGB, and although the largest divergence from zero is seen in the d_s^0 range of missing mass, as this is present in both data sets it is likely not from mixing of spectator and participant neutron data as the RGA data can not form a d_s^0. This agreement is encouraging due to the fact both data subsets are ΛK^+ electroproduction off a proton target. This helps verify the efficacy of the methodology despite the issues with statistics and acceptance corrections.

On the right-hand side of Figure 6.1 are both RGB data subsets. The ideal case again would be zero for the same reason as the data on the left. Although the data from the participant neutron subset does not behave in an ideal way, it mostly agrees with the other two data subsets.

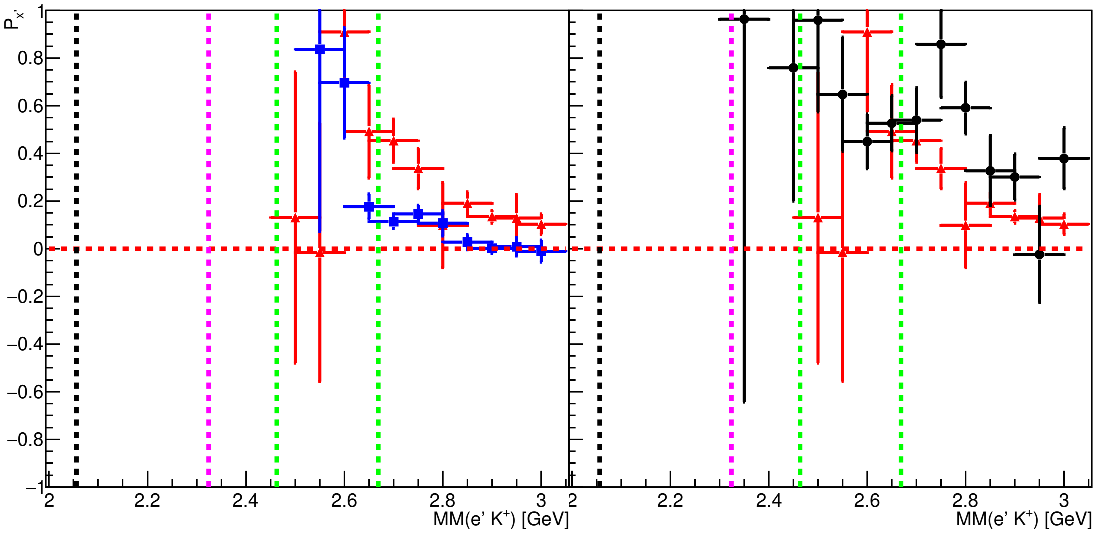

Fig. 6.1 Side by side view of two graphs both representing $P_{x'}$ vs MM(e'K^+) which is the missing mass defined in Equation 5.8. On the left, RGA data and RGB data with the spectator neutron are plotted together. The solid blue squares are RGA data, and the RGB with spectator neutron data is represented with red solid triangles. On the right is the data from both RGB subsets plotted together. The black solid circles are the RGB subset with participant neutron. The lines in both plots are as follows: black is the Λn threshold, pink is the $\Sigma^* n$ threshold, and the two green lines outline the range the d_s^0 is searched for.

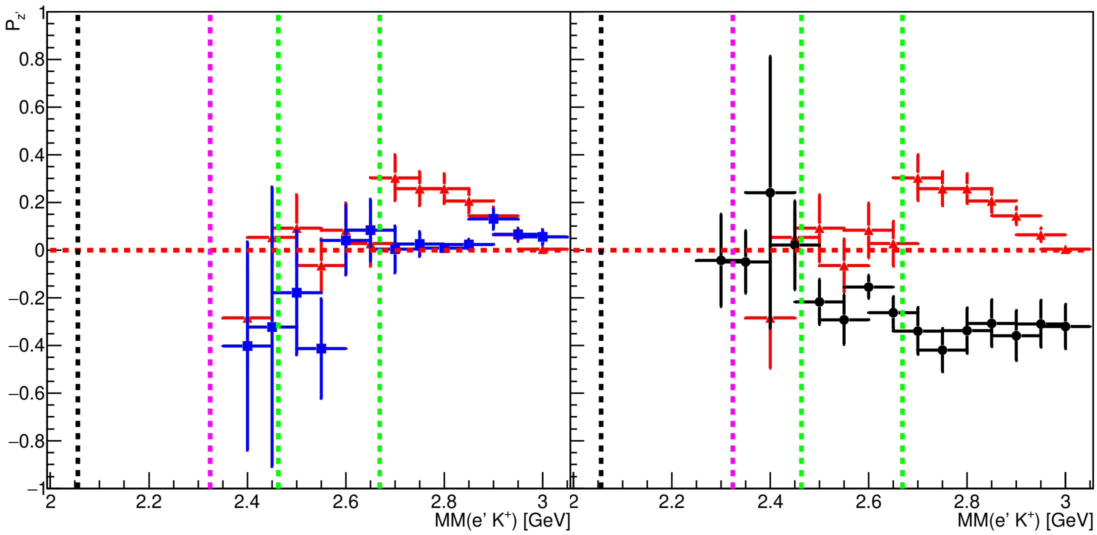

Fig. 6.2 Side by side view of two graphs both representing $P_{z'}$ vs MM(e'K^{+}) which is the missing mass defined in Equation 5.8. On the left, RGA data and RGB data with the spectator neutron are plotted together. The solid blue squares are RGA data, and the RGB with spectator neutron data is represented with red solid triangles. On the right is the data from both RGB subsets plotted together. The black solid circles are the RGB subset with participant neutron. The lines in both plots are as follows: black is the Λn threshold, pink is the $\Sigma^{*}n$ threshold, and the two green lines outline the range the d_s^0 is searched for.

Two plots of $P_{z'}$ are shown in Figure 6.2, and again from the theory presented in Section 1.3 the ideal case would be zero as it is for $P_{x'}$. The RGA data is close to this as it is relatively flat and near zero. Once again, the RGB data with the spectator neutron is mostly in agreement with the RGA data. There is a divergence in behaviour seen in the spectator neutron subset that begins with the point which has its bin centre at 2.75 GeV and ends for the point centred at 2.85 GeV. This could be again caused by issues with the acceptance corrections being paired with low statistics. The RGB data with the participant neutron is noticeably different from the other two subsets, which is encouraging in the way it further indicates a lack of mixing between the two RGB data subsets.
The key takeaway from these observables is that the RGA data and the RGB data with the spectator neutron are the most similar. This is good as they are both ΛK^{+} electroproduction off of a proton target. What is also apparent is that there are no sudden changes in the values, and any "peaks" are either too wide and, therefore, likely do not correlate with a resonance like the divergence from zero seen in the $P_{z'}$ of the RGB data with the spectator neutron. Or the peak in the $P_{x'}$ data seen in the RGA and RGB data, so this is just the same behaviour.

6.2 The Component of Polarization with a Non-vanishing Response Function

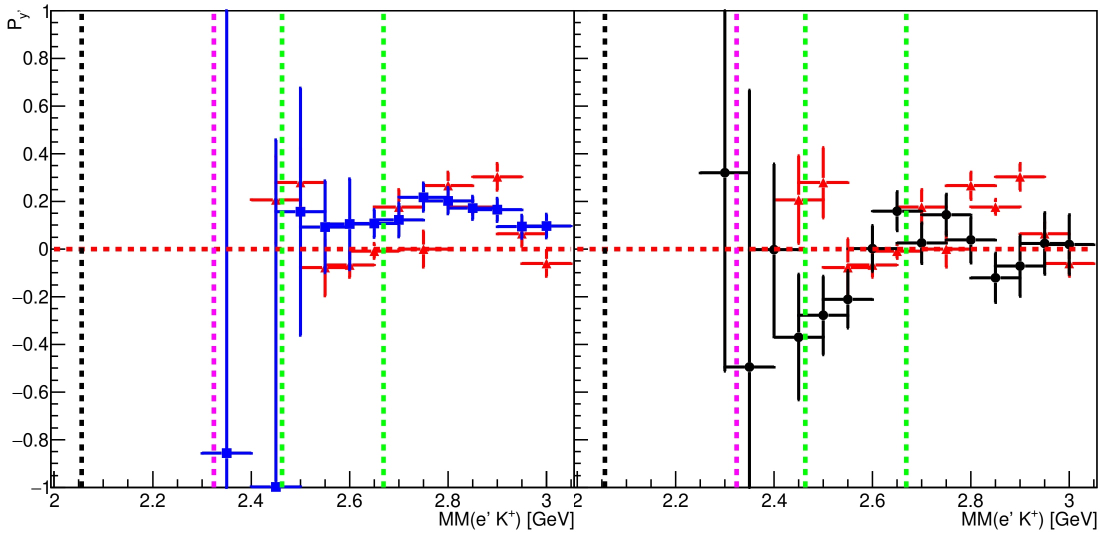

Fig. 6.3 Side by side view of two graphs both representing $P_{y'}$ vs MM(e'K^+) which is the missing mass defined in Equation 5.8. On the left, RGA data and RGB data with the spectator neutron are plotted together. The solid blue squares are RGA data, and the RGB with spectator neutron data is represented with red solid triangles. On the right is the data from both RGB subsets plotted together. The black solid circles are the RGB subset with participant neutron. The lines in both plots are as follows: black is the Λn threshold, pink is the $\Sigma^* n$ threshold, and the two green lines outline the range the d_s^0 is searched for.

This is $P_{y'}$, the component of polarization of most significant importance for the d_s^0 search and is plotted in Figure 6.3 for comparison purposes just like the components with a vanishing response function. $P_{y'}$ is the component with a non-vanishing response function and is where any changes and deviations in behaviour should be due to resonances. Taking into account the behaviours discussed above, any hints of evidence of the d_s^0 ideally would be a narrow peak all in the region identified by the green dashed lines, and this peak would have to be separate from behaviour seen in the RGA data and the RGB data with the spectator neutron. It is seen on the left of Figure 6.3 that the behaviour of $P_{y'}$ from RGA data and the RGB data with the spectator neutron is remarkably similar, especially in the region of 2.45 GeV to 3.05 GeV.

Then, in the right-hand side of Figure 6.3, it can be seen that the RGB data with the participant neutron is also very similar to the other data sets in the range between 2.6 GeV and 3.05 GeV. There is, however, a reasonable departure from the shared behaviour in the d_s^0 mass range depicted by the green dashed lines, specifically the points centred on 2.45, 2.5 and 2.55 GeV.

As the focus of this research is the analysis of this ΛK^+ electroproduction off of a deuteron target with an emphasis on the formation of the d_s^0 imparting polarization onto the daughter Λ and neutron (not measured here), a more in-depth look into the region of interest is required. The way this is done is by taking the plot of $P_{y'}$ vs $MM(e'K^+)$ and introducing two more rolling bins compared to the data points in Figure 6.3. Now the plot of $P_{y'}$ vs $MMe'K^+$, has four sets of ten missing mass bins with bin centres that are offset by 25 MeV from the previous set. This plot is then fit with a fourth-order polynomial plus a Breit–Wigner distribution; this convoluted function is represented by Equation 6.7. With no theoretical model for this data to make a more informed choice of background fit function, the choice of a fourth-order polynomial was made due to the behaviour of the data having three points of inflection.

$$y = ax^4 + bx^3 + cx^2 + dx + e + f\left(\frac{\left(\frac{\Gamma^2}{4}\right)}{(x-M)^2 + \frac{\Gamma^2}{4}}\right) \tag{6.7}$$

Where y would be the fit's predicted value of $P_{y'}$, x is the missing mass, a, b, c, d and e are parameters of the polynomial, f is the strength of the Breit-Wigner, Γ is the width of the Beit-Wigner and M is the missing mass bin centre value of the range 2450 to 2675 MeV fitting every 25 MeV step, totalling ten fits. Γ is varied by using the formalism outlined in Section 3.1; more precisely, the width is calculated by assuming a genuine hexaquark and using the mass from the centre of the missing mass bin that is being fit. From those fits, the strength of the peak f can be extracted along with an error for this value, and an upper limit of this peak strength can be determined, which is defined by the following relation $|f| + 2\sigma_f$.

Table 6.1 This is a summary of parameters of the Breit-Wigner function along with the values of the error in f (σ_f) and the upper bound extracted using the relation $|f| + 2\sigma_f$.

M [MeV]	Γ [MeV]	$\lvert f \rvert$	σ_f	Upper Bound
2450	8	0.008	0.282	0.572
2475	11	0.247	0.238	0.723
2500	18	0.024	0.219	0.462
2525	31	0.152	0.184	0.520
2550	54	0.172	0.148	0.468
2575	91	0.158	0.149	0.456
2600	139	0.308	0.183	0.674
2625	159	0.506	0.120	0.746
2650	159	0.401	0.156	0.713
2675	159	0.115	0.117	0.349

Figures 6.4, 6.5 and 6.6 show three different fits to the $P_{y'}$ data. First, in Figure 6.4, we can see the narrow spike in the fit. This is due to the fact that at the lower missing masses, there are lower

statistics and pairing this with the small widths in this region, any statistical fluctuation can produce a fit with relatively high peak strength. This is what leads to the leftmost peak seen in Figure 6.7.

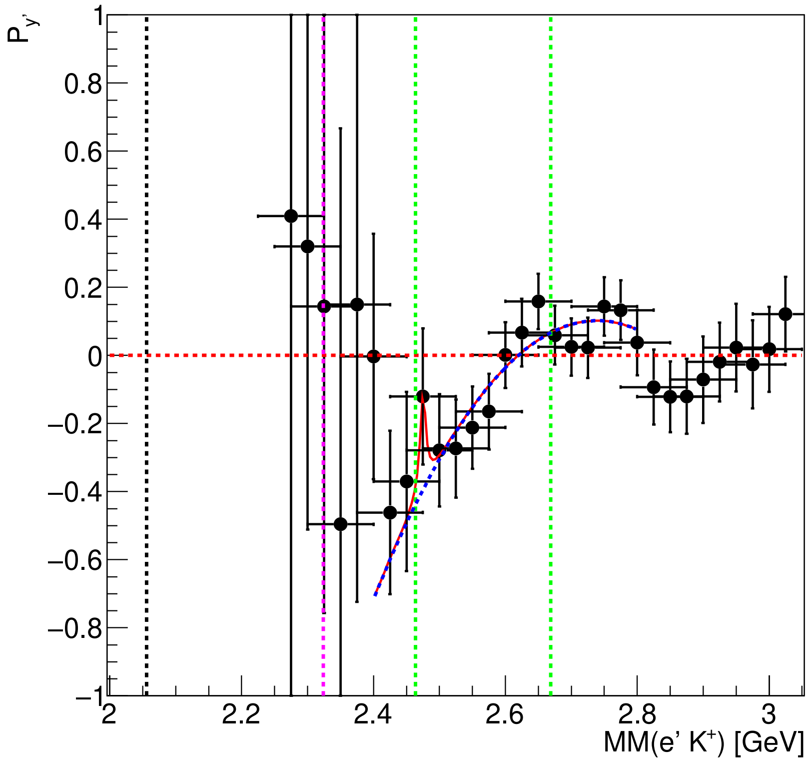

Fig. 6.4 A plot of the $P_{y'}$ of the Λ vs the missing mass defined in Equation 5.8. The black solid circles with black error bars are data from the RGB subset with the participant neutron, the red curve is the fit of the signal and background described by Equation 6.7, and the blue dashed curve is the fourth-order polynomial, which is the fit of just the background. Here, the mass used in the Breit-Wigner is 2475 MeV, and the width is 11 MeV.

Then, in Figure 6.5, we see a fit in a region where statistics are higher and the width is larger. Therefore, the peak strength is less reliant on small statistical fluctuations, but the peak strength and, subsequently, the upper limit is low here.

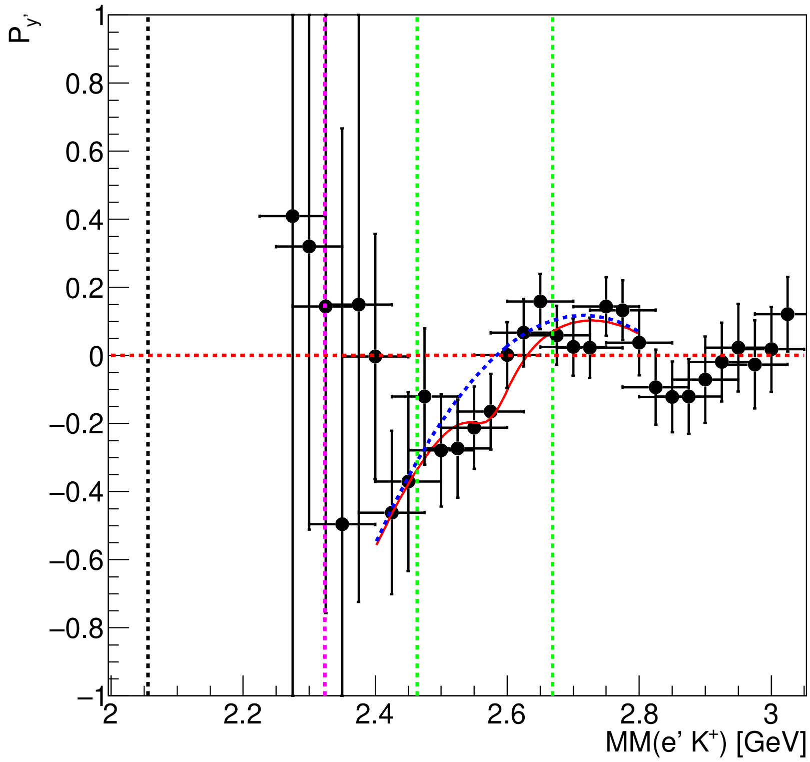

Fig. 6.5 A plot of the $P_{y'}$ of the Λ vs the missing mass defined in Equation 5.8. The black solid circles with black error bars are data from the RGB subset with the participant neutron, the red curve is the fit of the signal and background described by Equation 6.7, and the blue dashed curve is the fourth-order polynomial, which is the fit of just the background. Here, the mass used in the Breit-Wigner is 2575 MeV, and the width is 91 MeV.

Finally, Figure 6.6 does have the positives discussed concerning Figure 6.5, but as the background function diverges in behaviour from the other two plots shown, the large peak strength upper limit, brought about by this fit is to be taken with a grain of salt.

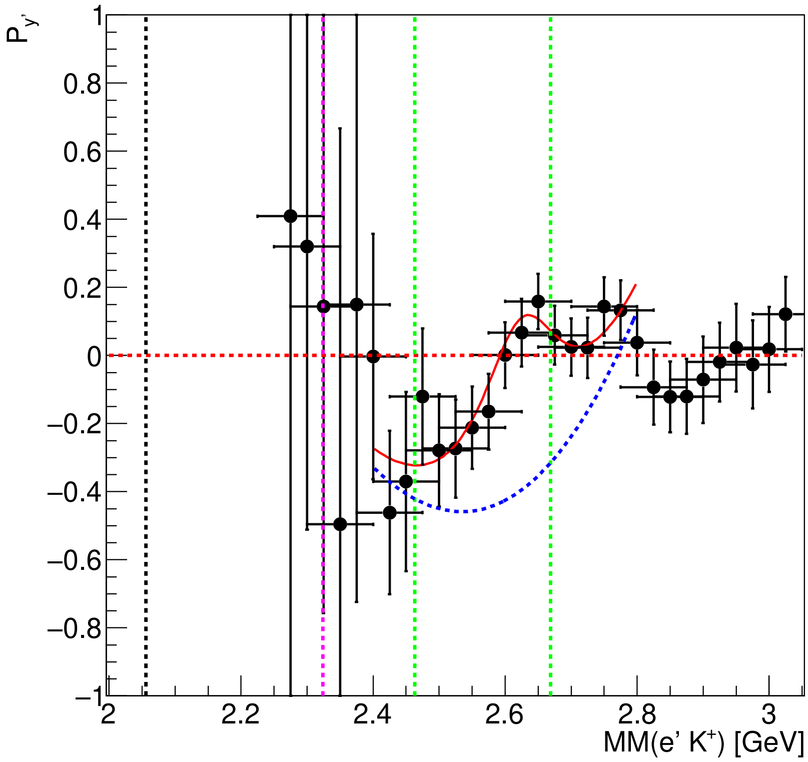

Fig. 6.6 A plot of the $P_{y'}$ of the Λ vs the missing mass defined in Equation 5.8. The black solid circles with black error bars are data from the RGB subset with the participant neutron, the red curve is the fit of the signal and background described by Equation 6.7, and the blue dashed curve is the fourth-order polynomial, which is the fit of just the background. Here, the mass used in the Breit-Wigner is 2625 MeV, and the width is 159 MeV.

Other fits vary in behaviour, mostly in accordance with these three main regions. In general, the upper bound of peak strength plotted in Figure 6.7 all lies above the blue dashed line placed at a value of 0.2, which indicates the peak strength extracted from the fitted peak seen in Figure 3.8 from the analogous analysis performed on the $d*(2380)$ seen in this paper [51]. As this is an upper limit, and strictly speaking, any value below the curve can be considered therefore, the comparison with this value is not perfect, but this is an important first step. This still means that with improvements in the data quality and the amount of available statistics, this channel will be good to analyse in search of evidence of the d_s^0.

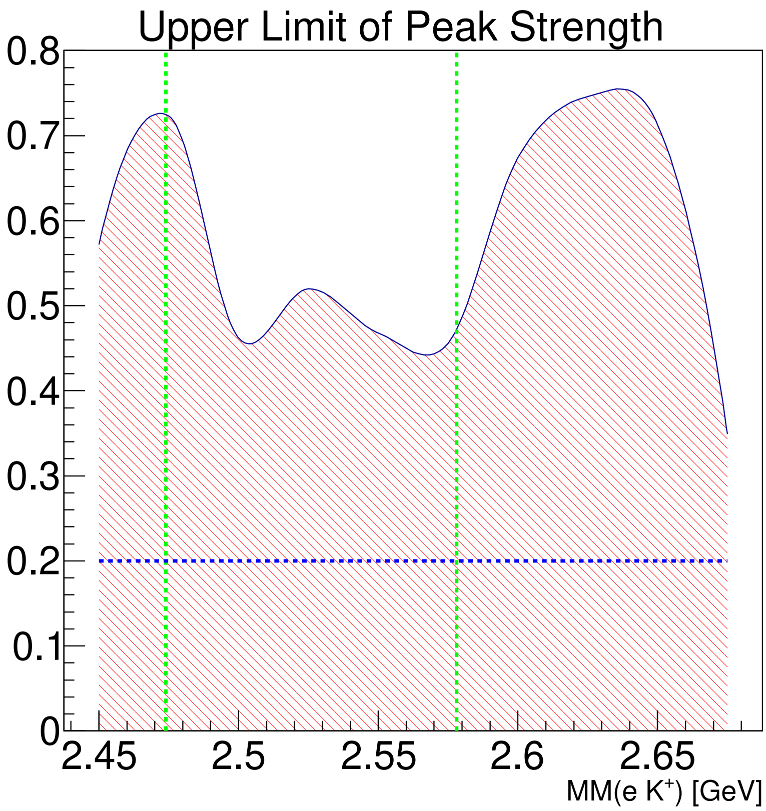

Fig. 6.7 The upper limit of peak strength (defined as the field strength plus 2σ plotted as a smoothed histogram against the missing mass defined in Equation 5.8. The green dashed lines here indicate the predicted mass of the d_s^0 assuming a genuine hexaquark structure at 2474 MeV, and the other is for the assumption of a 2578 MeV. The blue dashed line indicates the peak strength of the analogous analysis of the $d^*(2380)$ [51].

Chapter 7

Conclusion and Future Work

This final chapter will provide a full summary of the work presented in this thesis. Compiling all the main findings from the research and providing an outline of what future work can be done on this research and what this future work can improve on.

7.1 Conclusion

The first and most important thing to take away from this work is that this is the first measurement of the presented observables on this data and the first search for the d_s^0 hexaquark using the methodology outlined in this thesis. When it comes to making a conclusion from the search for the d_s^0, there is a hint of interesting behaviour of the component with a non-vanishing response function of the Λ polarization, P_y', in the RGB data subset with the participant neutron. An in-depth analysis of this observable was carried out in the region outlined by the green dashed lines in Figures 6.3, 6.4, 6.5 and 6.6. This search range is between missing mass values of 2463 MeV and 2669 MeV. The analysis was carried out by fitting this region plus some background with a fourth-order polynomial combined with a Breit-Wigner described by Equation 6.7. These fits allowed for the extraction of an upper limit on the peak strength of the Breit-Wigner distributions. This is plotted against the missing mass defined by Equation 5.8 in Figure 6.7; the behaviour in the region between the two predicted masses is certainly interesting. This is not enough to claim a discovery, which would take several studies of various decay channels, much like the catalogue of studies concerning the $d^*(2380)$. The question is then if this is, to paraphrase the original $d^*(2380)$ paper, a hint at this resonance? It is difficult to make that claim as there is no clear experimental evidence for the existence of this particle seen in the data presented in this thesis.

The argument is made, however, that the upper bound, along with the data discussed diverging from the behaviour of the other two data sets only in the particular missing mass region that the d_s is predicted to exist, encompassed by the green dashed lines in the polarization plots, could mean that there is the first hint of the d_s. This research in no way rules out its existence and does show that this channel, which was analysed for the first time in this thesis, has a non-vanishing cross-section and with improvements in statistics and data quality, it could be a promising channel to find the first experimental evidence of the d_s^0 as well as an interesting channel for hyperon-nucleon studies.

7.2 Future Work

First of all, the main issue with data is the low statistics; the biggest hope to address this is the pass 2 of both RGA and RGB. A major effort within the CLAS collaboration with the aim of improving calibrations, accuracy of particle reconstruction and better understanding of detector efficiency. The author had personal involvement in the process that has led to pass 2 by taking a lead role in producing energy corrections for FT-Cal as service work for the collaboration.

What should follow from said improvements should allow for the incorporation of data from the CD, which should provide a large jump in statistics along with the increased resolution required to reconstruct the K^0. Yet another improvement from pass 2 is the detached vertex reconstruction, which is very important when it comes to Λ production as it has a sufficient lifetime to have a detached vertex. This will not only help the analysis of the channel presented in this thesis but also will give access to other channels. This will not necessarily increase statistics to such a degree to see evidence of the d_s in missing or invariant mass, but it might allow for the inclusion of the $d_s \to \Lambda p$ channel for polarization studies; this channel is also currently hindered by the inability to reconstruct the K^0 successfully. Yet another hopeful improvement from the increased statistics would be the ability to access the angular kinematics that has the highest sensitivity to polarization in the case of the $8 \oplus 8$ decay of the d_s, where $\theta_{\Lambda}^{d_s} \approx 90°$.

Beyond what can be done with improved statistics is the use of a more realistic event generator, as opposed to the phase space only generator used in the work presented here. The improvement from this will come because acceptance corrections are important in polarization extraction. The improved event generator would have the ability to simulate particles as peaks with widths with realistic decay times and, therefore, having detached vertices.

7.2.1 Other Experiments

CLAS12 at JLab is not the only experiment that could be used in the hunt for the hexaquarks of the $J^p = 3^+$ anti-decuplet. Staying at JLab but moving to Hall D, where the K-Long Facility (KLF) will be housed. This will have a K^0-long beam incident on both liquid hydrogen and liquid deuterium targets [82]. This allows for not only d_s production but also the formation of d_{ss} and d_{sss}. This is due to the increased likelihood of strangeness in final states thanks to the strangeness of the beam. Another potential experiment for the hexaquark search does require movement from JLab, and this would be the Electron-Ion Collider (EIC) housed at Brookhaven National Lab (BNL). The EIC has a planned electron proton CM energy of 100 GeV [83], which would allow for potentially higher stats of the formation of the hexaquarks off of a deuteron target. While also allowing for the study of hexaquarks formed in the high-density environment found inside a nucleus as the EIC will use targets from protons to gold ions.

Bibliography

[1] *LVIII. On the masses of the ions in gases at low pressures*. en. DOI: 10.1080/14786449908621447. URL: https://www.tandfonline.com/doi/epdf/10.1080/14786449908621447?needAccess=true&role=button (visited on 07/31/2023).

[2] E. Rutherford. *LXXIX. The scattering of and particles by matter and the structure of the atom*. en. DOI: 10.1080/14786440508637080. URL: https://www.tandfonline.com/doi/epdf/10.1080/14786440508637080?needAccess=true (visited on 08/01/2023).

[3] "Bohr Model of the Atom". en. In: ().

[4] *LIV. Collision of particles with light atoms. IV. An anomalous effect in nitrogen*. en. DOI: 10.1080/14786440608635919. URL: https://www.tandfonline.com/doi/epdf/10.1080/14786440608635919?needAccess=true&role=button (visited on 08/28/2023).

[5] *The existence of a neutron*. en. DOI: 10.1098/rspa.1932.0112. URL: https://royalsocietypublishing.org/doi/epdf/10.1098/rspa.1932.0112 (visited on 08/28/2023).

[6] Hideki Yukawa. "On the Interaction of Elementary Particles. I". In: *Proceedings of the Physico-Mathematical Society of Japan. 3rd Series* 17 (1935), pp. 48–57. DOI: 10.11429/ppmsj1919.17.0_48.

[7] C. M. G. Lattes et al. "PROCESSES INVOLVING CHARGED MESONS". en. In: *Nature* 159.4047 (May 1947), pp. 694–697. ISSN: 0028-0836, 1476-4687. DOI: 10.1038/159694a0. URL: https://www.nature.com/articles/159694a0 (visited on 08/28/2023).

[8] V. D. Hopper and S. Biswas. "Evidence Concerning the Existence of the New Unstable Elementary Neutral Particle". en. In: *Physical Review* 80.6 (Dec. 1950), pp. 1099–1100. ISSN: 0031-899X. DOI: 10.1103/PhysRev.80.1099. URL: https://link.aps.org/doi/10.1103/PhysRev.80.1099 (visited on 08/28/2023).

[9] V. E. Barnes et al. “Observation of a Hyperon with Strangeness Minus Three”. en. In: *Physical Review Letters* 12.8 (Feb. 1964), pp. 204–206. ISSN: 0031-9007. DOI: 10.1103/PhysRevLett.12.204. URL: https://link.aps.org/doi/10.1103/PhysRevLett.12.204 (visited on 08/28/2023).

[10] M. Gell-Mann. “A Schematic Model of Baryons and Mesons”. en. In: *Resonance* 24.8 (Aug. 2019), pp. 923–925. ISSN: 0971-8044, 0973-712X. DOI: 10.1007/s12045-019-0853-x. URL: http://link.springer.com/10.1007/s12045-019-0853-x (visited on 08/28/2023).

[11] G. Zweig. “An SU(3) model for strong interaction symmetry and its breaking. Version 1”. In: (Jan. 1964).

[12] J. J. Aubert et al. “Experimental Observation of a Heavy Particle J”. en. In: *Physical Review Letters* 33.23 (Dec. 1974), pp. 1404–1406. ISSN: 0031-9007. DOI: 10.1103/PhysRevLett.33.1404. URL: https://link.aps.org/doi/10.1103/PhysRevLett.33.1404 (visited on 08/28/2023).

[13] S. W. Herb et al. “Observation of a Dimuon Resonance at 9.5 GeV in 400-GeV Proton-Nucleus Collisions”. en. In: *Physical Review Letters* 39.5 (Aug. 1977), pp. 252–255. ISSN: 0031-9007. DOI: 10.1103/PhysRevLett.39.252. URL: https://link.aps.org/doi/10.1103/PhysRevLett.39.252 (visited on 08/28/2023).

[14] F. Abe et al. “Observation of Top Quark Production in p ¯ p Collisions with the Collider Detector at Fermilab”. en. In: *Physical Review Letters* 74.14 (Apr. 1995), pp. 2626–2631. ISSN: 0031-9007, 1079-7114. DOI: 10.1103/PhysRevLett.74.2626. URL: https://link.aps.org/doi/10.1103/PhysRevLett.74.2626 (visited on 08/28/2023).

[15] Donald H. Perkins. *Introduction to high energy physics*. en. 4th ed. Cambridge ; New York: Cambridge University Press, 2000. ISBN: 978-0-521-62196-0.

[16] Robert Mann. “An introduction to particle physics and the standard model”. In: *An Introduction to Particle Physics and the Standard Model* (Jan. 2009). Publisher: CRC Press, pp. 15–20. ISSN: 9781420083002. DOI: 10.1201/9781420083002/INTRODUCTION-PARTICLE-PHYSICS-STANDARD-MODEL-ROBERT-MANN. URL: https://www-taylorfrancis-com.libproxy.york.ac.uk/books/oa-mono/10.1201/9781420083002/introduction-particle-physics-standard-model-robert-mann.

[17] Brookhaven National Laboratory. *Evolving View of the Proton*. Apr. 2022. URL: https://www.flickr.com/photos/brookhavenlab/51978766177/ (visited on 08/31/2023).

[18] A. P. Szczepaniak. "Modern hadron spectroscopy: a bridge between nuclear and particle physics." en. In: *Journal of Physics: Conference Series* 1014 (May 2018), p. 012017. ISSN: 1742-6588, 1742-6596. DOI: 10.1088/1742-6596/1014/1/012017. URL: https://iopscience.iop.org/article/10.1088/1742-6596/1014/1/012017 (visited on 11/18/2023).

[19] J. J. De Swart. "The Octet Model and its Clebsch-Gordan Coefficients". en. In: *Reviews of Modern Physics* 35.4 (Oct. 1963), pp. 916–939. ISSN: 0034-6861. DOI: 10.1103/RevModPhys.35.916. URL: https://link.aps.org/doi/10.1103/RevModPhys.35.916 (visited on 08/07/2023).

[20] Joseph R. Incandela et al. "Status and prospects of top-quark physics". en. In: *Progress in Particle and Nuclear Physics* 63.2 (Oct. 2009), pp. 239–292. ISSN: 01466410. DOI: 10.1016/j.ppnp.2009.08.001. URL: https://linkinghub.elsevier.com/retrieve/pii/S0146641009000520 (visited on 08/20/2023).

[21] R. P. Feynman. "Space-Time Approach to Quantum Electrodynamics". en. In: *Physical Review* 76.6 (Sept. 1949), pp. 769–789. ISSN: 0031-899X. DOI: 10.1103/PhysRev.76.769. URL: https://link.aps.org/doi/10.1103/PhysRev.76.769 (visited on 09/01/2023).

[22] S.-K. Choi et al. "Observation of a Narrow Charmoniumlike State in Exclusive B ± → K ± + J / Decays". en. In: *Physical Review Letters* 91.26 (Dec. 2003), p. 262001. ISSN: 0031-9007, 1079-7114. DOI: 10.1103/PhysRevLett.91.262001. URL: https://link.aps.org/doi/10.1103/PhysRevLett.91.262001 (visited on 09/12/2023).

[23] G. Knchlein, D. Drechsel, and L. Tiator. "Photo- and electroproduction of eta mesons". en. In: *Zeitschrift fr Physik A Hadrons and Nuclei* 352.3 (Sept. 1995), pp. 327–343. ISSN: 0939-7922, 1434-601X. DOI: 10.1007/BF01289506. URL: http://link.springer.com/10.1007/BF01289506 (visited on 09/19/2023).

[24] T. D. Lee and C. N. Yang. "General Partial Wave Analysis of the Decay of a Hyperon of Spin ½". en. In: *Physical Review* 108.6 (Dec. 1957), pp. 1645–1647. ISSN: 0031-899X. DOI: 10.1103/PhysRev.108.1645. URL: https://link.aps.org/doi/10.1103/PhysRev.108.1645 (visited on 10/28/2023).

[25] Klaus Peters. "A Primer on Partial Wave Analysis". In: *arXiv:hep-ph/0412069* (Dec. 2004). arXiv: hep-ph/0412069. URL: http://arxiv.org/abs/hep-ph/0412069 (visited on 06/21/2020).

[26] Kai-bao Chen et al. “Longitudinal and transverse polarizations of hyperon in unpolarized SIDIS and e + e annihilation”. en. In: *Physical Review D* 105.3 (Feb. 2022), p. 034027. ISSN: 2470-0010, 2470-0029. DOI: 10.1103/PhysRevD.105.034027. URL: https://link.aps.org/doi/10.1103/PhysRevD.105.034027 (visited on 11/26/2023).

[27] M. Gabrielyan et al. “Induced polarization of (1116) in kaon electroproduction”. en. In: *Physical Review C* 90.3 (Sept. 2014), p. 035202. ISSN: 0556-2813, 1089-490X. DOI: 10.1103/PhysRevC.90.035202. URL: https://link.aps.org/doi/10.1103/PhysRevC.90.035202 (visited on 09/17/2023).

[28] Navjot Hothi. “A brief overview of exotic hadron states”. en. In: *Materials Today: Proceedings* 64 (2022), pp. 1202–1205. ISSN: 22147853. DOI: 10.1016/j.matpr.2022.03.584. URL: https://linkinghub.elsevier.com/retrieve/pii/S2214785322019332 (visited on 11/26/2023).

[29] R. H. Dalitz and S. F. Tuan. “Possible Resonant State in Pion-Hyperon Scattering”. en. In: *Physical Review Letters* 2.10 (May 1959), pp. 425–428. ISSN: 0031-9007. DOI: 10.1103/PhysRevLett.2.425. URL: https://link.aps.org/doi/10.1103/PhysRevLett.2.425 (visited on 11/28/2023).

[30] Margaret H. Alston et al. “Study of Resonances of the System”. en. In: *Physical Review Letters* 6.12 (June 1961), pp. 698–702. ISSN: 0031-9007. DOI: 10.1103/PhysRevLett.6.698. URL: https://link.aps.org/doi/10.1103/PhysRevLett.6.698 (visited on 11/28/2023).

[31] A. Zhang et al. *$J^P={1/2}^-$ Pentaquarks in Jaffe and Wilczek’s Diquark Model*. arXiv:hep-ph/0403210. Mar. 2004. URL: http://arxiv.org/abs/hep-ph/0403210 (visited on 11/28/2023).

[32] R. J. Jaffe. “Multiquark hadrons. I. Phenomenology of Q 2 Q ¯ 2 mesons”. en. In: *Physical Review D* 15.1 (Jan. 1977), pp. 267–280. ISSN: 0556-2821. DOI: 10.1103/PhysRevD.15.267. URL: https://link.aps.org/doi/10.1103/PhysRevD.15.267 (visited on 11/28/2023).

[33] R. L. Jaffe. “Multiquark hadrons. II. Methods”. en. In: *Physical Review D* 15.1 (Jan. 1977), pp. 281–289. ISSN: 0556-2821. DOI: 10.1103/PhysRevD.15.281. URL: https://link.aps.org/doi/10.1103/PhysRevD.15.281 (visited on 11/28/2023).

[34] C. Gignoux, B. Silvestre-Brac, and J.M. Richard. “Possibility of stable multiquark baryons”. en. In: *Physics Letters B* 193.2-3 (July 1987), pp. 323–326. ISSN: 03702693. DOI: 10.1016/0370-2693(87)91244-5. URL: https://linkinghub.elsevier.com/retrieve/pii/0370269387912445 (visited on 11/28/2023).

[35] Harry J. Lipkin. "New possibilities for exotic hadrons — anticharmed strange baryons". en. In: *Physics Letters B* 195.3 (Sept. 1987), pp. 484–488. ISSN: 03702693. DOI: 10.1016/0370-2693(87)90055-4. URL: https://linkinghub.elsevier.com/retrieve/pii/0370269387900554 (visited on 11/28/2023).

[36] Stephen Lars Olsen. "A new hadron spectroscopy". en. In: *Frontiers of Physics* 10.2 (Apr. 2015), pp. 121–154. ISSN: 2095-0462, 2095-0470. DOI: 10.1007/s11467-014-0449-6. URL: http://link.springer.com/10.1007/s11467-014-0449-6 (visited on 11/28/2023).

[37] T. Nakano et al. "Evidence for a Narrow S = + 1 Baryon Resonance in Photoproduction from the Neutron". en. In: *Physical Review Letters* 91.1 (July 2003), p. 012002. ISSN: 0031-9007, 1079-7114. DOI: 10.1103/PhysRevLett.91.012002. URL: https://link.aps.org/doi/10.1103/PhysRevLett.91.012002 (visited on 12/12/2023).

[38] Reinhard A. Schumacher. "The Rise and Fall of Pentaquarks in Experiments". In: *AIP Conference Proceedings*. Vol. 842. ISSN: 0094243X arXiv:nucl-ex/0512042. 2006, pp. 409–417. DOI: 10.1063/1.2220285. URL: http://arxiv.org/abs/nucl-ex/0512042 (visited on 12/12/2023).

[39] R. Aaij et al. "Determination of the X (3872) Meson Quantum Numbers". en. In: *Physical Review Letters* 110.22 (May 2013), p. 222001. ISSN: 0031-9007, 1079-7114. DOI: 10.1103/PhysRevLett.110.222001. URL: https://link.aps.org/doi/10.1103/PhysRevLett.110.222001 (visited on 12/14/2023).

[40] Harold C. Urey, F. G. Brickwedde, and G. M. Murphy. "A Hydrogen Isotope of Mass 2". en. In: *Physical Review* 39.1 (Jan. 1932), pp. 164–165. ISSN: 0031-899X. DOI: 10.1103/PhysRev.39.164. URL: https://link.aps.org/doi/10.1103/PhysRev.39.164 (visited on 09/05/2023).

[41] H. Clement. "On the History of Dibaryons and their Final Observation". en. In: *Progress in Particle and Nuclear Physics* 93 (Mar. 2017). arXiv: 1610.05591, pp. 195–242. ISSN: 01466410. DOI: 10.1016/j.ppnp.2016.12.004. URL: http://arxiv.org/abs/1610.05591 (visited on 06/15/2021).

[42] P. Adlarson et al. "Abashian-Booth-Crowe Effect in Basic Double-Pionic Fusion: A New Resonance?" en. In: *Physical Review Letters* 106.24 (June 2011), p. 242302. ISSN: 0031-9007, 1079-7114. DOI: 10.1103/PhysRevLett.106.242302. URL: https://link.aps.org/doi/10.1103/PhysRevLett.106.242302 (visited on 08/23/2023).

[43] P. Adlarson et al. “Isospin decomposition of the basic double-pionic fusion in the region of the ABC effect”. en. In: *Physics Letters B* 721.4-5 (Apr. 2013), pp. 229–236. ISSN: 03702693. DOI: 10.1016/j.physletb.2013.03.019. URL: https://linkinghub.elsevier.com/retrieve/pii/S0370269313002311 (visited on 08/23/2023).

[44] P. Adlarson et al. “Measurement of the p n → p p 0 reaction in search for the recently observed resonance structure in d 0 0 and d + systems”. en. In: *Physical Review C* 88.5 (Nov. 2013), p. 055208. ISSN: 0556-2813, 1089-490X. DOI: 10.1103/PhysRevC.88.055208. URL: https://link.aps.org/doi/10.1103/PhysRevC.88.055208 (visited on 08/23/2023).

[45] P. Adlarson et al. “Neutron-proton scattering in the context of the d * (2380) resonance”. en. In: *Physical Review C* 90.3 (Sept. 2014), p. 035204. ISSN: 0556-2813, 1089-490X. DOI: 10.1103/PhysRevC.90.035204. URL: https://link.aps.org/doi/10.1103/PhysRevC.90.035204 (visited on 08/23/2023).

[46] WASA-at-COSY Collaboration et al. “Measurement of the $\overrightarrow{n} p\rightarrow d\pi^{0}\pi^{0}$ reaction with polarized beam in the region of the d*(2380) resonance”. en. In: *The European Physical Journal A* 52.5 (May 2016), p. 147. ISSN: 1434-6001, 1434-601X. DOI: 10.1140/epja/i2016-16147-5. URL: http://link.springer.com/10.1140/epja/i2016-16147-5 (visited on 08/23/2023).

[47] M. Bashkanov, H. Clement, and T. Skorodko. “Branching ratios for the decay of d*(2380)”. en. In: *The European Physical Journal A* 51.7 (July 2015), p. 87. ISSN: 1434-6001, 1434-601X. DOI: 10.1140/epja/i2015-15087-x. URL: http://link.springer.com/10.1140/epja/i2015-15087-x (visited on 08/23/2023).

[48] M. Bashkanov et al. “Deuteron photodisintegration by polarized photons in the region of the d∗(2380)”. en. In: *Physics Letters B* 789 (Feb. 2019), pp. 7–12. ISSN: 03702693. DOI: 10.1016/j.physletb.2018.12.026. URL: https://linkinghub.elsevier.com/retrieve/pii/S0370269318309535 (visited on 09/21/2023).

[49] M. Bashkanov et al. “Signatures of the d * (2380) Hexaquark in d (, p n →)”. en. In: *Physical Review Letters* 124.13 (Mar. 2020), p. 132001. ISSN: 0031-9007, 1079-7114. DOI: 10.1103/PhysRevLett.124.132001. URL: https://link.aps.org/doi/10.1103/PhysRevLett.124.132001 (visited on 09/22/2023).

[50] M. Bashkanov et al. "First measurement of polarisation transfer C x n in deuteron photodisintegration". en. In: *Physics Letters B* 844 (Sept. 2023), p. 138080. ISSN: 03702693. DOI: 10.1016/j.physletb.2023.138080. URL: https://linkinghub.elsevier.com/retrieve/pii/S0370269323004148 (visited on 09/22/2023).

[51] P. Adlarson et al. "Evidence for a New Resonance from Polarized Neutron-Proton Scattering". en. In: *Physical Review Letters* 112.20 (May 2014), p. 202301. ISSN: 0031-9007, 1079-7114. DOI: 10.1103/PhysRevLett.112.202301. URL: https://link.aps.org/doi/10.1103/PhysRevLett.112.202301 (visited on 08/20/2023).

[52] Fan Wang, Jialun Ping, and Hongxia Huang. *Remarks on the hidden color components in multi-quark study*. arXiv:1711.01445 [hep-ph, physics:nucl-th]. Nov. 2017. URL: http://arxiv.org/abs/1711.01445 (visited on 09/29/2023).

[53] V.D. Burkert et al. "The CLAS12 Spectrometer at Jefferson Laboratory". en. In: *Nuclear Instruments and Methods in Physics Research Section A: Accelerators, Spectrometers, Detectors and Associated Equipment* 959 (Apr. 2020), p. 163419. ISSN: 01689002. DOI: 10.1016/j.nima.2020.163419. URL: https://linkinghub.elsevier.com/retrieve/pii/S0168900220300243 (visited on 06/15/2020).

[54] Christoph W. Leemann, David R. Douglas, and Geoffrey A. Krafft. "THE CONTINUOUS ELECTRON BEAM ACCELERATOR FACILITY: CEBAF at the Jefferson Laboratory". In: *Annual Review of Nuclear and Particle Science* 51.1 (2001). _eprint: https://doi.org/10.1146/annurev.nucl.51.10170 pp. 413–450. DOI: 10.1146/annurev.nucl.51.101701.132327. URL: https://doi.org/10.1146/annurev.nucl.51.101701.132327 (visited on 05/18/2023).

[55] A. Acker et al. "The CLAS12 Forward Tagger". en. In: *Nuclear Instruments and Methods in Physics Research Section A: Accelerators, Spectrometers, Detectors and Associated Equipment* 959 (Apr. 2020), p. 163475. ISSN: 01689002. DOI: 10.1016/j.nima.2020.163475. URL: https://linkinghub.elsevier.com/retrieve/pii/S0168900220300838 (visited on 08/28/2023).

[56] A. Acker et al. "The CLAS12 Forward Tagger". en. In: *Nuclear Instruments and Methods in Physics Research Section A: Accelerators, Spectrometers, Detectors and Associated Equipment* 959 (Apr. 2020), p. 163475. ISSN: 01689002. DOI: 10.1016/j.nima.2020.163475. URL: https://linkinghub.elsevier.com/retrieve/pii/S0168900220300838 (visited on 06/16/2021).

[57] Ernest M. Henley, Alejandro García, and Hans Frauenfelder. *Subatomic physics*. en. 3rd ed. Hackensack, N.J: World Scientific, 2007. ISBN: 978-981-270-056-8 978-981-270-057-5.

[58] M.D. Mestayer et al. "The CLAS12 drift chamber system". en. In: *Nuclear Instruments and Methods in Physics Research Section A: Accelerators, Spectrometers, Detectors and Associated Equipment* 959 (Apr. 2020), p. 163518. ISSN: 01689002. DOI: 10.1016/j.nima.2020.163518. URL: https://linkinghub.elsevier.com/retrieve/pii/S016890022030111X (visited on 06/15/2020).

[59] D.S. Carman et al. "The CLAS12 Forward Time-of-Flight system". en. In: *Nuclear Instruments and Methods in Physics Research Section A: Accelerators, Spectrometers, Detectors and Associated Equipment* 960 (Apr. 2020), p. 163629. ISSN: 01689002. DOI: 10.1016/j.nima.2020.163629. URL: https://linkinghub.elsevier.com/retrieve/pii/S0168900220302102 (visited on 09/20/2023).

[60] Y.G. Sharabian et al. "The CLAS12 high threshold Cherenkov counter". en. In: *Nuclear Instruments and Methods in Physics Research Section A: Accelerators, Spectrometers, Detectors and Associated Equipment* 968 (July 2020), p. 163824. ISSN: 01689002. DOI: 10.1016/j.nima.2020.163824. URL: https://linkinghub.elsevier.com/retrieve/pii/S0168900220303466 (visited on 06/15/2023).

[61] M. Ungaro et al. "The CLAS12 Geant4 simulation". en. In: *Nuclear Instruments and Methods in Physics Research Section A: Accelerators, Spectrometers, Detectors and Associated Equipment* 959 (Apr. 2020), p. 163422. ISSN: 01689002. DOI: 10.1016/j.nima.2020.163422. URL: https://linkinghub.elsevier.com/retrieve/pii/S0168900220300279 (visited on 01/08/2024).

[62] M. Contalbrigo et al. "The CLAS12 Ring Imaging Cherenkov detector". In: *Nuclear Instruments and Methods in Physics Research, Section A: Accelerators, Spectrometers, Detectors and Associated Equipment* 964.March (2020). Publisher: Elsevier Ltd, pp. 163791–163791. DOI: 10.1016/j.nima.2020.163791. URL: https://doi.org/10.1016/j.nima.2020.163791.

[63] M.A. Antonioli et al. "The CLAS12 Silicon Vertex Tracker". en. In: *Nuclear Instruments and Methods in Physics Research Section A: Accelerators, Spectrometers, Detectors and Associated Equipment* 962 (May 2020), p. 163701. ISSN: 01689002. DOI: 10.1016/j.nima.2020.163701. URL: https://linkinghub.elsevier.com/retrieve/pii/S0168900220302588 (visited on 09/20/2023).

[64] P. Chatagnon et al. "The CLAS12 Central Neutron Detector". In: *Nuclear Instruments and Methods in Physics Research, Section A: Accelerators, Spectrometers, Detectors and Associated*

Equipment 959.January (2020). Publisher: Elsevier Ltd, pp. 163441–163441. DOI: 10.1016/j.nima.2020.163441. URL: https://doi.org/10.1016/j.nima.2020.163441.

[65] R. Fair et al. "The CLAS12 superconducting magnets". en. In: *Nuclear Instruments and Methods in Physics Research Section A: Accelerators, Spectrometers, Detectors and Associated Equipment* 962 (May 2020), p. 163578. ISSN: 01689002. DOI: 10.1016/j.nima.2020.163578. URL: https://linkinghub.elsevier.com/retrieve/pii/S0168900220301522 (visited on 07/27/2023).

[66] B. Raydo et al. "The CLAS12 Trigger System". en. In: *Nuclear Instruments and Methods in Physics Research Section A: Accelerators, Spectrometers, Detectors and Associated Equipment* 960 (Apr. 2020), p. 163529. ISSN: 01689002. DOI: 10.1016/j.nima.2020.163529. URL: https://linkinghub.elsevier.com/retrieve/pii/S0168900220301182 (visited on 11/30/2023).

[67] M. Bashkanov et al. *Dibaryons and where to find them*. arXiv:2308.07066 [hep-ph, physics:nucl-th] version: 1. Aug. 2023. URL: http://arxiv.org/abs/2308.07066 (visited on 01/09/2024).

[68] A. Gal. "The d $*$ (2380) dibaryon resonance width and decay branching ratios". en. In: *Physics Letters B* 769 (June 2017), pp. 436–440. ISSN: 03702693. DOI: 10.1016/j.physletb.2017.03.040. URL: https://linkinghub.elsevier.com/retrieve/pii/S0370269317302289 (visited on 08/29/2023).

[69] M Bashkanov and H Clement. "Phenomenological Description of the pn $\rightarrow$ R $\rightarrow$ $\rightarrow$ d00 Reaction and its Confrontation with WASA-at-COSY Data". en. In: ().

[70] P Adlarson et al. "Measurement of the np$\rightarrow$np00 reaction in search for the recently observed d*(2380) resonance". en. In: *Physics Letters B* (2015).

[71] G. Agakishiev et al. "Study of the quasi-free np $\rightarrow$ np $+$ reaction with a deuterium beam at 1.25 GeV/nucleon". en. In: *Physics Letters B* 750 (Nov. 2015), pp. 184–193. ISSN: 03702693. DOI: 10.1016/j.physletb.2015.09.016. URL: https://linkinghub.elsevier.com/retrieve/pii/S0370269315006917 (visited on 12/06/2023).

[72] *s018.dvi - rpp2023-list-lambda.pdf*. URL: https://pdg.lbl.gov/2023/web/viewer.html?file=../listings/rpp2023-list-lambda.pdf (visited on 08/26/2023).

[73] *GEant4 Monte-Carlo — GEMC*. URL: https://gemc.jlab.org/gemc/html/index.html (visited on 08/17/2023).

[74] Annette Pricking, M. Bashkanov, and H. Clement. *Implications of the ABC Resonance Structure on Elastic Neutron-Proton Scattering*. arXiv:1310.5532 [nucl-ex, physics:nucl-th]. Oct. 2013. URL: http://arxiv.org/abs/1310.5532 (visited on 08/16/2023).

[75] *Home - RCDB*. URL: https://clasweb.jlab.org/rcdb (visited on 08/22/2023).

[76] V. Ziegler et al. "The CLAS12 software framework and event reconstruction". en. In: *Nuclear Instruments and Methods in Physics Research Section A: Accelerators, Spectrometers, Detectors and Associated Equipment* 959 (Apr. 2020), p. 163472. ISSN: 01689002. DOI: 10.1016/j.nima.2020.163472. URL: https://linkinghub.elsevier.com/retrieve/pii/S0168900220300784 (visited on 09/27/2023).

[77] *Event IO (evio) | Data Acquisition Support*. URL: https://coda.jlab.org/drupal/content/event-io-evio (visited on 09/27/2023).

[78] *HIPO File Format — HIPO 1.0 documentation*. URL: https://userweb.jlab.org/~gavalian/docs/sphinx/hipo/html/chapters/hipo_introduction.html (visited on 08/18/2023).

[79] ROOT team. *ROOT: analyzing petabytes of data, scientifically.* en. URL: https://root.cern/ (visited on 08/18/2023).

[80] *Clas12Root*. original-date: 2019-08-20T22:44:05Z. June 2022. URL: https://github.com/JeffersonLab/clas12root (visited on 09/28/2023).

[81] *s017.dvi - rpp2023-list-n.pdf*. URL: https://pdg.lbl.gov/2023/web/viewer.html?file=../listings/rpp2023-list-n.pdf (visited on 08/26/2023).

[82] KLF Collaboration et al. *Strange Hadron Spectroscopy with Secondary KL Beam in Hall D*. arXiv:2008.08215 [hep-ex, physics:hep-ph, physics:nucl-ex, physics:nucl-th]. Mar. 2021. URL: http://arxiv.org/abs/2008.08215 (visited on 08/17/2023).

[83] R. Abdul Khalek et al. "Science Requirements and Detector Concepts for the Electron-Ion Collider". en. In: *Nuclear Physics A* 1026 (Oct. 2022), p. 122447. ISSN: 03759474. DOI: 10.1016/j.nuclphysa.2022.122447. URL: https://linkinghub.elsevier.com/retrieve/pii/S0375947422000677 (visited on 09/07/2023).